SANDIA REPORT
SAND2021-7427
Unclassified Unlimited Release
Printed June 22, 2021

Sandia National Laboratories

Development, Implementation, and Verification of Partially-Ionized Collisional Multifluid Plasma Models in Drekar

Michael M. Crockatt (mmcrock@sandia.gov) — *Computational Multiphysics, Center for Computing Research*

John N. Shadid (jnshadi@sandia.gov) — *Computational Mathematics, Center for Computing Research*

Prepared by
Sandia National Laboratories
Albuquerque, New Mexico 87185
Livermore, California 94550

Issued by Sandia National Laboratories, operated for the United States Department of Energy by National Technology & Engineering Solutions of Sandia, LLC.

Printed in the United States of America. This report has been reproduced directly from the best available copy.

Available to DOE and DOE contractors from

U.S. Department of Energy
Office of Scientific and Technical Information
P.O. Box 62
Oak Ridge, TN 37831

Telephone: (865) 576-8401
Facsimile: (865) 576-5728
E-Mail: reports@osti.gov
Online ordering: http://www.osti.gov/scitech

Available to the public from

U.S. Department of Commerce
National Technical Information Service
5301 Shawnee Road
Alexandria, VA 22312

Telephone: (800) 553-6847
Facsimile: (703) 605-6900
E-Mail: orders@ntis.gov
Online order: https://classic.ntis.gov/help/order-methods

ABSTRACT

We consider the development of multifluid models for partially ionized multispecies plasmas. The models are composed of a standard set of five-moment fluid equations for each species plus a description of electromagnetics. The most general model considered utilizes a full set of fluid equations for each charge state of each atomic species, plus a set of fluid equations for electrons. The fluid equations are coupled through source terms describing electromagnetic coupling, ionization, recombination, charge exchange, and elastic scattering collisions in the low-density coronal limit. The form of each of these source terms is described in detail, and references for required rate coefficients are identified for a diverse range of atomic species. Initial efforts have been made to extend these models to incorporate some higher-density collisional effects, including ionization potential depression and three-body recombination.

Some reductions of the general multifluid model are considered. First, a reduced multifluid model is derived which averages over all of the charge states (including neutrals) of each atomic species in the general multifluid model. The resulting model maintains full consistency with the general multifluid model from which it is derived by leveraging a quasi-steady-state collisional ionization equilibrium assumption to recover the ionization fractions required to make use of the general collision models. Further reductions are briefly considered to derive certain components of a single-fluid magnetohydrodynamics (MHD) model. In this case, a generalized Ohm's law is obtained, and the standard MHD resistivity is expressed in terms of the collisional models used in the general multifluid model.

A number of numerical considerations required to obtain robust implementations of these multifluid models are discussed. First, an algebraic flux correction (AFC) stabilization approach for a continuous Galerkin finite element discretization of the multifluid system is described in which the characteristic speeds used in the stabilization of the fluid systems are synchronized across all species in the model. It is demonstrated that this synchronization is crucial in order to obtain a robust discretization of the multifluid system. Additionally, several different formulations are considered for describing the electromagnetics portion of the multifluid system using nodal continuous Galerkin finite element discretizations. The formulations considered include a parabolic divergence cleaning method and an implicit projection method for the traditional curl formulation of Maxwell's equations, a purely-hyperbolic potential-based formulation of Maxwell's equations, and a mixed hyperbolic-elliptic potential-based formulation of Maxwell's equations. Some advantages and disadvantages of each formulation are explored to compare solution robustness and the ease of use of each formulation.

Numerical results are presented to demonstrate the accuracy and robustness of various components of our implementation. Analytic solutions for a spatially homogeneous damped plasma oscillation are derived in order to verify the implementation of the source terms for electromagnetic coupling and elastic collisions between fluid species. Ionization balance as a function of electron temperature is evaluated for several atomic species of interest by comparing to steady-state calculations using various sets of ionization and recombination rate coefficients. Several test problems in one and two spatial dimensions are used to demonstrate the accuracy and robustness of the discretization and stabilization approach for the fluid components of the multifluid system. This includes standard test problems for electrostatic and electromagnetic shock tubes in the two-fluid and ideal shock-MHD limits, a cylindrical diocotron instability, and the GEM challenge magnetic reconnection problem. A one-dimensional simplified prototype of an argon gas puff configuration as deployed on Sandia's Z-machine is used as a demonstration to exercise the full range of capabilities associated with the general multifluid model.

ACKNOWLEDGEMENT

The authors would like to thank Roger Pawlowski, Sidafa Conde, Sibusiso Mabuza, Tom Smith, Ari Rappaport, and Ignacio Tomas, for collaborative contributions to the development of the multifluid plasma capabilities, stabilization, and implicit solution algorithms in Drekar. We would also like to thank Allen Robinson for reviewing this manuscript, providing feedback to assist in removing typos and improving clarity, and for pointing out that the numerical issues that have been encountered when using the implicit projection scheme for Maxwell's equations may be due to the fact that a periodic potential cannot represent a field with non-zero mean.

This work was partially supported by the U.S. Department of Energy, Office of Science, Office of Advanced Scientific Computing Research, Applied Mathematics Program, and by the U.S. Department of Energy, Office of Science, Office of Advanced Scientific Computing Research and Office of Fusion Energy Sciences, Scientific Discovery through the Advanced Computing (SciDAC) program.

CONTENTS

LIST OF FIGURES

LIST OF TABLES

1. INTRODUCTION

1.1. Notation

The following notation is assumed throughout:

(i) When used as a subscript, the symbol e will be used to denote quantities associated with the electron species.

(ii) N_A denotes the number of atomic species, which are indexed by $\alpha, \beta \in \{1, \ldots, N_A\}$.

(iii) z_α denotes the maximum tracked charge state of atomic species α. We note that this value may be different than the maximum charge state $z_\alpha^{\max}$ for the species; ie., $0 < z_\alpha \leq z_\alpha^{\max}$.

(iv) An ordered pair (α, k) will be used to denote associations with neutrals ($k = 0$) or ions ($k > 0$) of atomic species α with charge state k. We assume always that $k \geq 0$.

(v) Standard non-bold fonts will be used for scalar quantities in $\mathbb{R}$.

(vi) Bold fonts will be used for vector quantities in $\mathbb{R}^3$ (eg., $\mathbf{u}$ for velocity).

(vii) Bold fonts with a single underline will be used for second-order tensors in $\mathbb{R}^3 \otimes \mathbb{R}^3$ (eg., $\underline{\mathbf{P}}$ for the pressure tensor).

(viii) An exponent applied to a vector quantity will be used to denote the dot product of that quantity with itself; ie., $\mathbf{u}^2 = \mathbf{u} \cdot \mathbf{u}$.

(ix) Quantities associated with a particle species s will be denoted as follows:

m_s	particle mass	$\underline{\mathbf{P}}_s$	pressure tensor
n_s	number density	p_s	scalar pressure
ρ_s	mass density	$\underline{\mathbf{\Pi}}_s$	deviatoric stress tensor
q_s	electric charge	e_s	specific internal energy
Z_s	signed charge number	T_s	temperature
$\mathcal{E}_s$	total energy	$\mathbf{h}_s$	heat flux
$\mathbf{u}_s$	average fluid velocity		

These quantities satisfy the following relations:

$$\rho_s = m_s n_s, \qquad \mathcal{E}_s = \frac{1}{2}\rho_s \mathbf{u}_s^2 + \rho_s e_s,$$
$$q_s = -Z_s q_e, \qquad \underline{\mathbf{P}}_s = p_s \underline{\mathbf{I}} + \underline{\mathbf{\Pi}}_s.$$

(x) Products of quantities for the same species may be grouped via parentheses to share one species subscript; eg., for momentum $\rho_s \mathbf{u}_s = (\rho \mathbf{u})_s$.

(xi) The following constants are used:

(a) k_B is the Boltzmann constant.

(b) ϵ_0 is the vacuum electrical permittivity.

(c) μ_0 is the vacuum magnetic permeability.

(d) $c = (\varepsilon_0 \mu_0)^{-1/2}$ is the speed of light in vacuum.

(e) q_e is the (negative) elementary electric charge.

(f) e (in an upright typeface) may occasionally be used to denote the positive elementary electric charge $|q_e|$. The use of this notation will generally be limited to cases in which the use of the signed charge q_e is particularly cumbersome.

Implementation. Comments related to the implementation of the multifluid models described herein in the Drekar code are given in a box of this format. These comments are intended to aid in the implementation of these models, or describe specific implementation details motivated by purely numerical considerations.

1.2. Kinetic model

We consider models for a partially-ionized plasma composed of multiple atomic species indexed by $\alpha \in \{1,\dots,N_A\}$, each of which may be present in one of several charge states $k \in \{0,1,\dots,z_\alpha\}$. The fluid descriptions that are the focus of this document can be derived by taking various moments (with respect to the velocity variables) of a coupled set of kinetic equations. Each such kinetic equation takes a form typical for charged particle motion:

$$\partial_t f_s + \mathbf{v}\cdot\nabla_{\mathbf{x}} f_s + \frac{q_s}{m_s}\left(\mathbf{E}+\mathbf{v}\times\mathbf{B}\right)\cdot\nabla_{\mathbf{v}} f_s = \mathcal{C}_s\left[f_s\right] + \mathcal{S}_s, \tag{1}$$

where $f_s = f_s(\mathbf{x},\mathbf{v},t)$ is the one-particle distribution function for species s, $\mathcal{S}_s$ is a source of particles of type s, and s represents one of:

(i) e (for the electron species),

(ii) $(\alpha,0)$ with $\alpha \in \{1,\dots,N_A\}$ (for neutral species), or

(iii) (α,k) with $\alpha \in \{1,\dots,N_A\}$ and $k \in \{1,\dots,z_\alpha\}$ (for ion species with charge k);

or more simply $s \in \Lambda_{\mathrm{G}}$, where the index set Λ_{G} is defined by

$$\Lambda_{\mathrm{G}} = \left\{(\alpha,k) : \alpha = 1,\dots,N_A; k = 0,\dots,z_\alpha\right\} \cup \{e\}. \tag{2}$$

The kinetic equations (1) are coupled through the collision operators $\mathcal{C}_s$, which describe interactions between particles. These interactions may occur between species of the same type or between species of different types. Collisions of both scattering and reacting types are considered, with reacting interactions covering electron-collision ionization, radiative and dielectronic recombination, three-body recombination, and resonant charge exchange events. The following general assumptions are made:

(i) It is assumed that resonant charge-exchange interactions occur only between ion and neutral species of the same type; that is, we neglect effects due to charge exchange between two ions and charge exchange between different atomic species.

(ii) The plasma is assumed to be optically thin, so that modeling the dynamics of the radiation field and and its effects on the plasma (eg., photoionization) may be neglected.

(iii) We assume that atoms of different species $\alpha \neq \beta$ engage in only scattering interactions; that is, reacting interactions are restricted to particles of the same atomic species.

For purposes of notation, the collision operators $\mathcal{C}_s$ may be decomposed into a sum of contributions from various interaction types:

$$\mathcal{C}_s = \mathcal{C}_s^{\mathrm{sc}} + \mathcal{C}_s^{\mathrm{ion}} + \mathcal{C}_s^{\mathrm{rec}} + \mathcal{C}_s^{\mathrm{tbr}} + \mathcal{C}_s^{\mathrm{cx}} + \mathcal{C}_s^{\mathrm{rad}}, \tag{3}$$

where each term denotes interactions as follows:

$$\mathcal{C}_s^{\mathrm{sc}} : \text{Scattering interactions,} \tag{4a}$$
$$\mathcal{C}_s^{\mathrm{ion}} : \text{Ionization reactions,} \tag{4b}$$
$$\mathcal{C}_s^{\mathrm{rec}} : \text{Recombination reactions,} \tag{4c}$$
$$\mathcal{C}_s^{\mathrm{tbr}} : \text{Three-body recombination reactions,} \tag{4d}$$
$$\mathcal{C}_s^{\mathrm{cx}} : \text{Charge-exchange reactions,} \tag{4e}$$
$$\mathcal{C}_s^{\mathrm{rad}} : \text{Radiative emission.} \tag{4f}$$

For more thorough discussions concerning the form of the collision operators $\mathcal{C}_s$ see, for example, [64, 65].

1.3. Summary of fluid models

Each multifluid model is based on a standard set of five-moment fluid equations, which can be derived by taking various velocity moments of a set of kinetic equations of the form (1). The resulting fluid equations can be written as

$$\partial_t \rho_s + \nabla \cdot \left(\rho_s \mathbf{u}_s\right) = \mathcal{C}_s^{[0]} + \mathcal{S}_s^{[0]}, \tag{5a}$$

$$\partial_t \left(\rho_s \mathbf{u}_s\right) + \nabla \cdot \left(\rho_s \mathbf{u}_s \otimes \mathbf{u}_s + p_s \underline{\mathbf{I}} + \underline{\boldsymbol{\Pi}}_s\right) = q_s n_s \left(\mathbf{E} + \mathbf{u}_s \times \mathbf{B}\right) + \boldsymbol{\mathcal{C}}_s^{[1]} + \boldsymbol{\mathcal{S}}_s^{[1]}, \tag{5b}$$

$$\partial_t \mathcal{E}_s + \nabla \cdot \left[\left(\mathcal{E}_s + p_s\right)\mathbf{u}_s + \mathbf{u}_s \cdot \underline{\boldsymbol{\Pi}}_s + \mathbf{h}_s\right] = q_s n_s \mathbf{u}_s \cdot \mathbf{E} + \mathcal{C}_s^{[2]} + \mathcal{S}_s^{[2]}, \tag{5c}$$

where the notation used here largely follows that of [46]. While the derivation of these fluid equations proceeds under the assumption of an ideal gas for each fluid, they have been written in a general form to permit non-ideal closures and equations of state to be used if desired. The form of these fluid equations is provided here for reference: detailed derivations of these fluid equations can be found in, eg., [19, 46]. The remainder of this document focuses primarily on the structure of the interaction terms $\mathcal{C}_s^{[0]}$, $\boldsymbol{\mathcal{C}}_s^{[1]}$, and $\mathcal{C}_s^{[2]}$, and on certain numerical considerations related to the robust implementation of multifluid models in the Drekar code.

2. GENERAL MULTIFLUID MODEL

2.1. Model description

We now consider a general multifluid model based on taking various velocity moments the kinetic equations (1) for each species. This yields a set of standard five-moment fluid equations (continuity, momentum, and total energy) for each species. The source terms for each equation are written in a general form for either an electron species or an arbitrary atomic species. In order to avoid repetition, only the most general form of each source term is provided for the atomic species: This is done with the understanding that not all ionization and recombination terms will be present for each species; ie., neutral atoms do not recombine and ions of the maximum charge state for a species do not further ionize. Even though the corresponding source terms are included in the description of the general source terms, these terms are effectively zero.

The continuity, momentum, and total energy equations for each species are given by (5), where

$$\mathcal{C}_s^{[0]} \approx m_s \int \mathcal{C}_s\left[f_s\right] d\mathbf{v}, \qquad \boldsymbol{\mathcal{C}}_s^{[1]} \approx m_s \int \mathbf{v} \mathcal{C}_s\left[f_s\right] d\mathbf{v}, \qquad \text{and} \qquad \mathcal{C}_s^{[2]} \approx m_s \int \mathbf{v}^2 \mathcal{C}_s\left[f_s\right] d\mathbf{v} \tag{6a}$$

describe exchange of mass, momentum, and energy due to collisional interactions between species, and

$$\mathcal{S}_s^{[0]} \approx m_s \int \mathcal{S}_s \, d\mathbf{v}, \qquad \boldsymbol{\mathcal{S}}_s^{[1]} \approx m_s \int \mathbf{v} \mathcal{S}_s \, d\mathbf{v}, \qquad \text{and} \qquad \mathcal{S}_s^{[2]} \approx m_s \int \mathbf{v}^2 \mathcal{S}_s \, d\mathbf{v}, \tag{6b}$$

represent external sources. We do not derive the expressions for the fluid source terms here: the interested reader is referred to the derivations in [64, 65] on which this work is based. The purpose of the model development here is to extend the work of [64, 65] (largely through modifications of notation) from the case of a three-species plasma (neutral, ion, electron) to a more general context for plasmas containing arbitrarily many atomic species and charge states. Additionally, the fluid energy equations are written directly in terms of internal and kinetic energy densities to remove the assumption of an ideal gas equation of state and allow for an arbitrary equation of state to be used for each fluid species.

Expressions are provided for the collision terms in two forms. In section 2.1.1, the source terms are written using notation that is a direct extension of that of [64, 65]. In section 2.1.2, the source terms are re-written strictly in terms of the conserved fluid quantities.

2.1.1. Meier notation

Mass exchange. The collision sources $\mathcal{C}_s^{[0]}$ have the form

$$\mathcal{C}_e^{[0]} = m_e \sum_{\substack{(\alpha,k)\in\mathcal{N}_S \\ k\neq z_\alpha}} \Gamma^{\text{ion}}_{(\alpha,k)} - m_e \sum_{\substack{(\alpha,k)\in\mathcal{N}_S \\ k\neq 0}} \left(\Gamma^{\text{rec}}_{(\alpha,k)} + \Gamma^{\text{tbr}}_{(\alpha,k)}\right), \tag{7a}$$

$$\mathcal{C}^{[0]}_{(\alpha,k)} = m_{(\alpha,k)}\left(\Gamma^{\text{ion}}_{(\alpha,k-1)} - \Gamma^{\text{ion}}_{(\alpha,k)} - \Gamma^{\text{rec}}_{(\alpha,k)} + \Gamma^{\text{rec}}_{(\alpha,k+1)} - \Gamma^{\text{tbr}}_{(\alpha,k)} + \Gamma^{\text{tbr}}_{(\alpha,k+1)}\right), \qquad (\alpha,k)\in\Lambda_{\text{G}}, \tag{7b}$$

where

$$\Gamma^{\text{ion}}_s = n_e n_s I_s, \qquad \Gamma^{\text{rec}}_s = n_e n_s R_s, \qquad \Gamma^{\text{tbr}}_s = n_e^2 n_s R^{\text{tbr}}_s, \tag{8a}$$

and

$$I_s = \langle \sigma^{\text{ion}}_s \mathbf{v}_e \rangle, \qquad R_s = \langle \sigma^{\text{rec}}_s \mathbf{v}_e \rangle, \qquad R^{\text{tbr}}_s = \langle \sigma^{\text{tbr}}_s \mathbf{v}_e \rangle \tag{8b}$$

are the ionization, radiative-plus-dielectronic recombination, and three-body recombination rate parameters, respectively.

Exchange of momentum. The collision sources $\boldsymbol{\mathcal{C}}_s^{[1]}$ have the form

$$\boldsymbol{\mathcal{C}}_e^{[1]} = m_e \sum_{\substack{(\alpha,k)\in\mathcal{N}_S \\ k\neq z_\alpha}} \mathbf{u}_{(\alpha,k)}\Gamma^{\text{ion}}_{(\alpha,k)} - m_e\mathbf{u}_e \sum_{\substack{(\alpha,k)\in\mathcal{N}_S \\ k\neq 0}} \left(\Gamma^{\text{rec}}_{(\alpha,k)} + \Gamma^{\text{tbr}}_{(\alpha,k)}\right) + \sum_{(\alpha,k)\in\mathcal{N}_S} \mathbf{R}_{e;(\alpha,k)} \tag{9a}$$

for the electron species, and

$$\begin{aligned}\boldsymbol{\mathcal{C}}^{[1]}_{(\alpha,k)} = {} & m_{(\alpha,k)}\mathbf{u}_{(\alpha,k-1)}\Gamma^{\text{ion}}_{(\alpha,k-1)} - m_{(\alpha,k)}\mathbf{u}_{(\alpha,k)}\left(\Gamma^{\text{ion}}_{(\alpha,k)} + \Gamma^{\text{rec}}_{(\alpha,k)} + \Gamma^{\text{tbr}}_{(\alpha,k)}\right) \\ & + \left(m_{(\alpha,k+1)}\mathbf{u}_{(\alpha,k+1)} + m_e\mathbf{u}_e\right)\left(\Gamma^{\text{rec}}_{(\alpha,k+1)} + \Gamma^{\text{tbr}}_{(\alpha,k+1)}\right) + \sum_{s\in\Lambda_{\text{G}}\backslash(\alpha,k)} \mathbf{R}_{(\alpha,k);s} + \boldsymbol{\mathcal{C}}^{\text{cx},[1]}_{(\alpha,k)}\end{aligned} \tag{9b}$$

for the atomic species, where

$$\boldsymbol{\mathcal{C}}^{\text{cx},[1]}_{(\alpha,k)} = \begin{cases} -\sum_{\ell=1}^{z_\alpha} \boldsymbol{\mathcal{C}}^{\text{cx},[1]}_{(\alpha,\ell)}, & k=0, \\ m_{(\alpha,k)}\left(\mathbf{u}_{(\alpha,0)} - \mathbf{u}_{(\alpha,k)}\right)\Gamma^{\text{cx}}_{(\alpha,k)} + \mathbf{R}^{\text{cx}}_{(\alpha,k);(\alpha,0)} - \mathbf{R}^{\text{cx}}_{(\alpha,0);(\alpha,k)}, & k>0, \end{cases} \tag{9c}$$

and $\Gamma^{\text{cx}}_{(\alpha,k)}$ is the charge exchange rate parameter.

Exchange of energy. Written out term-by-term, the collision sources $\mathcal{C}_s^{[2]}$ have the form[1]

$$\begin{aligned}\mathcal{C}_e^{[2]} = {} & \sum_{\substack{(\alpha,k)\in\mathcal{N}_S \\ k\neq z_\alpha}} \left(\tfrac{1}{2}m_e\mathbf{u}^2_{(\alpha,k)} + m_e e_{(\alpha,k)} - \phi^{\text{ion}}_{(\alpha,k)}\right)\Gamma^{\text{ion}}_{(\alpha,k)} - \left(\tfrac{1}{2}m_e\mathbf{u}_e^2 + m_e e_e\right)\sum_{\substack{(\alpha,k)\in\mathcal{N}_s \\ k\neq 0}}\left(\Gamma^{\text{rec}}_{(\alpha,k)} + \Gamma^{\text{tbr}}_{(\alpha,k)}\right) \\ & + \sum_{(\alpha,k)\in\mathcal{N}_S}\left(\mathbf{u}_e\cdot\mathbf{R}_{e;(\alpha,k)} + Q_{e;(\alpha,k)}\right) + Q_e^{\text{rad}}\end{aligned} \tag{10a}$$

for the electron species, and

$$\begin{aligned}\mathcal{C}^{[2]}_{(\alpha,k)} = {} & \left(\tfrac{1}{2}m_{(\alpha,k)}\mathbf{u}^2_{(\alpha,k-1)} + m_{(\alpha,k)}e_{(\alpha,k-1)}\right)\Gamma^{\text{ion}}_{(\alpha,k-1)} - \left(\tfrac{1}{2}m_{(\alpha,k)}\mathbf{u}^2_{(\alpha,k)} + m_{(\alpha,k)}e_{(\alpha,k)}\right)\left(\Gamma^{\text{ion}}_{(\alpha,k)} + \Gamma^{\text{rec}}_{(\alpha,k)} + \Gamma^{\text{tbr}}_{(\alpha,k)}\right) \\ & + \left(\tfrac{1}{2}m_{(\alpha,k+1)}\mathbf{u}^2_{(\alpha,k+1)} + m_{(\alpha,k+1)}e_{(\alpha,k+1)} + \tfrac{1}{2}m_e\mathbf{u}_e^2 + m_e e_e\right)\left(\Gamma^{\text{rec}}_{(\alpha,k+1)} + \Gamma^{\text{tbr}}_{(\alpha,k+1)}\right) + \phi^{\text{ion}}_{(\alpha,k)}\Gamma^{\text{tbr}}_{(\alpha,k+1)} \\ & + \sum_{s\in\Lambda_{\text{G}}\backslash(\alpha,k)}\left(\mathbf{u}_{(\alpha,k)}\cdot\mathbf{R}_{(\alpha,k);s} + Q_{(\alpha,k);s}\right) + \mathcal{C}^{\text{cx},[2]}_{(\alpha,k)} + Q^{\text{rad}}_{(\alpha,k)}\end{aligned} \tag{10b}$$

[1] The forms of the ionization, recombination, and charge exchange sources largely follows that of [64, 65], with the exception that the terms representing the transfer of thermal energy are written in terms of the specific internal energy e_s of each species instead of the fluid temperature T_s. Whereas [64, 65] assumes only an idea gas, our formulation permits a more general form of the expression for internal energy.

for the atomic species, where

$$\mathcal{C}^{\mathrm{cx},[2]}_{(\alpha,k)} = \begin{cases} -\sum_{\ell=1}^{z_\alpha} \mathcal{C}^{\mathrm{cx},[2]}_{(\alpha,k)}, & k=0, \\ \frac{1}{2} m_{(\alpha,k)} \left(\mathbf{u}^2_{(\alpha,0)} - \mathbf{u}^2_{(\alpha,k)} \right) \Gamma^{\mathrm{cx}}_{(\alpha,k)} + \mathbf{u}_{(\alpha,0)} \cdot \mathbf{R}^{\mathrm{cx}}_{(\alpha,k);(\alpha,0)} - \mathbf{u}_{(\alpha,k)} \cdot \mathbf{R}^{\mathrm{cx}}_{(\alpha,0);(\alpha,k)} & \\ \quad + Q^{\mathrm{cx}}_{(\alpha,k);(\alpha,0)} - Q^{\mathrm{cx}}_{(\alpha,0);(\alpha,k)}, & k>0. \end{cases} \tag{10c}$$

Here $Q^{\mathrm{rad}}_e, Q^{\mathrm{rad}}_{(\alpha,k)}$ represent sources or losses of energy through radiative processes (eg., bremsstrahlung, line radiation, emission from recombination, etc.) and $\phi^{\mathrm{ion}}_{(\alpha,k)}$ denotes the ionization potential[2] for species (α,k). It should be noted that the form of $\mathcal{C}^{[2]}_{(\alpha,k)}$ in (10b) is such that the ionization energy associated with radiative and dielectronic recombination reactions is always assumed to be lost as a radiative emission. Further losses as a result of these reactions, typically as a function of the electron internal energy [64, 65], would be included as additional terms in $Q^{\mathrm{rad}}_{(\alpha,k)}$.

2.1.2. Conserved quantities notation

Mass exchange. In terms of conserved quantities, the collision sources $\mathcal{C}^{[0]}_s$ can be written as

$$\mathcal{C}^{[0]}_e = \rho_e \sum_{\substack{(\alpha,k)\in\mathcal{N}_S \\ k\neq z_\alpha}} \frac{\rho_{(\alpha,k)}}{m_{(\alpha,k)}} I_{(\alpha,k)} - \rho_e \sum_{\substack{(\alpha,k)\in\mathcal{N}_S \\ k\neq 0}} \frac{\rho_{(\alpha,k)}}{m_{(\alpha,k)}} \left(R_{(\alpha,k)} + \frac{\rho_e}{m_e} R^{\mathrm{tbr}}_{(\alpha,k)} \right) \tag{11a}$$

for the electron species, and

$$\begin{aligned} \mathcal{C}^{[0]}_{(\alpha,k)} = {} & \frac{m_{(\alpha,k)}}{m_{(\alpha,k-1)}} \frac{\rho_e}{m_e} \rho_{(\alpha,k-1)} I_{(\alpha,k-1)} - \frac{\rho_e}{m_e} \rho_{(\alpha,k)} I_{(\alpha,k)} \\ & + \frac{m_{(\alpha,k)}}{m_{(\alpha,k+1)}} \frac{\rho_e}{m_e} \rho_{(\alpha,k+1)} \left(R_{(\alpha,k+1)} + \frac{\rho_e}{m_e} R^{\mathrm{tbr}}_{(\alpha,k+1)} \right) - \frac{\rho_e}{m_e} \rho_{(\alpha,k)} \left(R_{(\alpha,k)} + \frac{\rho_e}{m_e} R^{\mathrm{tbr}}_{(\alpha,k)} \right) \end{aligned} \tag{11b}$$

for the atomic species

Exchange of momentum. In terms of conserved quantities, the collision sources $\boldsymbol{\mathcal{C}}^{[1]}_s$ can be written as

$$\boldsymbol{\mathcal{C}}^{[1]}_e = \rho_e \sum_{\substack{(\alpha,k)\in\mathcal{N}_S \\ k\neq z_\alpha}} \frac{(\rho\mathbf{u})_{(\alpha,k)}}{m_{(\alpha,k)}} I_{(\alpha,k)} - (\rho\mathbf{u})_e \sum_{\substack{(\alpha,k)\in\mathcal{N}_S \\ k\neq 0}} \frac{\rho_{(\alpha,k)}}{m_{(\alpha,k)}} \left(R_{(\alpha,k)} + \frac{\rho_e}{m_e} R^{\mathrm{tbr}}_{(\alpha,k)} \right) + \sum_{(\alpha,k)\in\mathcal{N}_S} \mathbf{R}_{e;(\alpha,k)} \tag{12a}$$

for the electron species, and

$$\begin{aligned} \boldsymbol{\mathcal{C}}^{[1]}_{(\alpha,k)} = {} & \frac{m_{(\alpha,k)}}{m_{(\alpha,k-1)}} \frac{\rho_e}{m_e} (\rho\mathbf{u})_{(\alpha,k-1)} I_{(\alpha,k-1)} - \frac{\rho_e}{m_e} (\rho\mathbf{u})_{(\alpha,k)} I_{(\alpha,k)} \\ & + \left(\frac{\rho_e}{m_e} (\rho\mathbf{u})_{(\alpha,k+1)} + \frac{\rho_{(\alpha,k+1)}}{m_{(\alpha,k+1)}} (\rho\mathbf{u})_e \right) \left(R_{(\alpha,k+1)} + \frac{\rho_e}{m_e} R^{\mathrm{tbr}}_{(\alpha,k+1)} \right) \\ & - \frac{\rho_e}{m_e} (\rho\mathbf{u})_{(\alpha,k)} \left(R_{(\alpha,k)} + \frac{\rho_e}{m_e} R^{\mathrm{tbr}}_{(\alpha,k)} \right) + \sum_{s\in\Lambda_{\mathrm{G}}\succ(\alpha,k)} \mathbf{R}_{(\alpha,k);s} + \boldsymbol{\mathcal{C}}^{\mathrm{cx},[1]}_{(\alpha,k)} \end{aligned} \tag{12b}$$

for the atomic species.

[2] Instead of the ground-state ionization potential $\phi^{\mathrm{ion}}_{(\alpha,k)}$, the authors of [65] use an effective ionization potential $\phi^{\mathrm{eff}}_{(\alpha,k)}$ that "approximately includes the electron binding energy plus the excitation energy that is expended (on average) for each ionization event," and additionally includes contributions from the dissociation of diatomic gases. We have excluded these additional contributions since (i) they are highly uncertain and serve as only very rough approximations of reality, and (ii) these contributions would not apply in many of our applications of interest.

Exchange of energy. In terms of conserved quantities, the collision sources $\mathcal{C}_s^{[2]}$ can be written as

$$\begin{aligned}\mathcal{C}_e^{[2]} = \rho_e \sum_{\substack{(\alpha,k)\in\mathcal{N}_S \\ k\neq z_\alpha}} \frac{\mathcal{E}_{(\alpha,k)}}{m_{(\alpha,k)}} I_{(\alpha,k)} - \frac{\rho_e}{m_e} \sum_{\substack{(\alpha,k)\in\mathcal{N}_S \\ k\neq z_\alpha}} \frac{\rho_{(\alpha,k)}}{m_{(\alpha,k)}} \phi^{\text{ion}}_{(\alpha,k)} I_{(\alpha,k)} - \mathcal{E}_e \sum_{\substack{(\alpha,k)\in\mathcal{N}_S \\ k\neq 0}} \frac{\rho_{(\alpha,k)}}{m_{(\alpha,k)}} \left(R_{(\alpha,k)} + \frac{\rho_e}{m_e} R^{\text{tbr}}_{(\alpha,k)} \right) \\ + \sum_{(\alpha,k)\in\mathcal{N}_S} \left(\frac{(\rho\mathbf{u})_e}{\rho_e} \cdot \mathbf{R}_{e;(\alpha,k)} + Q_{e;(\alpha,k)} \right) + Q_e^{\text{rad}}\end{aligned} \tag{13a}$$

for the electron species, and

$$\begin{aligned}\mathcal{C}^{[2]}_{(\alpha,k)} = \frac{m_{(\alpha,k)}}{m_{(\alpha,k-1)}} \frac{\rho_e}{m_e} \mathcal{E}_{(\alpha,k-1)} I_{(\alpha,k-1)} - \frac{\rho_e}{m_e} \mathcal{E}_{(\alpha,k)} I_{(\alpha,k)} + \frac{\rho_e^2}{m_e^2} \frac{\rho_{(\alpha,k+1)}}{m_{(\alpha,k+1)}} \phi^{\text{ion}}_{(\alpha,k)} R^{\text{tbr}}_{(\alpha,k+1)} \\ + \left(\frac{\rho_e}{m_e} \mathcal{E}_{(\alpha,k+1)} + \frac{\rho_{(\alpha,k+1)}}{m_{(\alpha,k+1)}} \mathcal{E}_e \right) \left(R_{(\alpha,k+1)} + \frac{\rho_e}{m_e} R^{\text{tbr}}_{(\alpha,k+1)} \right) - \frac{\rho_e}{m_e} \mathcal{E}_{(\alpha,k)} \left(R_{(\alpha,k)} + \frac{\rho_e}{m_e} R^{\text{tbr}}_{(\alpha,k)} \right) \\ + \sum_{s\in\Lambda_G{}_\succ(\alpha,k)} \left(\frac{(\rho\mathbf{u})_{(\alpha,k)}}{\rho_{(\alpha,k)}} \cdot \mathbf{R}_{(\alpha,k);s} + Q_{(\alpha,k);s} \right) + \mathcal{C}^{\text{cx},[2]}_{(\alpha,k)} + Q^{\text{rad}}_{(\alpha,k)}\end{aligned} \tag{13b}$$

for the atomic species.

Further consideration is paid to the charge-exchange and elastic scattering terms in section 2.2, where their full definition for specific models is given.

2.2. Collisional transfer models

We now turn our attention to specifying values for collisional transfer coefficients that appear in $\mathcal{C}_s^{[0]}$, $\boldsymbol{\mathcal{C}}_s^{[1]}$, and $\mathcal{C}_s^{[2]}$. Our focus here is on analytic models from which derivatives may be obtained for the assembly of Jacobian matrices used for the solution of nonlinear systems resulting from implicit time discretization of the multifluid system. In Drekar, these Jacobian matrices are constructed using automatic differentiation [27, 75]. Future work will explore using collisional transfer coefficients provided by libraries such as the FLYCHK library [22], which may not provide derivative information or support general interfaces that can leverage the automatic differentiation libraries that are currently used in Drekar to construct the necessary Jacobian matrices.

The collisional transfer models considered here focus primarily on the lower-density, optically-thin coronal limit. In this limit, photons do not interact with the plasma after they are emitted (hence photoionization is neglected), excited states are assumed to be unpopulated and transitions between charge states are assumed to occur from the ground state, and higher-density effects such as three-body recombination are generally neglected.

We have begun initial efforts to explore extending these models to include some higher-density effects such as ionization potential depression and three-body recombination. At this time, the implementation of ionization potential depression and three-body recombination models is still under development, and has not been tested within Drekar. The mathematical approaches described here for these models should therefore be considered exploratory in nature, and largely untested and unverified. Further, it should be noted that these effects represent only a limited selection of the models that should be included to accurately model plasmas in the regimes in which these effects would be important.

2.2.1. Ionization rate

The ionization rate parameter $I_{(\alpha,k)}$ specifies the ionization rate of atomic species α from charge state k to $k+1$ by electron-impact ionization. We consider the following functional forms for ionization rate parameters:

(i) Mattioli, et al. [63] have generated coefficients for functional fits of the form

$$I_{(\alpha,k)} = 10^{-11} T_e^{-1/2} \sum_{i=1}^{N_{(\alpha,k)}} c_i^{(\alpha,k)} \exp\left(-E_i^{(\alpha,k)} / T_e \right) \tag{14}$$

based on the data of Loch, et al. [53] for all charge states of Kr, where $c_i^{(\alpha,k)}$, $E_i^{(\alpha,k)}$, and $N_{(\alpha,k)}$ are tabulated fit parameters. The expression (14) is given in units of $\mathrm{cm}^3\mathrm{s}^{-1}$, and the electron temperature T_e is expected in units of eV.

(ii) Voronov [96] provides coefficients for functional fits of the form

$$I_{(\alpha,k)} = A_{(\alpha,k)} \frac{1 + P_{(\alpha,k)} \sqrt{U_{(\alpha,k)}}}{X_{(\alpha,k)} + U_{(\alpha,k)}} \left(U_{(\alpha,k)}\right)^{K_{(\alpha,k)}} \exp\left(-U_{(\alpha,k)}\right). \tag{15}$$

Here $U_{(\alpha,k)} = \phi^{\mathrm{ion}}_{(\alpha,k)} / T_e$ is the (dimensionless) relative temperature, $\phi^{\mathrm{ion}}_{(\alpha,k)}$ is the ionization energy for species α and charge state k, and $A_{(\alpha,k)}$, $K_{(\alpha,k)}$, $P_{(\alpha,k)}$, and $X_{(\alpha,k)}$ are tabulated fit parameters. The expression (15) is given in units of $\mathrm{cm}^3\mathrm{s}^{-1}$. Fit parameters are found in [96] for over 400 cases from H to Ni^{27+} that are (in most cases) accurate to within 10% for temperatures between 1 eV and 20 KeV. For some ions of higher charge states, the fit parameters are computed for temperature ranges up to 100 KeV.

Sterling, et al. [87] have computed additional coefficients using Voronov's fit formula for all charge states of Kr. We note that there appears to be an inconsistency in the units used for computing the fit coefficients in [87], as direct application of these coefficients seems to yield unusual results. We have inferred that the fit coefficients computed in [87] expect that inside of the exponential term $U_{(\alpha,k)}$ is computed with T_e given in units of eV, but all other values of $U_{(\alpha,k)}$ are computed with T_e given in units of degrees Kelvin. To ensure consistency, we scale the coefficients of [87] as follows, so that $U_{(\alpha,k)}$ is always computed with T_e given in units of eV:

$$X_{(\alpha,k)} = E \hat{X}_{(\alpha,k)}, \qquad A_{(\alpha,k)} = E^{1-K_{(\alpha,k)}} \hat{A}_{(\alpha,k)}, \tag{16}$$

where $X_{(\alpha,k)}$ and $A_{(\alpha,k)}$ are the scaled values used, $\hat{X}_{(\alpha,k)}$ and $\hat{A}_{(\alpha,k)}$ are the original values from [87], and $E = 1.16045221\mathrm{E}{+4}$ is the conversion factor from units of eV to degrees Kelvin. Using these adjusted values yields ionization rates with the expected behavior.

(iii) The following functional approximation from Lotz [54, 55] may also be used:

$$I_{(\alpha,k)} = (2.97\mathrm{E}{-6}) \frac{\xi_{(\alpha,k)}}{\phi^{\mathrm{ion}}_{(\alpha,k)} \sqrt{T_e}} E_1\left(U_{(\alpha,k)}\right), \tag{17}$$

where $\xi_{(\alpha,k)}$ is the number of electrons in the outer shell of the atom being ionized, $U_{(\alpha,k)} = \phi^{\mathrm{ion}}_{(\alpha,k)} / T_e$, and E_1 is the exponential integral of the first kind. The expression (17) is given in units of $\mathrm{cm}^3\mathrm{s}^{-1}$, and the leading constant is chosen for $\phi^{\mathrm{ion}}_{(\alpha,k)}$ and T_e both in units of eV. One important advantage of this formula is that as the ionization energy $\phi^{\mathrm{ion}}_{(\alpha,k)}$ approaches zero, the ionization rate $I_{(\alpha,k)}$ monotonically approaches infinity. This ionization model may therefore be combined with models for ionization potential depression to capture effects of pressure ionization phenomena in high-density plasmas, as is done, for example, in the FLYCHK library [22]. Other ionization models, such as the fits of Voronov, are not appropriate for use with modified ionization energies and are not well-behaved in this limit.

Implementation. We use the following combination of approximations from [2], originally sourced from [4] and [38], respectively, in order to evaluate the exponential integral term:

$$E_1(x) \approx \begin{cases} -\ln x + a_0 + a_1 x + a_2 x^2 + a_3 x^3 + a_4 x^4 + a_5 x^5, & x \le 1, \\ \dfrac{e^{-x}}{x} \dfrac{x^2 + c_1 x + c_2}{x^2 + b_1 x + b_2}, & x \ge 1, \end{cases} \tag{18}$$

with

$$a_0 = -0.57721566, \qquad b_1 = 3.330657, \tag{19a}$$
$$a_1 = \ \ 0.99999193, \qquad b_2 = 1.681534, \tag{19b}$$
$$a_2 = -0.24991055, \tag{19c}$$
$$a_3 = \ \ 0.05519968, \tag{19d}$$
$$a_4 = -0.00976004, \qquad c_1 = 2.334733, \tag{19e}$$
$$a_5 = \ \ 0.00107857, \qquad c_2 = 0.250621. \tag{19f}$$

This approximation has an absolute error of less than 5.0E−5 over the entire real axis. Note that this piecewise approximation is continuous, but it's first derivative is discontinuous at $x = 1$.

2.2.2. Recombination rate

We treat the total recombination rate as a sum of two components: $R_{(\alpha,k)}$ specifies the recombination rate of atomic species α from charge state k to $k-1$ due to radiative (RR) and dielectronic recombination (DR), and $R^{\text{tbr}}_{(\alpha,k)}$ specifies the recombination rate due to three-body recombination (TBR). It should be noted that dielectronic recombination only applies to cases in which the reactant atom contains one or more bound electrons. We consider multiple sources of data for each recombination rate parameter. Where data from preferred sources is unavailable, alternative sources are used. In general, dielectronic recombination rates can be effectively suppressed by sufficiently high electron densities [70, 71], but we have not included such effects at this time.

Radiative recombination. We leverage the following sources of data for radiative recombination, in order of preference:

(i) Badnell [13] provides coefficients for fits based on the functional form of Verner and Ferland [95], which can be written as

$$R^{\text{rad}}_{(\alpha,k)} = A_{(\alpha,k)} \left[\sqrt{T_e / T_0^{(\alpha,k)}} \left(1 + \sqrt{T_e / T_0^{(\alpha,k)}}\right)^{1-D_{(\alpha,k)}} \left(1 + \sqrt{T_e / T_1^{(\alpha,k)}}\right)^{1+D_{(\alpha,k)}} \right]^{-1}, \tag{20a}$$

where

$$D_{(\alpha,k)} = B_{(\alpha,k)} + C_{(\alpha,k)} \exp\left(-T_2^{(\alpha,k)} / T_e\right) \tag{20b}$$

is the modified exponential coefficient introduced by Gu [33], and $A_{(\alpha,k)}$, $B_{(\alpha,k)}$, $C_{(\alpha,k)}$, and $T_i^{(\alpha,k)}$ for $i = 0, 1, 2$ are tabulated fit parameters. Except for some low-charge ions, it is usually the case that $C_{(\alpha,k)} = T_2^{(\alpha,k)} = 0$, in which case $D_{(\alpha,k)} = B_{(\alpha,k)}$. The expression (20) is given in units of cm^3s^{-1}, and coefficients are provided for electron temperatures in units of eV or K. Fits are provided for all elements up to Zn (inclusive), plus Kr, Mo, and Xe, for all isoelectronic sequences up to Na-like forming Mg-like. The fits are claimed to be accurate for electron temperatures between $10\,k^2$ and $10^7\,k^2$ degrees Kelvin to within 1% for multiply charged ions and 5% for singly and doubly ionized states. Further, the fit formula is designed to produce the correct asymptotic forms outside of these temperature ranges in both the low- and high-temperature limits.

(ii) Sterling [86] has computed fit coefficients for Kr^+ through Kr^{6+} using a two-part formula. The formula consists of a fit of the form (20) that, for certain ions, is combined with a fit of the form (25) above some specified temperature. These fits yield rates in units of cm^3s^{-1} and expect electron temperatures in units of degrees Kelvin.

(iii) Mattioli, et al. [63] provide fit coefficients for all charge states of Kr using the original functional form of Verner and Ferland [95] (ie., the formula (20) with $D_{(\alpha,k)} = B_{(\alpha,k)}$). The coefficients generate rates in units of cm^3s^{-1} with electron temperatures expected in units of eV.

(iv) Kotelnikov, et al. [45] supply the following approximate analytic formula based on a hydrogenic approximation:

$$R^{\text{rad}}_{(\alpha,k)} = \frac{8.414 k\alpha^4 c a_0^2 \left[\ln(1+\lambda) + 3.499\right]}{(1/\lambda)^{1/2} + 0.6517\,(1/\lambda) + 0.2138\,(1/\lambda)^{3/2}}, \tag{21a}$$

where α is the fine-structure constant, a_0 is the Bohr radius, c is the speed of light in vacuum, and

$$\lambda = \frac{h R_\infty c k^2}{k_{\text{B}} T_e}, \tag{21b}$$

with h, k_{B}, and R_∞ representing the Planck, Boltzmann, and Rydberg constants, respectively. When using standard SI units for all supplementary constants, the expression (21a) yields rates in units of m^3s^{-1}. The accuracy of this formula is expected to be within 3% for $1.0\text{E}{-4} < \lambda < 1.0\text{E}{+4}$. Unlike some radiative recombination rate formulas, this formula yields rates $R^{\text{rad}}_{(\alpha,k)} \propto T_e^{-1/2}$ and $R^{\text{rad}}_{(\alpha,k)} \propto T_e^{-3/2}$ in the low- and high-temperature limits, respectively, so that reasonable (though not necessarily accurate) rates are obtained outside of the targeted temperature range in both limits.

Implementation. For electron temperatures given in units of degrees Kelvin, we may write

$$A = (8.141\text{E}{+6})\, k\alpha^4 c a_0^2 = (2.0030269543112400\text{E}{-14})\, k, \tag{22a}$$

$$B = (1.5788750459524500\text{E}{+5})\, k^2, \tag{22b}$$

$$\lambda = B/T_e. \tag{22c}$$

Then the expression

$$R^{\text{rad}}_{(\alpha,k)} = A \frac{\ln(1+\lambda) + 3.499}{(1/\lambda)^{1/2} + 0.6517\,(1/\lambda) + 0.2138\,(1/\lambda)^{3/2}} \tag{23}$$

yields recombination rates in units of cm^3s^{-1}.

(v) Landini, et al. [49, 50] provide coefficients for functional fits of the form

$$R^{\text{rad}}_{(\alpha,k)} = A_{(\alpha,k)}\,(T_e * 1.0\text{E}{-4})^{-X_{(\alpha,k)}}, \tag{24}$$

where $A_{(\alpha,k)}$ and $X_{(\alpha,k)}$ are tabulated fit parameters. The expression (24) is given in units of cm^3s^{-1}, and the electron temperature T_e is expected in units of degrees Kelvin. Because the functional form of these fits contains only a single, constant exponent, this formula cannot reproduce the asymptotic behavior expected in the low- and high-temperature limits. However, data are provided for lower ionization states of some heavier atomic species not found in other sources – in particular, S, Cl, Ar, K, Ca, Ti, Cr, Mn, Fe, Co, and Ni.

Dielectronic recombination. We leverage the following sources of data for dielectronic recombination, in order of preference:

(i) In a sequence of papers, [1, 5, 6, 7, 8, 12, 14, 17, 24, 25, 26, 42, 68, 100, 101, 102, 103] Badnell, et al. provide coefficients for functional fits of the form

$$R^{\text{die}}_{(\alpha,k)} = T_e^{-3/2} \sum_{i=1}^{N_{(\alpha,k)}} c_i^{(\alpha,k)} \exp\left(-E_i^{(\alpha,k)}/T_e\right), \tag{25}$$

where $c_i^{(\alpha,k)}$, $E_i^{(\alpha,k)}$, and $N_{(\alpha,k)}$ are tabulated fit parameters. The expression (25) is given in units of cm^3s^{-1}, and the electron temperature is expected in units of degrees Kelvin. The fits are generated using data obtained from atomic structure calculations, and are claimed to reproduce the computed data on which they are based to within 5% in general, and in most cases to within 1%.

(ii) Sterling [86] has computed fit coefficients for Kr^+ through Kr^{6+} using the formula (25). Similar to other sources, these fits yield rates in units of cm^3s^{-1}. The coefficients are given for electron temperatures in units of degrees Kelvin, but may be easily converted for units of eV.

(iii) Mattioli, et al. [63] provide fit coefficients for all charge states of Kr using a functional fit of the form (25). The coefficients generate rates in units of $\mathrm{cm}^3\mathrm{s}^{-1}$ with electron temperatures expected in units of eV.

(iv) Landini, et al. [49, 50] provide coefficients for fits of the form

$$R^{\mathrm{die}}_{(\alpha,k)} = A_{(\alpha,k)}\, T_e^{-3/2} \exp\left(-T_0^{(\alpha,k)}/T_e\right)\left(1 + B_{(\alpha,k)} \exp\left(-T_1^{(\alpha,k)}/T_e\right)\right), \tag{26}$$

where $A_{(\alpha,k)}$, $B_{(\alpha,k)}$, $T_0^{(\alpha,k)}$, and $T_1^{(\alpha,k)}$ are tabulated fit parameters. The expression (26) is given in units of $\mathrm{cm}^3\mathrm{s}^{-1}$, and the electron temperature is expected in units of degrees Kelvin. While believed to be generally less accurate than the formula (25), the fits of Landini, et al. can be used as a substitute for data not provided by Badnell, et al. for lower ionization states of some heavier atomic species – in particular, S, Cl, Ar, K, Ca, Ti, Cr, Mn, Fe, Co, and Ni.

(v) A collection of semi-empirical models are given by Hahn [34, 35] based on fitting data by excitation mode rather than isoelectronic sequence. The total dielectronic rate coefficient is decomposed as

$$R^{\mathrm{die}}_{(\alpha,k)} = \alpha_{1\mathrm{s}} + \alpha_{2\mathrm{s}} + \alpha_{2\mathrm{p}} + \alpha_{3\mathrm{s}} + \alpha_{3\mathrm{p}}, \tag{27}$$

where the parameters α_* represent the contribution of dielectronic recombination due to electron excitation from the 1s, 2s, 2p, 3s, and 3p orbitals, respectively. The individual rates are given by

$$\alpha_{1\mathrm{s}} = A_1\, T_e^{-3/2} \exp\left(-A_2/T_e\right) \exp\left(-A_3\,(N-2)^2\right)\left(\frac{6}{4+N}\right)^{0.9}, \tag{28a}$$

$$\alpha_{2\mathrm{s}} = B_1\, T_e^{-3/2} \exp\left(-B_2/T_e\right)(N-2)\,(10-N)\,(N+B_3)^{-2.5}\left(1 + 0.3\,T_e^{-0.21}\right), \tag{28b}$$

$$\alpha_{2\mathrm{p}} = C_1\, T_e^{-3/2} \exp\left(-\frac{C_2}{T_e}\left(1 + \frac{0.0001}{N+1}\right)\right) \exp\left(-C_3|N-9.6|\right)\sqrt{\frac{10}{N+1}}, \tag{28c}$$

$$\alpha_{3\mathrm{s}} = D_1\, T_e^{-3/2} \exp\left(-\frac{D_2}{T_e}\left(1.0 - \frac{0.15}{(N-10)^{1.5}}\right)\right)\frac{(N-10)\,(Z_c-N)}{N-D_3}, \tag{28d}$$

$$\alpha_{3\mathrm{p}} = E_1\, T_e^{-3/2} \exp\left(-E_2/T_e\right) \exp\left(-E_3\,(N-12)^2\right)(N-10)\,(Z_c-10)\,\frac{1}{8}, \tag{28e}$$

where N is the number of electrons in the recombining ion, Z_c is the nuclear core charge of the recombining ion, $Z = Z_c - 2$, $Z' = Z_c - 10$, $Z'' = Z_c - 7$, and

$$A_1 = 1230 \exp\left(-\frac{44}{Z_c + 2.86}\right) Z_c^{-0.14}, \tag{29a}$$

$$A_2 = (0.0075)\,(Z_c + 1/N)^2, \tag{29b}$$

$$A_3 = 0.0222\, Z_c, \tag{29c}$$

$$B_1 = 52 \exp\left(-\frac{18}{1+Z}\right)\left(\frac{Z_c}{10 + 0.011\, Z_c^2}\right)^{0.65}, \tag{29d}$$

$$B_2 = \frac{0.0023\, Z}{1 + 0.0015\, Z^2}, \tag{29e}$$

$$B_3 = 0.8, \tag{29f}$$

$$C_1 = 2.15 \exp\left(-0.004\,(Z-35)^2\right) Z^{1.8}, \tag{29g}$$

$$C_2 = (0.00115)\, Z^2\,(1 - 0.003 Z), \tag{29h}$$

$$C_3 = 0.17, \tag{29i}$$

$$D_1 = (0.16)\left(Z'\right)^2 \exp\left(-0.11\, Z'\right), \tag{29j}$$

$$D_2 = (0.0024)\, Z'\left(1 - 0.01 Z'\right), \tag{29k}$$

$$D_3 = 6, \tag{29l}$$

$$E_1 = \frac{0.45}{Z'} \exp\left(\frac{Z'}{4 + 0.02 Z'}\right), \tag{29m}$$

$$E_2 = 0.0003\left(Z''\right)^2\left(1 - 0.003Z''\right), \tag{29n}$$

$$E_3 = 0.02. \tag{29o}$$

For a given ion, at most three of the individual terms are included in the overall recombination rate. Specifically, α_{1s} should be taken to be zero unless $N < 10$, α_{2s} should be taken to be zero unless $2 < N < 10$, α_{2p} should be taken to be zero unless $N > 2$, and α_{3s} and α_{3p} should be taken to be zero unless $N > 10$.

These formulas are intended to be valid for a reasonably large range of ions. The author claims that these formulas should be reliable to within ±50% for $Z_c < 50$ and $N < 13$, when compared to the data used to generate the formulas. In our experience, these formulas appear to generate reasonable values for larger values of N, in the sense that the values generated are physically plausible (eg., nonnegative) with roughly reasonable profiles compared to other data sources, though the accuracy of the rates in this regime is questionable. Further, the use of a five-shell model neglects contributions from higher levels that are populated in ground-state ions with $N > 18$.

Three-body recombination. Rates for three-body recombination are obtained from collisional ionization rates using the principle of detailed balance. For a plasma in equilibrium, the collisional ionization and three-body recombination rates balance, so that

$$n_{(\alpha,k)} I_{(\alpha,k)} = n_{(\alpha,k)} n_e R^{\text{tbr}}_{(\alpha,k)} \tag{30a}$$

or

$$\frac{n_{(\alpha,k+1)} n_e}{n_{(\alpha,k)}} = \frac{I_{(\alpha,k)}}{R^{\text{tbr}}_{(\alpha,k+1)}}. \tag{30b}$$

Equating the right side of (30b) with the right side of the Saha equation

$$\frac{n_{(\alpha,k+1)} n_e}{n_{(\alpha,k)}} = \frac{2}{\lambda^3}\frac{g_{i+1}}{g_i}\exp\left(-\phi^{\text{ion}}_{(\alpha,k)}/T_e\right), \tag{31}$$

we find that

$$R^{\text{tbr}}_{(\alpha,k+1)} = \frac{\lambda^3}{2}\frac{g_{(\alpha,k+1)}}{g_{(\alpha,k)}} I_{(\alpha,k)} \exp\left(\phi^{\text{ion}}_{(\alpha,k)}/T_e\right), \tag{32}$$

where

$$\lambda^2 \stackrel{\text{def}}{=} \frac{h^2}{2\pi m_e k_{\text{B}} T_e} \tag{33}$$

is the thermal de Broglie wavelength of an electron, and $g_{(\alpha,k)}$ and $g_{(\alpha,k+1)}$ are the statistical weights (degeneracy of states) of the neighboring charge states.

For collisional ionizaton rates given using the formula of Lotz (17), the three-body recombination rate may be written as

$$R^{\text{tbr}}_{(\alpha,k+1)} = (4.92\text{E}{-}36)\frac{g_{(\alpha,k)}}{g_{(\alpha,k+1)}}\frac{\xi_{(\alpha,k)}}{\phi^{\text{ion}}_{(\alpha,k)} T_e^2} U\left(1,1,\phi^{\text{ion}}_{(\alpha,k)}/T_e\right), \tag{34}$$

where $U(a,b,x)$ is the confluent hypergeometric function of the second kind, which satisfies

$$U(1,1,x) = e^x E_1(x). \tag{35}$$

The formula (34) is given in units of cm^6s^{-1}, and the leading constant is chosen for $\phi^{\text{ion}}_{(\alpha,k)}$ and T_e in units of eV.

Implementation. It is important to note that the evaluation of (32) must be carefully considered for very low electron temperatures. When the electron temperature is very low, evaluation of the product $e^x E_1(x)$ as written (ie., as the product of two function evaluations) is numerically unstable. It is therefore important that some method for evaluating $U(1,1,x)$ be available. While many numerical libraries contain subroutines for evaluating functions of this type, we leverage the following modification of (18) to avoid introducing any

library dependencies:

$$U(1,1,x) \approx \begin{cases} e^x\left(-\ln x + a_0 + a_1 x + a_2 x^2 + a_3 x^3 + a_4 x^4 + a_5 x^5\right), & x \le 1, \\ \dfrac{1}{x}\dfrac{x^2 + c_1 x + c_2}{x^2 + b_1 x + b_2}, & x \ge 1, \end{cases} \tag{36}$$

with the parameters a_i, b_i, and c_i given previously in (19).

Implementation. For a given electron temperature, the equilibrium ionization fractions are typically vanishingly small outside of a limited range of charge states. When these models are implemented into fluid codes, difficulties with numerical precision can arise when very low ionization fractions are encountered. In an attempt to alleviate difficulties with low-density fluids and scaling issues between different fluids, a limiting procedure is applied to the ionization and recombination rates based on the densities of the reactants of each process.

Given a crossover value D and a slope p for the reactant number densities (eg. $D = 10^{10}$ m^{-3} and $p = 4$), the ionization and recombination rates $I_{(\alpha,k)}$ and $R_{(\alpha,k)}$ are replaced by the values $\eta I_{(\alpha,k)}$ and $\eta R_{(\alpha,k)}$, respectively, where

$$\eta \stackrel{\text{def}}{=} \frac{1}{1+r_e^p}\frac{1}{1+r_{(\alpha,k)}^p}, \qquad \text{with} \qquad r_s = \frac{D}{n_s}. \tag{37}$$

This results in the ionization and recombination rates being artificially suppressed when the reactant densities are very low, and effectively creates a number density floor for each species.

2.2.3. Ionization potential depression (IPD)

We leverage the ionization potential depression model of Stewart and Pyatt [88]. The amount by which the ionization energy is depressed is given by

$$\delta\phi_{(\alpha,k)}^{\text{ion}} = \frac{3(k+1)q_e^2}{8\pi\epsilon_0\lambda_{\text{D}}}\frac{\left[(a/\lambda_{\text{D}})^3+1\right]^{2/3}-1}{(a/\lambda_{\text{D}})^3}, \tag{38a}$$

where

$$a^3 \stackrel{\text{def}}{=} \frac{3(k+1)}{4\pi n_e}, \tag{38b}$$

$$\lambda_{\text{D}}^2 \stackrel{\text{def}}{=} \frac{\epsilon_0 k_{\text{B}}}{q_e^2}\left[\frac{n_e}{T_e} + \sum_{(\alpha,\ell)}\frac{\ell^2 n_{(\alpha,\ell)}}{T_{(\alpha,\ell)}}\right]^{-1}, \tag{38c}$$

are the ion sphere radius and the Debye length of the plasma, respectively. The standard ionization rate $\phi_{(\alpha,k)}^{\text{ion}}$ is then replaced by the depressed value

$$\hat{\phi}_{(\alpha,k)}^{\text{ion}} \stackrel{\text{def}}{=} \phi_{(\alpha,k)}^{\text{ion}} - \delta\phi_{(\alpha,k)}^{\text{ion}}. \tag{39}$$

This value is used in the formulas for computing rate coefficients for ionization and three-body recombination. It is important to note here that the ionization rate formula of Lotz (17) must be used if depressed ionization energy values are desired: The other sources of ionization rate coefficients discussed previously do not yield the correct behavior as $\hat{\phi}_{(\alpha,k)}^{\text{ion}} \to 0$.

2.2.4. Equilibrium ionization fractions (Coronal)

For comparison purposes, the equilibrium ionization fractions of several elements of interest have been computed using the previously discussed sources of ionization and recombination rate coefficients in the low-density (coronal) limit. In this case, only collisional ionization, radiative recombination, and dielectronic recombination are

Model	Species	Coefficient	Rate Preference
Generic	He, Be, Ne, Al, Ar, Kr	Ionization	Lotz
		RR	Kotelnikov
		DR	Hahn
Fit 1	Ne, Al, Ar	Ionization	Voronov
		RR	Landini, Kotelnikov
		DR	Landini
Fit 2	Kr	Ionization	Mattioli
		RR	Mattioli
		DR	Mattioli
Fit 3	He, Be, Ne, Al, Ar, Kr	Ionization	Mattioli, Voronov
		RR	Sterling, Badnell, Mattioli, Kotelnikov
		DR	Sterling, Badnell, Mattioli, Landini

TABLE 2.1. Summary of different sets of ionization and recombination rate coefficients used to compare the equilibrium ionization fractions of some elements of interest.

considered: the effects of three-body recombination and ionization potential depression are neglected. The ionization fractions are computed under a steady-state assumption using the approach described in section 3.2.1. Four combinations of ionization and recombination rates are considered, with most differences due to the choice of recombination rates:

- *Generic:* Consists of models that are all designed to be applied to wide ranges of atomic species. Specifically, the formulas of Lotz [54, 55], Kotelnikov, et al. [45], and Hahn [34, 35], for ionization, radiative recombination, and dielectronic recombination, respectively.
- *Fit 1:* Combines Voronov's analytic fit formulas for ionization [96] with the recombination rate fits of Landini, et al. [49, 50]. Since these references do not include rates for hydrogenic ions, we use the radiative recombination rate formula of Kotelnikov, et al. for these species. Applies only to those species of interest for which data is provided by Landini, et al. (ie., Ne, Al, Ar).
- *Fit 2:* Sources ionization, radiative recombination, and dielectronic recombination rates from the work of Mattioli, et al. [63]. Applies only to Kr.
- *Fit 3:* Uses our preferred recombination rates for all species of interest. Leverages the recombination rates of Badnell, et al. [1, 5, 6, 7, 8, 12, 13, 14, 17, 24, 25, 26, 42, 68, 100, 101, 102, 103] and Sterling, et al. [86] where available. When such rates are not available, the rates of Mattioli, et al. [63], Kotelnikov, et al., [45], and Landini, et al., [49, 50] are used, in that order.

The differences between each case are outlined in table 2.1. The ionization fractions and the corresponding average charge state for a some species of interest computed using each applicable set of ionization and recombination rates is shown in fig. 2.1. $\overline{Z}$ values computed by the FLYCHK library [22] in the low-density limit are included for comparison purposes.

2.2.5. Equilibrium ionization fractions (Higher-density)

The equilibrium ionization fractions of several elements of interest have been computed with high-density effects (ie., ionization potential depression and three-body recombination) included. All forms of ionization and recombination are considered, including collisional ionization and three-body recombination (both computed accounting for ionization potential depression) in addition to radiative and dielectronic recombination. Here the ionization rate formula of Lotz [54, 55] is used, with three-body recombination rates computed by detailed balance. Radiative and dielectronic recombination rates are computed using the fits of Badnell, et al. [1, 5, 6, 7, 8, 12, 13, 14, 17, 24, 25, 26, 42, 68, 100, 101, 102, 103] and Sterling, et al. [86] where available. When such rates are not available, the rates of

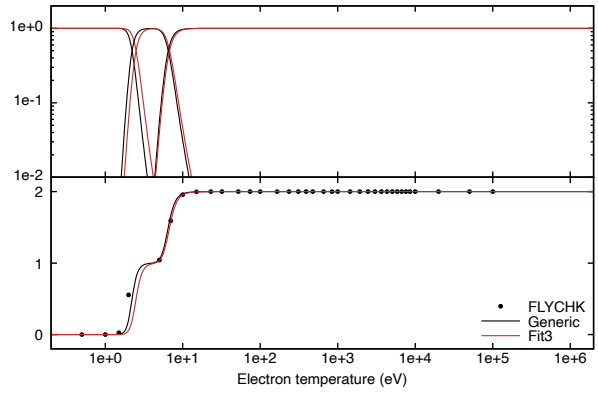

(A) He.

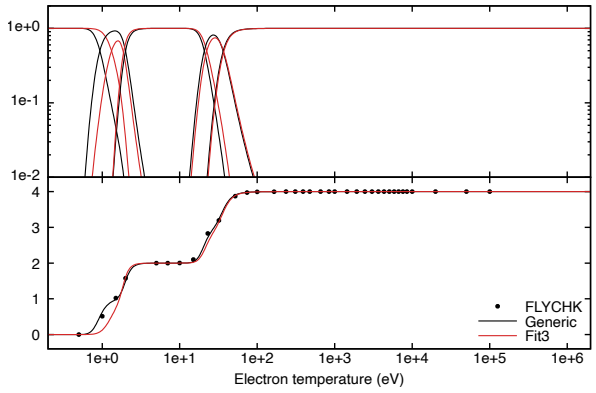

(B) Be.

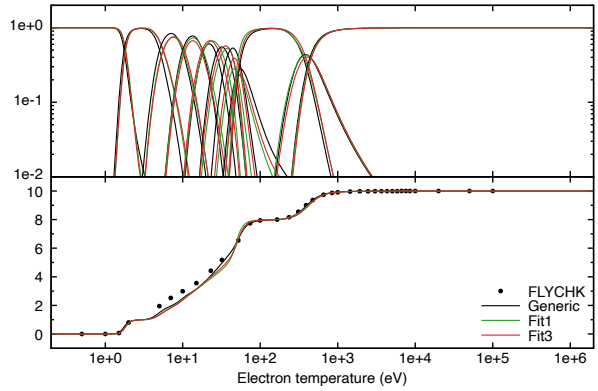

(C) Ne.

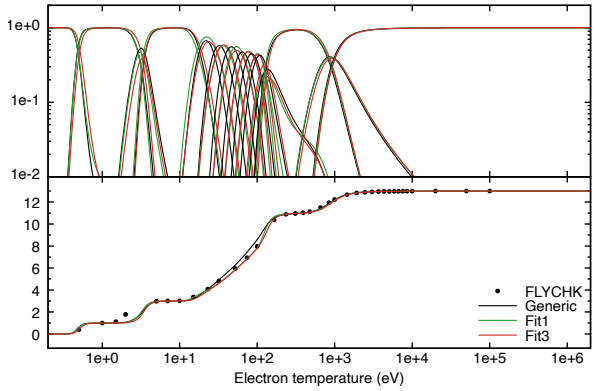

(D) Al.

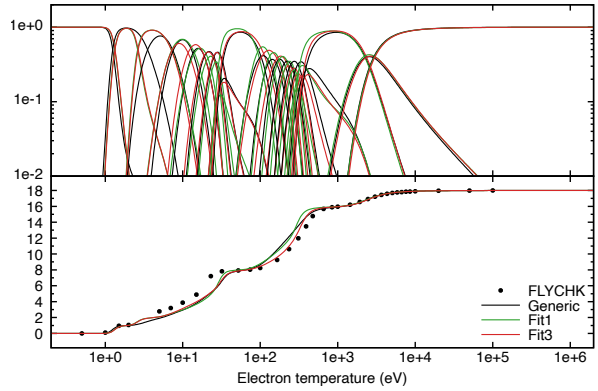

(E) Ar.

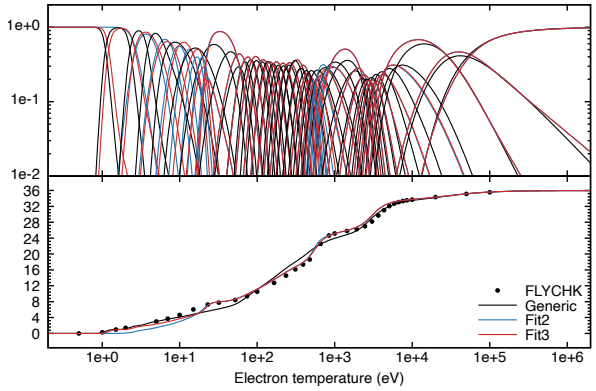

(F) Kr.

FIGURE 2.1. Comparison of equilibrium ionization fractions for various elements using different sources of ionization and recombination rate parameters in the low-density (coronal) limit. The various sources used for each case are summarized in table 2.1. Each plot shows the fraction of each charge state (top) and the resulting average charge state (bottom) for the models relevant to that atomic species. Select values for the average charge of each species computed using the FLYCHK library [22] at low density ($n_e = 10^{12}\,\mathrm{cm}^{-3}$) are included in the comparison.

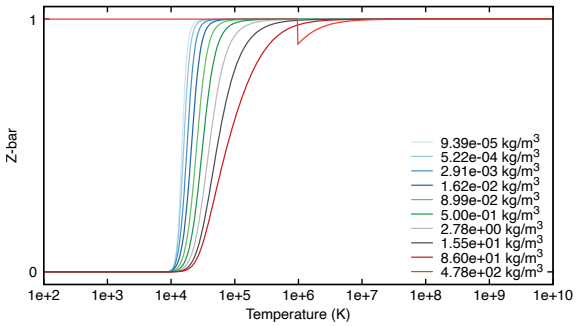

(A) H.

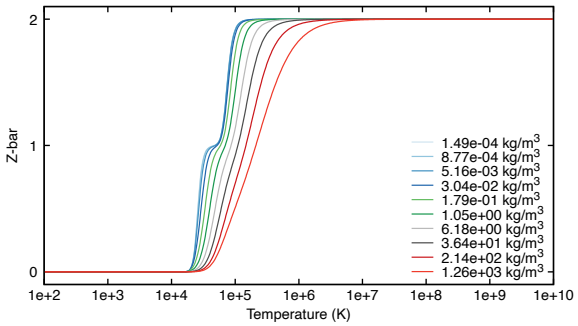

(B) He.

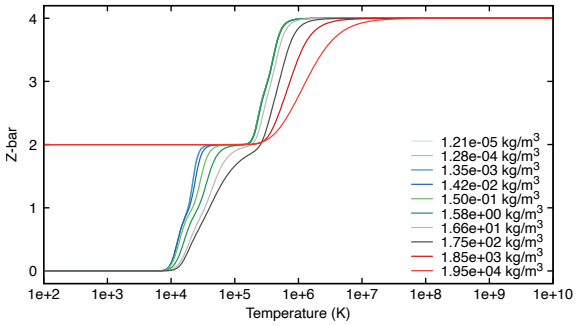

(C) Be.

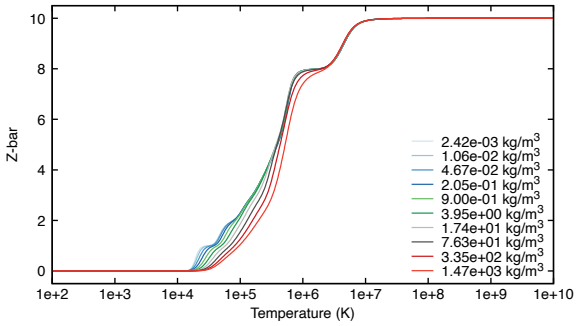

(D) Ne.

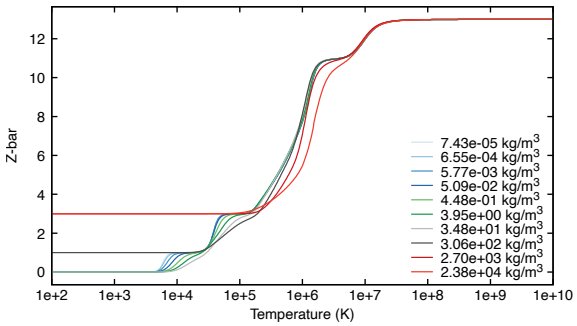

(E) Al.

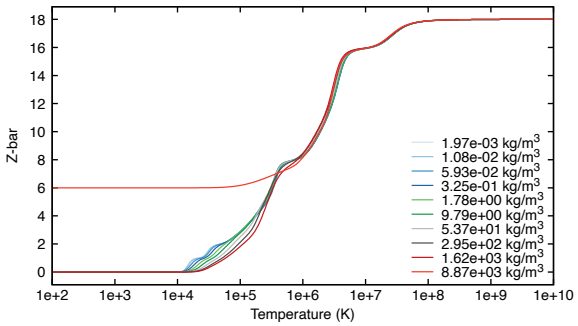

(F) Ar.

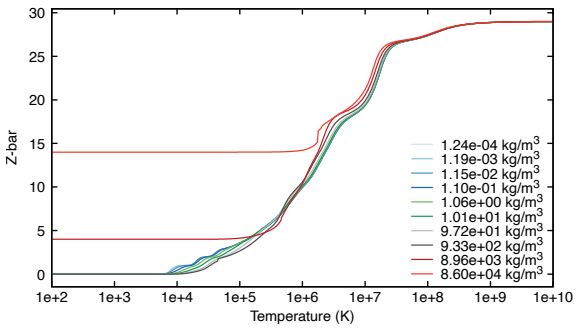

(G) Cu.

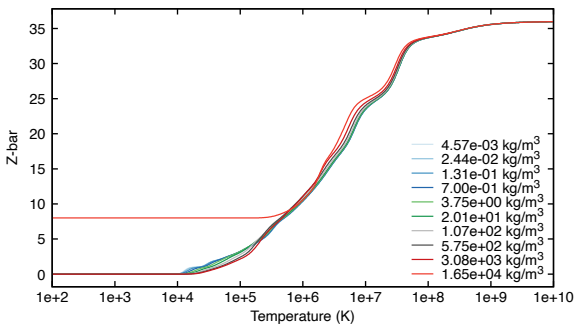

(H) Kr.

FIGURE 2.2. Comparison of equilibrium ionization fractions for various elements at different densities using models incorporating high-density effects (ionization potential depression and three-body recombination). We can see that the expected valence state is reproduced for Al and Be at solid densities.

Mattioli, et al. [63], Kotelnikov, et al., [45], and Landini, et al., [49, 50] are used, in that order. Note that in contrast to the coronal models in fig. 2.1, we consider only one set of ionization and recombination rate coefficients for each atomic species in this case. Suppression of dielectronic recombination rates due to high-density effects is not currently included in this model.

Including ionization potential depression and three-body recombination and applying a steady-state assumption results in a nonlinear system that must be solved to obtain the charge state fractions. This is done using a Newton iteration implemented in a simple script implemented in the python language. Computed average charge states for some species of interest using the aforementioned ionization and recombination models are shown in fig. 2.2. For each element, ten logarithmically-spaced density values are selected based on typical density values for solid and gas phases. Densities plotted using a light green color correspond roughly to a gas phase and densities plotted using a dark red color correspond roughly to a solid phase. For metals such as Be, Al, and Cu, solid densities are given at room temperature, and gas-phase densities are approximated based on the number densities of atmospheric gasses at STP. For atmospheric gases (ie., H, He, Ne, Ar, Kr) gas-phase densities are chosen at standard temperature and pressure (STP), and solid densities are approximated based on the number densities of metals at room temperature.

Implementation. One of the primary motivations for the use of ionization potential depression models is to properly capture the conductivity behavior of metals such as Be and Al in solid and liquid phases. In such regimes, the metal may be modeled roughly as a two-component system of ions and an electron fluid. In order to properly capture this behavior, the ionization energies of valence electrons must be depressed below zero by the IPD model used. For example, we can see that in fig. 2.2 the charge state for Al at solid density is three in the low-temperature limit, which matches the expected valence of solid Al.

One difficulty associated with the use of IPD models for solid-density metals is that the ionization rate formula of Lotz (17) is only defined for strictly positive ionization energies and diverges to positive infinity as the ionization energy approaches zero. If it is known a priori that the average charge state will not fall below three, then the lower charge states may be excluded from the computation entirely. However, because density values often vary significantly over the duration of a simulation, there are likely to be regions of low-density material where the expected average charge state would require these lower charge states. It is therefore necessary to produce some method for handling negative ionization energies without completely excluding the corresponding charge states from the calculation.

Our current attempts to handle potentially negative ionization energies leverage the fact that the ionization rate formula (17) diverges monotonically to positive infinity as the ionization energy approaches zero. By clipping the ionization energy to a minimum value that is positive and of small magnitude, the ionization rate may be made arbitrarily large but always defined. To ensure that the resulting rate coefficients yield continuous derivatives, a smooth exponential damping formula is applied. The damped ionization energy is then given by

$$\hat{\phi}^{\mathrm{ion},*}_{(\alpha,k)} \stackrel{\mathrm{def}}{=} \phi^{\mathrm{ion}}_{(\alpha,k)} F\left(\varepsilon_*, \delta_*, \hat{\phi}^{\mathrm{ion}}_{(\alpha,k)} / \phi^{\mathrm{ion}}_{(\alpha,k)}\right) \tag{40a}$$

where

$$F(\varepsilon_*, \delta_*, x) \stackrel{\mathrm{def}}{=} \begin{cases} \delta_* + (\varepsilon_* - \delta_*) \exp\left(-\dfrac{(x-\varepsilon_*)^2}{2\varepsilon_*^2} - \dfrac{x-\varepsilon_*}{\delta_*-\varepsilon_*}\right), & x \le \varepsilon_*, \\ x & x \ge \varepsilon_*. \end{cases} \tag{40b}$$

In order to properly reproduce the desired valence conduction behavior, the three-body recombination rate should ideally go to zero, but at the very least not grow as fast as the ionization rate. We use the latter approach since it is somewhat easier to enforce: to do so, we define two damped ionization energies

$$\hat{\phi}^{\mathrm{ion},*}_{(\alpha,k)} = \phi^{\mathrm{ion}}_{(\alpha,k)} F\left(\varepsilon_*, \delta_*, \hat{\phi}^{\mathrm{ion}}_{(\alpha,k)} / \phi^{\mathrm{ion}}_{(\alpha,k)}\right) \quad \text{and} \quad \hat{\phi}^{\mathrm{ion},\dagger}_{(\alpha,k)} = \phi^{\mathrm{ion}}_{(\alpha,k)} F\left(\varepsilon_\dagger, \delta_\dagger, \hat{\phi}^{\mathrm{ion}}_{(\alpha,k)} / \phi^{\mathrm{ion}}_{(\alpha,k)}\right) \tag{41}$$

to be used in the evaluation of the ionization and three-body recombination rates $I_{(\alpha,k)}$ and $R^{\mathrm{tbr}}_{(\alpha,k+1)}$, re-

spectively. The results in fig. 2.2 were generated using the following parameters:

$$\varepsilon_* = 10^{-2}, \qquad \delta_* = 10^{-12}, \tag{42a}$$

$$\varepsilon_\dagger = 10^{-2}, \qquad \delta_\dagger = 10^{-4}. \tag{42b}$$

We have found that these parameters work reasonably well for most cases, though these values are less effective for the case of Cu near solid densities. A more suitable approach for this case has not yet been identified.

2.2.6. Momentum transfer due to elastic collisions

The momentum transfer from species s to species t due to elastic, non-reacting collisions is specified by $\mathbf{R}_{s;t}$, defined as [61, 62]

$$\mathbf{R}_{s;t} = \alpha_{s;t}\rho_s\rho_t\left(\mathbf{u}_t - \mathbf{u}_s\right)\Phi_{s;t} = \alpha_{s;t}\Big[\rho_s(\rho\mathbf{u})_t - \rho_t(\rho\mathbf{u})_s\Big]\Phi_{s;t}, \tag{43}$$

where $\alpha_{s;t}$ is the friction coefficient, and $\Phi_{s;t}$ is a correction factor that depends on the drift speed $|\mathbf{u}_s - \mathbf{u}_t|$ and the reduced thermal speed

$$V_{\text{therm}} = \sqrt{\frac{2k_\text{B}\left(m_t T_s + m_s T_t\right)}{m_s m_t}}. \tag{44}$$

It is found that $\Phi_{s;t} = 1$ in the limit of vanishing drift speed, and this value is generally sufficient when the drift speed is much smaller than the thermal speed. Expressions for more general scenarios can be found in [81].

The friction coefficient is composed of different expressions depending on whether the interaction involves one or more neutral species [62]. For two interacting charged species, the friction coefficient is given by

$$\alpha_{s;t} \overset{\text{def}}{=} \frac{Z_s^2 Z_t^2 |q_e|^4 \ln\Lambda_{s;t}}{6\pi\sqrt{2\pi}\epsilon_0^2 m_s m_t m_{s;t}\left(k_\text{B}T_s/m_s + k_\text{B}T_t/m_t\right)^{3/2}}, \tag{45}$$

where

$$m_{s;t} \overset{\text{def}}{=} \frac{m_s m_t}{m_s + m_t} \tag{46}$$

is the reduced mass and

$$\ln\Lambda_{s;t} \overset{\text{def}}{=} \ln\left[\frac{12\pi\left(\epsilon_0 k_\text{B}\right)^{3/2}\left(T_s + T_t\right)}{|Z_s Z_t||q_e|^3}\left(\frac{T_s T_t}{Z_s^2 n_s T_t + Z_t^2 n_t T_s}\right)^{1/2}\right] \tag{47}$$

is Coulomb's logarithm. For interactions that involve one or more neutral species, the friction coefficient is given by

$$\alpha_{s;t} \overset{\text{def}}{=} \frac{1}{m_s + m_t}\frac{4}{3}\left[\frac{8}{\pi}\left(\frac{k_\text{B}T_s}{m_s} + \frac{k_\text{B}T_t}{m_t}\right)\right]^{1/2}\sigma_{s;t}, \tag{48}$$

where $\sigma_{s;t}$ is the collisional cross section.

Constant values for some collisional cross sections $\sigma_{s;t}$ between species up to He are included in [62]. These values are summarized in table 2.2. For heavier species, we compute constant cross section values using a simple hard-sphere approximation, where

$$\sigma_{s;t} = \pi\left(r_s + r_t\right)^2 \tag{49}$$

with r_s and r_t the radii of the neutral charge state of species s and t, respectively. Cross section values computed using atomic radii from [23] are summarized in table 2.3.

Species	Value (m^2)	Model
H^+-H	1.0E−18	Quant. mech. calc. [97]
H^+-He	1.0E−19	Quant. mech. calc. [97]
$H-e$	1.5E−19	Quant. mech. calc. [97]
$He-e$	5.0E−20	Quant. mech. calc. [97]
$H-He$	1.5E−19	[52]
$H-He^+$	2.0E−20	Hard sphere [62]
$H-He^{2+}$	1.0E−20	Hard sphere [62]
$He-He^+$	5.0E−19	Quant. mech. calc. [31]
$He-He^{2+}$	3.0E−21	Hard sphere [62]

TABLE 2.2. Elastic scattering cross section values for some interactions involving neutral species.

2.2.7. Momentum transfer due to charge exchange

The following approximation for $\Gamma^{\text{cx}}_{(\alpha,k)}$ is given in [72]:

$$\Gamma^{\text{cx}}_{(\alpha,k)} = \sigma^{\text{cx}}_{(\alpha,k)}\left(U^{\text{cx}}_{(\alpha,k)}\right) n_{(\alpha,k)} n_{(\alpha,0)} U^{\text{cx}}_{(\alpha,k)}, \tag{50}$$

where

$$U^{\text{cx}}_{(\alpha,k)} = \left(\frac{4}{\pi}u^2_{T_{(\alpha,k)}} + \frac{4}{\pi}u^2_{T_{(\alpha,0)}} + u^2_{(\alpha,k);(\alpha,0)}\right)^{1/2}, \tag{51}$$

with

$$u^2_{s;t} = \left\|\mathbf{u}_{s;t}\right\|^2, \qquad \mathbf{u}_{s;t} = \mathbf{u}_s - \mathbf{u}_t, \qquad u^2_{T_s} = \frac{2k_{\text{B}}T_s}{m_s}, \tag{52}$$

and σ^{cx}_s denotes the charge exchange cross section for species s. The author of [65] has observed this approximation to be accurate to within a few percent.

Using this approximation, the momentum sources $\boldsymbol{\mathcal{C}}^{\text{cx},[1]}_{(\alpha,k)}$ can be written more concretely in terms of conserved quantities. This gives

$$\boldsymbol{\mathcal{C}}^{\text{cx},[1]}_{(\alpha,k)} = \frac{1}{m_{(\alpha,0)}}\left[\rho_{(\alpha,k)}(\rho\mathbf{u})_{(\alpha,0)} - \rho_{(\alpha,0)}(\rho\mathbf{u})_{(\alpha,k)}\right]\sigma^{\text{cx}}_{(\alpha,k)}\left(U^{\text{cx}}_{(\alpha,k)}\right)U^{\text{cx}}_{(\alpha,k)} + \mathbf{R}^{\text{cx}}_{(\alpha,k);(\alpha,0)} - \mathbf{R}^{\text{cx}}_{(\alpha,0);(\alpha,k)}, \tag{53}$$

and, similarly for the total energy sources $\mathcal{C}^{\text{cx},[2]}_{(\alpha,k)}$,

$$\begin{aligned}\mathcal{C}^{\text{cx},[2]}_{(\alpha,k)} = \frac{1}{2m_{(\alpha,0)}}&\left[\frac{\rho_{(\alpha,k)}}{\rho_{(\alpha,0)}}(\rho\mathbf{u})^2_{(\alpha,0)} - \frac{\rho_{(\alpha,0)}}{\rho_{(\alpha,k)}}(\rho\mathbf{u})^2_{(\alpha,k)}\right] + \frac{(\rho\mathbf{u})_{(\alpha,0)}}{\rho_{(\alpha,0)}}\cdot\mathbf{R}^{\text{cx}}_{(\alpha,k);(\alpha,0)} - \frac{(\rho\mathbf{u})_{(\alpha,k)}}{\rho_{(\alpha,k)}}\cdot\mathbf{R}^{\text{cx}}_{(\alpha,0);(\alpha,k)} \\ &+ Q^{\text{cx}}_{(\alpha,k);(\alpha,0)} - Q^{\text{cx}}_{(\alpha,0);(\alpha,k)}.\end{aligned} \tag{54}$$

The momentum transfer between an ion species $i=(\alpha,k)$ and a neutral species $n=(\alpha,0)$ due to charge exchange interactions is specified by $\mathbf{R}^{\text{cx}}_{i;n}$ and $\mathbf{R}^{\text{cx}}_{n;i}$, which are defined as [72]

$$\mathbf{R}^{\text{cx}}_{i;n} = \sigma^{\text{cx}}_i\left(U^{\text{cx}}_i\right) n_n\rho_i\left(\mathbf{u}_n - \mathbf{u}_i\right) u^2_{T_n}\left[4\left(\frac{4}{\pi}u^2_{T_i} + u^2_{i;n}\right) + \frac{9\pi}{4}u^2_{T_n}\right]^{-1/2}, \tag{55a}$$

$$\mathbf{R}^{\text{cx}}_{n;i} = \sigma^{\text{cx}}_i\left(U^{\text{cx}}_i\right) n_n\rho_i\left(\mathbf{u}_i - \mathbf{u}_n\right) u^2_{T_i}\left[4\left(\frac{4}{\pi}u^2_{T_n} + u^2_{i;n}\right) + \frac{9\pi}{4}u^2_{T_i}\right]^{-1/2}, \tag{55b}$$

or, to emphasize conserved quantities,

$$\mathbf{R}^{\text{cx}}_{i;n} = \sigma^{\text{cx}}_i\left(U^{\text{cx}}_i\right)\left[\rho_i(\rho\mathbf{u})_n - \rho_n(\rho\mathbf{u})_i\right]\frac{u^2_{T_n}}{m_n}\left[4\left(\frac{4}{\pi}u^2_{T_i} + u^2_{i;n}\right) + \frac{9\pi}{4}u^2_{T_n}\right]^{-1/2}, \tag{55c}$$

$$\mathbf{R}^{\text{cx}}_{n;i} = \sigma^{\text{cx}}_i\left(U^{\text{cx}}_i\right)\left[\rho_n(\rho\mathbf{u})_i - \rho_i(\rho\mathbf{u})_n\right]\frac{u^2_{T_i}}{m_n}\left[4\left(\frac{4}{\pi}u^2_{T_n} + u^2_{i;n}\right) + \frac{9\pi}{4}u^2_{T_i}\right]^{-1/2}. \tag{55d}$$

		Elastic scattering cross section (m^2)						
	Radius (m)	H	He	Be	Ne	Al	Ar	e^-
H	5.30E−11	3.53E−20	2.22E−20	8.55E−20	2.60E−20	9.19E−20	4.83E−20	8.82E−21
He	3.10E−11	2.22E−20	1.21E−20	6.42E−20	1.50E−20	6.97E−20	3.27E−20	3.02E−21
Be	1.12E−10	8.55E−20	6.42E−20	1.58E−19	7.07E−20	1.66E−19	1.05E−19	3.94E−20
Ne	3.80E−11	2.60E−20	1.50E−20	7.07E−20	1.81E−20	7.65E−20	3.73E−20	4.54E−21
Al	1.18E−10	9.19E−20	6.97E−20	1.66E−19	7.65E−20	1.75E−19	1.12E−19	4.37E−20
Ar	7.10E−11	4.83E−20	3.27E−20	1.05E−19	3.73E−20	1.12E−19	6.33E−20	1.58E−20

TABLE 2.3. Atomic radii and elastic scattering cross section values computed using a hard-sphere approximation. Values for interactions involving electrons are computed using an electron radius of zero. Values of atomic radii sourced from [23].

A common approach to constructing approximate values for the charge exchange cross sections σ_i^{cx} is a fit of the form

$$\sigma_i^{\text{cx}}(v) = \left(A + C\log_b v\right)^2, \tag{56}$$

where A, C, and b are constants. In [72] a fit formula from [32] for charge exchange between H and H^+ is used that is characterized by

$$A = 2.1\text{E}{-7}, \qquad C = -9.2\text{E}{-9}, \qquad \text{and} \qquad b = e, \tag{57}$$

with units of cm^2. Based on data from [16], the author of [65] proposes the following fits:

$$\text{H}{-}\text{H}^+: \qquad A = 1.12\text{E}{-18}, \qquad C = -7.15\text{E}{-20}, \qquad b = e, \tag{58a}$$

$$\text{D}{-}\text{D}^+: \qquad A = 1.09\text{E}{-18}, \qquad C = -7.15\text{E}{-20}, \qquad b = e, \tag{58b}$$

with units of m^2.

2.2.8. Thermal energy transfer due to elastic collisions

The thermal energy transfer from species s to species t due to elastic, non-reacting collisions is specified by $Q_{s;t}$, defined as [62]

$$Q_{s;t} = \frac{\alpha_{s;t}\rho_s\rho_t}{m_s+m_t}\left[A_{s;t}k_{\text{B}}(T_t - T_s)\Psi_{s;t} + m_t(\mathbf{u}_t - \mathbf{u}_s)^2\Phi_{s;t}\right] \tag{59a}$$

$$= \frac{\alpha_{s;t}}{m_s+m_t}\rho_s\rho_t A_{s;t}k_{\text{B}}(T_t - T_s)\Psi_{s;t} + \frac{\alpha_{s;t}}{m_s+m_t}\frac{m_t}{\rho_s\rho_t}\left[\rho_s(\rho\mathbf{u})_t - \rho_t(\rho\mathbf{u})_s\right]^2\Phi_{s;t}, \tag{59b}$$

where $\alpha_{s;t}$ is the friction coefficient given by either (45) or (48), and $\Psi_{s;t}$ and $\Phi_{s;t}$ are correction factors that depend on the drift speed $|\mathbf{u}_s - \mathbf{u}_t|$ and the reduced thermal speed (44). The parameter $A_{s;t}$ takes the value 4 for electron-neutral interactions, and 3 for all other types of interactions. The correction factors $\Psi_{s;t}$ and $\Phi_{s;t}$ take the value 1 in the limit of vanishing drift speed, and this value is generally sufficient when the drift speed is much smaller than the thermal speed. Expressions for more general scenarios can be found in [81].

2.2.9. Thermal energy transfer due to charge exchange

The transfer of thermal energy between an ion species $i = (\alpha, k)$ and a neutral species $n = (\alpha, 0)$ due to charge exchange interactions is specified by $Q_{i;n}^{\text{cx}}$ and $Q_{n;i}^{\text{cx}}$. The following approximations from [72] are used:

$$Q_{i;n}^{\text{cx}} = \sigma_i^{\text{cx}}\left(U_i^{\text{cx}}\right)n_n\rho_i\frac{3}{4}u_{T_n}^2\left(\frac{4}{\pi}u_{T_i}^2 + u_{i;n}^2 + \frac{64}{9\pi}u_{T_n}^2\right)^{1/2}, \tag{60a}$$

$$Q_{n;i}^{\text{cx}} = \sigma_i^{\text{cx}}\left(U_i^{\text{cx}}\right)n_n\rho_i\frac{3}{4}u_{T_i}^2\left(\frac{4}{\pi}u_{T_n}^2 + u_{i;n}^2 + \frac{64}{9\pi}u_{T_i}^2\right)^{1/2}, \tag{60b}$$

or

$$Q^{\mathrm{cx}}_{i;n} = \sigma^{\mathrm{cx}}_i\left(U^{\mathrm{cx}}_i\right)\rho_n\rho_i\frac{3}{4}\frac{u^2_{T_n}}{m_n}\left(\frac{4}{\pi}u^2_{T_i}+u^2_{i;n}+\frac{64}{9\pi}u^2_{T_n}\right)^{1/2}, \tag{60c}$$

$$Q^{\mathrm{cx}}_{n;i} = \sigma^{\mathrm{cx}}_i\left(U^{\mathrm{cx}}_i\right)\rho_n\rho_i\frac{3}{4}\frac{u^2_{T_i}}{m_n}\left(\frac{4}{\pi}u^2_{T_n}+u^2_{i;n}+\frac{64}{9\pi}u^2_{T_i}\right)^{1/2}, \tag{60d}$$

to emphasize conserved quantities.

2.2.10. Radiative losses

As described earlier in section 2.1.1, it is assumed that the ionization energy associated with the charge state transition is always radiated during radiative and dielectronic recombination reactions. Additional sources, as a function of electron internal energy, are used to more carefully account for the remainder of the radiated energy, depending on the specific details of the reaction. In general, since this additional loss constitutes some fraction of the electron internal energy participating in the reaction, we may bound the additional loss above and below, by the cases where all or none of the electron internal energy is radiated away, respectively. If no portion of the electron internal energy is radiated away during recombination, then no additions need be made to the source terms as described previously. If all of the electron internal energy is radiated away during recombination, then the contribution

$$\frac{\rho_{(\alpha,k)}}{m_{(\alpha,k)}}\rho_e e_e R_{(\alpha,k)} \tag{61}$$

should be added to the loss term $Q^{\mathrm{rad}}_{(\alpha,k-1)}$, for each recombining ion (α,k). At this time, our implementation is limited to these two extremes (all or none of this energy emitted). We are currently investigating potential approaches for incorporating these effects, including approaches similar to [60] where the loss term is parameterized in terms of an effective loss factor.

3. FULLY-AVERAGED MULTIFLUID MODEL

We now consider a reduced multifluid model in which the fluid equations for the individual charge states of a given atomic species are combined into a single fluid for that species. The resulting model consists of one set of fluid equations for each atomic species plus a set of fluid equations for the electron species. In the remainder of this section, the subscript α will be used to denote quantities associated with this average atomic state for atomic species α.

3.1. Model description

The values for total mass, momentum, and energy densities for species α are given by summing across all charge states:

$$\rho_\alpha \stackrel{\mathrm{def}}{=} \sum_{k=0}^{z_\alpha}\rho_{(\alpha,k)}, \tag{62a}$$

$$\rho_\alpha \mathbf{u}_\alpha \stackrel{\mathrm{def}}{=} \sum_{k=0}^{z_\alpha}\rho_{(\alpha,k)}\mathbf{u}_{(\alpha,k)}, \tag{62b}$$

$$\mathcal{E}_\alpha \stackrel{\mathrm{def}}{=} \sum_{k=0}^{z_\alpha}\mathcal{E}_{(\alpha,k)}. \tag{62c}$$

The total number and charge densities are obtained similarly:

$$n_\alpha \stackrel{\mathrm{def}}{=} \sum_{k=0}^{z_\alpha} n_{(\alpha,k)}, \tag{62d}$$

$$q_\alpha n_\alpha \stackrel{\mathrm{def}}{=} \sum_{k=0}^{z_\alpha} q_{(\alpha,k)} n_{(\alpha,k)}. \tag{62e}$$

The average charge state $\overline{Z}_\alpha$ is defined through the relation

$$n_\alpha \overline{Z}_\alpha \stackrel{\text{def}}{=} \sum_{k=0}^{z_\alpha} k n_{(\alpha,k)}. \tag{62f}$$

The model developed here tracks only the conserved variables ρ_α, $(\rho\mathbf{u})_\alpha$, $\mathcal{E}_\alpha$ for the charge-state averaged fluid for each atomic species. As such, only center-of-mass averages for quantities such as velocity and specific internal energy are available. The natural assumption, and the one that we make here, is therefore that the velocities and specific internal energies of the individual charge states are exactly that of the averaged fluid: ie., $\mathbf{u}_{(\alpha,k)} = \mathbf{u}_\alpha$ and $e_{(\alpha,k)} = e_\alpha$ for each k.

The above assumptions may be combined with a method for computing the charge state fractions of the atomic species α to separate the conserved quantities for each charge state. More specifically, suppose that an algorithm is provided that takes as input the conserved variables for the electron fluid and the conserved variables for each averaged ion fluid, and outputs the charge state fractions

$$f_{(\alpha,k)} \stackrel{\text{def}}{=} \frac{n_{(\alpha,k)}}{n_\alpha} \tag{63}$$

for each k. It should be noted that the charge state fractions are assumed to satisfy basic properties such as

$$f_{(\alpha,k)} \in [0,1] \qquad \text{and} \qquad \sum_{k=0}^{z_\alpha} f_{(\alpha,k)} = 1. \tag{64}$$

Define the averaged mass m_α and mass fractions $f^m_{(\alpha,k)}$ by

$$m_\alpha \stackrel{\text{def}}{=} \sum_{k=0}^{z_\alpha} f_{(\alpha,k)} m_{(\alpha,k)} \qquad \text{and} \qquad f^m_{(\alpha,k)} \stackrel{\text{def}}{=} \frac{m_{(\alpha,k)} f_{(\alpha,k)}}{m_\alpha}, \tag{65}$$

respectively. Then the conserved variables for each charge state are recovered (under these approximations) by

$$\rho_{(\alpha,k)} \stackrel{\text{def}}{=} \rho_\alpha f^m_{(\alpha,k)}, \qquad (\rho\mathbf{u})_{(\alpha,k)} \stackrel{\text{def}}{=} (\rho\mathbf{u})_\alpha f^m_{(\alpha,k)} \qquad \text{and} \qquad \mathcal{E}_{(\alpha,k)} \stackrel{\text{def}}{=} \mathcal{E}_\alpha f^m_{(\alpha,k)}. \tag{66}$$

The final assumption made in this section is that the masses of the individual charge states are related by

$$m_{(\alpha,k)} = m_{(\alpha,k+1)} + m_e = m_{(\alpha,0)} - k m_e. \tag{67}$$

Continuity. Summing (5a) with $s = (\alpha, k)$ for $k = 0, \ldots, z_\alpha$ and applying the relations (62) yields the following continuity equation for the total atomic number density:

$$\partial_t \rho_\alpha + \nabla \cdot \left(\rho_\alpha \mathbf{u}_\alpha\right) = \mathcal{C}^{[0]}_\alpha + \mathcal{S}^{[0]}_\alpha, \tag{68}$$

where

$$\mathcal{C}^{[0]}_\alpha \stackrel{\text{def}}{=} \sum_{k=0}^{z_\alpha} \mathcal{C}^{[0]}_{(\alpha,k)} \qquad \text{and} \qquad \mathcal{S}^{[0]}_\alpha \stackrel{\text{def}}{=} \sum_{k=0}^{z_\alpha} \mathcal{S}^{[0]}_{(\alpha,k)}. \tag{69}$$

Summing the contributions due to ionization and recombination reactions and using the mass relation (67), the collision source reduces to

$$\mathcal{C}^{[0]}_\alpha = \rho_e \frac{\rho_\alpha}{m_\alpha} \left(R_\alpha + \frac{\rho_e}{m_e} R^{\text{tbr}}_\alpha \right) - \rho_e \frac{\rho_\alpha}{m_\alpha} I_\alpha, \tag{70}$$

where

$$R_\alpha \stackrel{\text{def}}{=} \sum_{k=1}^{z_\alpha} f_{(\alpha,k)} R_{(\alpha,k)}, \qquad R^{\text{tbr}}_\alpha \stackrel{\text{def}}{=} \sum_{k=1}^{z_\alpha} f_{(\alpha,k)} R^{\text{tbr}}_{(\alpha,k)}, \qquad \text{and} \qquad I_\alpha \stackrel{\text{def}}{=} \sum_{k=0}^{z_\alpha - 1} f_{(\alpha,k)} I_{(\alpha,k)}. \tag{71}$$

The electron collision source is similarly reduced to

$$\mathcal{C}^{[0]}_e = \sum_{\alpha \in N_A} \rho_e \frac{\rho_\alpha}{m_\alpha} I_\alpha - \sum_{\alpha \in N_A} \rho_e \frac{\rho_\alpha}{m_\alpha} \left(R_\alpha + \frac{\rho_e}{m_e} R^{\text{tbr}}_\alpha \right). \tag{72}$$

Momentum. Summing (5b) with $s=(\alpha,k)$ for $k=0,\ldots,z_\alpha$, applying the relations (62), and transforming the system into a reference frame moving with the mean atomic fluid velocity $\mathbf{u}_\alpha$ yields

$$\partial_t\left(\rho_\alpha\mathbf{u}_\alpha\right)+\nabla\cdot\left(\rho_\alpha\mathbf{u}_\alpha\otimes\mathbf{u}_\alpha+p_\alpha\underline{\mathbf{I}}+\underline{\boldsymbol{\Pi}}_\alpha\right)=q_\alpha n_\alpha\left(\mathbf{E}+\mathbf{u}_\alpha\times\mathbf{B}\right)+\boldsymbol{\mathcal{C}}_\alpha^{[1]}+\boldsymbol{\mathcal{S}}_\alpha^{[1]}, \tag{73}$$

where

$$\boldsymbol{\mathcal{C}}_\alpha^{[1]}\stackrel{\text{def}}{=}\sum_{k=0}^{z_\alpha}\boldsymbol{\mathcal{C}}_{(\alpha,k)}^{[1]},\qquad\text{and}\qquad\boldsymbol{\mathcal{S}}_\alpha^{[1]}\stackrel{\text{def}}{=}\sum_{k=0}^{z_\alpha}\boldsymbol{\mathcal{S}}_{(\alpha,k)}^{[1]}. \tag{74}$$

The averaged collision source is obtained by simply summing the contributions from each charge state. The symmetry of the charge exchange terms results in their cancellation and removal from the momentum source for the averaged model. The reduction of the remaining components yields

$$\boldsymbol{\mathcal{C}}_\alpha^{[1]}=(\rho\mathbf{u})_e\frac{\rho_\alpha}{m_\alpha}\left(R_\alpha+\frac{\rho_e}{m_e}R_\alpha^{\text{tbr}}\right)-\rho_e\frac{(\rho\mathbf{u})_\alpha}{m_\alpha}I_\alpha+\sum_{s\in\Lambda_{\text{FA}}\backsim\alpha}\mathbf{R}_{\alpha;s}, \tag{75}$$

where

$$\mathbf{R}_{\alpha;e}\stackrel{\text{def}}{=}\sum_{k=0}^{z_\alpha}\mathbf{R}_{(\alpha,k);e},\qquad\qquad\mathbf{R}_{\alpha;\beta}\stackrel{\text{def}}{=}\sum_{k=0}^{z_\alpha}\sum_{\ell=0}^{z_\beta}\mathbf{R}_{(\alpha,k);(\beta,\ell)}, \tag{76}$$

and (76) is written with the understanding that $\mathbf{R}_{(\alpha,k);(\alpha,k)}=\mathbf{0}$. Similarly, the collision source for the electron fluid becomes

$$\boldsymbol{\mathcal{C}}_e^{[1]}=\sum_{\alpha\in N_A}\rho_e\frac{(\rho\mathbf{u})_\alpha}{m_\alpha}I_\alpha-\sum_{\alpha\in N_A}(\rho\mathbf{u})_e\frac{\rho_\alpha}{m_\alpha}\left(R_\alpha+\frac{\rho_e}{m_e}R_\alpha^{\text{tbr}}\right)+\sum_{\alpha\in\Lambda_{\text{FA}}}\mathbf{R}_{e;\alpha}, \tag{77}$$

where

$$\mathbf{R}_{e;\alpha}\stackrel{\text{def}}{=}\sum_{k=0}^{z_\alpha}\mathbf{R}_{e;(\alpha,k)}. \tag{78}$$

Energy. Summing (5c) with $s=(\alpha,k)$ for $k=0,\ldots,z_\alpha$, applying the relations (62), transforming the system into a reference frame moving with the mean species velocity $\mathbf{u}_\alpha$, and neglecting the individual ion drift velocities as before yields

$$\partial_t\mathcal{E}_\alpha+\nabla\cdot\left[\left(\mathcal{E}_\alpha+p_\alpha\right)\mathbf{u}_\alpha+\mathbf{u}_\alpha\cdot\underline{\boldsymbol{\Pi}}_\alpha+\mathbf{h}_\alpha\right]=q_\alpha n_\alpha\mathbf{u}_\alpha\cdot\mathbf{E}+\mathcal{C}_\alpha^{[2]}+\mathcal{S}_\alpha^{[2]}, \tag{79}$$

where

$$\mathcal{C}_\alpha^{[2]}\stackrel{\text{def}}{=}\sum_{k=0}^{z_\alpha}\mathcal{C}_{(\alpha,k)}^{[2]}\qquad\text{and}\qquad\mathcal{S}_\alpha^{[2]}\stackrel{\text{def}}{=}\sum_{k=0}^{z_\alpha}\mathcal{S}_{(\alpha,k)}^{[2]}. \tag{80}$$

Summing the contributions from each charge state, and again noting that the terms due to charge exchange interactions cancel, the averaged total energy source reduces to

$$\mathcal{C}_\alpha^{[2]}=\mathcal{E}_e\frac{\rho_\alpha}{m_\alpha}\left(R_\alpha+\frac{\rho_e}{m_e}R_\alpha^{\text{tbr}}\right)-\rho_e\frac{\mathcal{E}_\alpha}{m_\alpha}I_\alpha+\frac{\rho_e^2}{m_e^2}\frac{\rho_\alpha}{m_\alpha}\Phi_\alpha^{\text{tbr}}+\sum_{s\in\Lambda_{\text{FA}}\backsim\alpha}\left(\mathbf{u}_\alpha\cdot\mathbf{R}_{\alpha;s}+Q_{\alpha;s}\right), \tag{81}$$

where

$$\Phi_\alpha^{\text{tbr}}\stackrel{\text{def}}{=}\sum_{k=1}^{z_\alpha}f_{(\alpha,k)}\phi_{(\alpha,k-1)}^{\text{ion}}R_{(\alpha,k)}^{\text{tbr}}, \tag{82}$$

$\mathbf{R}_{\alpha;e}$ and $\mathbf{R}_{\alpha;\beta}$ are given in (76), and $Q_{\alpha;e}$ and $Q_{\alpha;\beta}$ are defined in a similar manner; ie.,

$$Q_{\alpha;e}\stackrel{\text{def}}{=}\sum_{k=0}^{z_\alpha}Q_{(\alpha,k);e},\qquad\text{and}\qquad Q_{\alpha;\beta}\stackrel{\text{def}}{=}\sum_{k=0}^{z_\alpha}\sum_{\ell=0}^{z_\beta}Q_{(\alpha,k);(\beta,\ell)}. \tag{83}$$

The collision source for the electron species becomes

$$\mathcal{C}_e^{[2]}=\sum_{\alpha\in N_A}\rho_e\frac{\mathcal{E}_\alpha}{m_\alpha}I_\alpha-\sum_{\alpha\in N_A}\mathcal{E}_e\frac{\rho_\alpha}{m_\alpha}\left(R_\alpha+\frac{\rho_e}{m_e}R_\alpha^{\text{tbr}}\right)-\sum_{\alpha\in N_A}\frac{\rho_e}{m_e}\frac{\rho_\alpha}{m_\alpha}\Phi_\alpha^{\text{ion}}+\sum_{\alpha=1}^{N_A}\left(\mathbf{u}_e\cdot\mathbf{R}_{e;\alpha}+Q_{e;\alpha}\right)+Q_e^{\text{rad}}, \tag{84}$$

where

$$Q_{e;\alpha}\stackrel{\text{def}}{=}\sum_{k=0}^{z_\alpha}Q_{e;(\alpha,k)}\qquad\text{and}\qquad\Phi_\alpha^{\text{ion}}\stackrel{\text{def}}{=}\sum_{k=0}^{z_\alpha-1}f_{(\alpha,k)}\phi_{(\alpha,k)}^{\text{ion}}I_{(\alpha,k)}. \tag{85}$$

3.2. Collisional transfer models

3.2.1. Quasi-steady-state collisional ionization equilibrium (QSS-CIE)

Most of the models for collisional interactions described in section 2.2 depend on quantities associated with individual charge states, such as the number densities $n_{(\alpha,k)}$. However, the averaged multifluid model tracks only total mean quantities aggregated over all ionization states. Quantities associated with individual charge states can be computed from the aggregate quantities using (65) and (66) if the charge state fractions $f_{(\alpha,k)}$ are known.

The following quasi-steady-state collisional ionization equilibrium (QSS-CIE) model is used to compute the charge state fractions [21]. This is done by solving a steady-state reaction system for each point in the physical domain. In the QSS-CIE model, the ionization fractions of two successive charge states are related by

$$\frac{f_{(\alpha,k+1)}}{f_{(\alpha,k)}} = \frac{I_{(\alpha,k)}}{R_{(\alpha,k+1)}}, \qquad (k = 0, \ldots, z_\alpha - 1). \tag{86}$$

Combining the relations (86) with the additional constraint

$$\sum_{k=0}^{z_\alpha} f_{(\alpha,k)} = 1 \tag{87}$$

yields a linear system for the values of the ionization fractions, which can be written as

$$\begin{pmatrix} 1 & 1 & 1 & \cdots & 1 \\ -I_{(\alpha,0)} & R_{(\alpha,1)} & & & \\ & -I_{(\alpha,1)} & R_{(\alpha,2)} & & \\ & & \ddots & \ddots & \\ & & & -I_{(\alpha,z_\alpha-1)} & R_{(\alpha,z_\alpha)} \end{pmatrix} \begin{pmatrix} f_{(\alpha,0)} \\ f_{(\alpha,1)} \\ f_{(\alpha,2)} \\ \vdots \\ f_{(\alpha,z_\alpha)} \end{pmatrix} = \begin{pmatrix} 1 \\ 0 \\ 0 \\ \vdots \\ 0 \end{pmatrix}. \tag{88}$$

Once the system (88) is solved, the ionization fractions obtained can be used to compute required quantities such as the individual ion number densities $n_{(\alpha,k)}$ and the average ion charge state $\overline{Z}_\alpha$.

3.2.2. Momentum transfer due to elastic collisions

Using the general model (43) for momentum transfer, the reduced source terms defined in (76) can be simplified as

$$\mathbf{R}_{s;e} = \alpha_{s;e}\rho_s\rho_e(\mathbf{u}_e - \mathbf{u}_s), \tag{89a}$$

$$\mathbf{R}_{s;t} = \alpha_{s;t}\rho_s\rho_t(\mathbf{u}_t - \mathbf{u}_s), \tag{89b}$$

where $\alpha_{s;e}$ and $\alpha_{s;t}$ are the mass-weighted friction coefficients

$$\alpha_{s,e} \overset{\text{def}}{=} \sum_{k=0}^{z_s} \alpha_{(s,k);e} f^m_{(s,k)}, \tag{90a}$$

$$\alpha_{s,t} = \sum_{k=0}^{z_s}\sum_{\ell=0}^{z_t} \alpha_{(s,k);(t,\ell)} f^m_{(s,k)} f^m_{(t,\ell)}. \tag{90b}$$

3.2.3. Thermal energy transfer due to elastic collisions

Using the general model (59) for thermal energy transfer, the reduced source terms defined in (83) can be simplified slightly as

$$Q_{s;e} = \tilde{\alpha}_{s;e}\rho_s\rho_e k_\mathrm{B}(T_e - T_s)\Psi_{s;e} + \hat{\alpha}_{s;e}\rho_s\rho_e(\mathbf{u}_e - \mathbf{u}_s)^2\Phi_{s;e}, \tag{91a}$$

$$Q_{s;t} = \tilde{\alpha}_{s;t}\rho_s\rho_t k_\mathrm{B}(T_t - T_s)\Psi_{s;t} + \hat{\alpha}_{s;t}\rho_s\rho_t(\mathbf{u}_t - \mathbf{u}_s)^2\Phi_{s;t}, \tag{91b}$$

where

$$\tilde{\alpha}_{s;e} = \sum_{k=0}^{z_s} \frac{\alpha_{(s,k);e} f^m_{(s,k)} A_{(s,k);e}}{m_{(s,k)} + m_e}, \qquad \hat{\alpha}_{s;e} = \sum_{k=0}^{z_s} \frac{\alpha_{(s,k);e} f^m_{(s,k)} m_e}{m_{(s,k)} + m_e}, \tag{92a}$$

$$\tilde{\alpha}_{s;t} = 3 \sum_{k=0}^{z_s} \sum_{\ell=0}^{z_t} \frac{\alpha_{(s,k);(t,\ell)} f^m_{(s,k)} f^m_{(t,\ell)}}{m_{(s,k)} + m_{(t,\ell)}}, \qquad \hat{\alpha}_{s;t} = \sum_{k=0}^{z_s} \sum_{\ell=0}^{z_t} \frac{\alpha_{(s,k);(t,\ell)} f^m_{(s,k)} f^m_{(t,\ell)} m_{(t,\ell)}}{m_{(s,k)} + m_{(t,\ell)}}. \tag{92b}$$

4. SINGLE-FLUID EXTENDED MAGNETOHYDRODYNAMICS MODEL

We now consider the derivation of a generalized Ohm's law for a single-fluid magnetohydrodynamics (MHD) model as a reduction of the multifluid models. In general, the derivation of the single-fluid MHD model assumes quasineutrality between the electrons and ions, and the separate fluid equations for ions and electrons are summed to produce a set of fluid equations describing conservation of total fluid mass, momentum, and energy. The resulting fluid equations are combined with a description of electromagnetics and an Ohm's law that describes the evolution of current density.

The focus of this section is the derivation of the full generalized Ohm's law, that may be reduced term-by-term, ultimately to the level of a traditional resistive or ideal MHD Ohm's law. The primary motivation is to show the relationship between the material parameters used for typical single-fluid MHD models (ie., resistivity) and the material parameters used in the multifluid context (ie., ionization, recombination, and elastic scattering rates). Discussion of the remainder of the consistent single-fluid MHD model (ie., the fluid equations themselves) is omitted. This presentation is based on the fully-averaged multifluid model described in section 3, since that model already includes some of the reductions required to form the single-fluid model. We restrict our discussion here to the case of a single atomic species α in order to reduce the complexity of the model, but this can be extended to multiple atomic species.

4.1. Center-of-mass quantities

The total mass, momentum, and energy densities for the plasma are given by summing the contributions from electrons and ions:

$$\rho \stackrel{\text{def}}{=} \rho_\alpha + \rho_e, \tag{93a}$$

$$\rho \mathbf{u} \stackrel{\text{def}}{=} \rho_\alpha \mathbf{u}_\alpha + \rho_e \mathbf{u}_e, \tag{93b}$$

$$\mathcal{E} \stackrel{\text{def}}{=} \mathcal{E}_\alpha + \mathcal{E}_e. \tag{93c}$$

Note that the definitions for the total mass and momentum densities given above implicitly define the center-of-mass velocity $\mathbf{u}$.

4.2. Generalized Ohm's law

In this context, it is useful to write the charge of each species in terms of a positive unit charge quantity $\mathrm{e} = |q_e|$, where $q_e = -\mathrm{e}$. The ion particle charge in this notation is given by $q_\alpha = \overline{Z}_\alpha \mathrm{e}$. The derivation of Ohm's law proceeds by computing a charge-weighted sum of the momentum equations of each species [19], and assuming quasineutrality: ie., $n_e = \overline{Z}_\alpha n_\alpha$. Multiplying the ion and electron momentum equations by $\overline{Z}_\alpha \mathrm{e}/m_\alpha$ and $-\mathrm{e}/m_e$, respectively, and summing yields, after some algebraic manipulation,

$$
\begin{aligned}
&\partial_t \mathbf{J} - (m_\alpha n_\alpha \mathbf{u}_\alpha)\,\partial_t\left(\frac{\overline{Z}_\alpha \mathrm{e}}{m_\alpha}\right) - \left(\nabla\frac{\overline{Z}_\alpha \mathrm{e}}{m_\alpha}\right)\left(m_\alpha n_\alpha \mathbf{u}_\alpha \otimes \mathbf{u}_\alpha + p_\alpha \underline{\mathbf{I}} + \underline{\boldsymbol{\Pi}}_\alpha\right) \\
&\quad + \nabla\cdot\left[\left(1+\frac{m_e\overline{Z}_\alpha}{m_\alpha}\right)(\mathbf{u}\otimes\mathbf{J}+\mathbf{J}\otimes\mathbf{u}) - \frac{m_e\overline{Z}_\alpha}{m_\alpha}(\mathbf{u}_e\otimes\mathbf{J}+\mathbf{J}\otimes\mathbf{u}_e) - \frac{1}{\overline{Z}_\alpha \mathrm{e} n_\alpha}(\mathbf{J}\otimes\mathbf{J})\right. \\
&\qquad \left. - \frac{\mathrm{e}}{m_e}\left(\left(p_e\underline{\mathbf{I}}+\underline{\boldsymbol{\Pi}}_e\right) - \frac{m_e\overline{Z}_\alpha}{m_\alpha}\left(p_\alpha\underline{\mathbf{I}}+\underline{\boldsymbol{\Pi}}_\alpha\right)\right)\right] \\
&= \frac{\overline{Z}_\alpha \mathrm{e}^2 n_\alpha}{m_e}\left[\left(1+\frac{m_e\overline{Z}_\alpha}{m_\alpha}\right)\left(\mathbf{E}+\mathbf{u}\times\mathbf{B}-\eta\mathbf{J}+\eta^{\mathrm{ion}}\overline{Z}_\alpha \mathrm{e} n_\alpha \mathbf{u}\right) - \eta^{\mathrm{rec}}\mathbf{J}\right] - \frac{\mathrm{e}}{m_e}\left(1-\frac{m_e\overline{Z}_\alpha}{m_\alpha}\right)\mathbf{J}\times\mathbf{B}.
\end{aligned}
\tag{94}
$$

Here the values

$$
\eta = \frac{m_e m_\alpha}{\overline{Z}_\alpha \mathrm{e}^2}\alpha_{e;\alpha} \tag{95a}
$$

$$
\eta^{\mathrm{ion}} = \frac{m_e}{\overline{Z}_\alpha \mathrm{e}^2}\left(R_\alpha + \overline{Z}_\alpha n_\alpha R_\alpha^{\mathrm{tbr}} - I_\alpha\right) \tag{95b}
$$

$$
\eta^{\mathrm{rec}} = \frac{m_e}{\overline{Z}_\alpha \mathrm{e}^2}\left(R_\alpha + \overline{Z}_\alpha n_\alpha R_\alpha^{\mathrm{tbr}} + \frac{m_e\overline{Z}_\alpha}{m_\alpha} I_\alpha\right). \tag{95c}
$$

denote terms that induce resistive effects.

It should be noted that the only assumption made in the derivation of (94) is quasineutrality of the plasma. Additional assumptions are typically used to further simplify (94) as part of generating the desired Ohm's law for a given application. Two assumptions are often used for this purpose. The first is to neglect the contributions of ionization and recombination, which is particularly suited to the case of fully ionized plasmas with a constant $\overline{Z}$. In this case, η as defined in (95a) denotes the traditional resistivity.

The second assumption is that the electron particle mass is orders of magnitude smaller than the particle mass of the ions. The result of this assumption is to neglect terms of order

$$
\frac{m_e\overline{Z}_\alpha}{m_\alpha}. \tag{96}
$$

The justification for this is that the ratio (96) is on the order of $5\mathrm{E}{-4}$ for monatomic proteum and decreases as the atomic mass number of the ions increases. Under these additional assumptions, (94) simplifies to

$$
\partial_t \mathbf{J} + \nabla\cdot\left[\mathbf{u}\otimes\mathbf{J}+\mathbf{J}\otimes\mathbf{u} - \frac{1}{\overline{Z}_\alpha \mathrm{e} n_\alpha}\mathbf{J}\otimes\mathbf{J} - \frac{\mathrm{e}}{m_e}\left(p_e\underline{\mathbf{I}}+\underline{\boldsymbol{\Pi}}_e\right)\right] = \frac{\overline{Z}_\alpha \mathrm{e}^2 n_\alpha}{m_e}\left(\mathbf{E}+\mathbf{u}\times\mathbf{B}-\eta\mathbf{J}\right) - \frac{\mathrm{e}}{m_e}\mathbf{J}\times\mathbf{B}, \tag{97}
$$

which is the familiar generalized Ohm's law used in most contexts.

5. DISCRETIZATION OF THE MULTIFLUID SYSTEM

In this section we discuss some crucial aspects of the discretization of the fluid equations in the multifluid system. This is done using the general expressions (5) for the fluid equations for an arbitrary species s, where the index set to which s belongs varies depending on the exact form of the multifluid model (for example the general multifluid model described in section 2 or the fully averaged model described in section 3). The details of the finite element discretization and associated stabilization scheme follow that of [27], which extends the work of [58, 59] to a two-fluid system, and is included here mostly for the sake of completeness. In the context of the multifluid model development that is the focus of this manuscript, the primary concern is synchronization of the artificial diffusion across all species in the multifluid system.

5.1. Continuous Galerkin finite element discretization

The fluid equations (5) may be written in the form of a general balance law:

$$\partial_t \mathbf{U}_s + \nabla \cdot \underline{\mathbf{F}}(\mathbf{U}_s) = \mathbf{S}_s(\mathbf{U}_s), \tag{98}$$

where

$$\mathbf{U}_s = \begin{bmatrix} \rho_s \\ \rho_s \mathbf{u}_s \\ \mathcal{E}_s \end{bmatrix}, \tag{99a}$$

$$\underline{\mathbf{F}}(\mathbf{U}_s) = \begin{bmatrix} \rho_s \mathbf{u}_s \\ \rho_s \mathbf{u}_s \otimes \mathbf{u}_s + p_s \underline{\mathbf{I}} + \underline{\boldsymbol{\Pi}}_s \\ (\mathcal{E}_s + p_s)\mathbf{u}_s + \mathbf{u}_s \cdot \underline{\boldsymbol{\Pi}}_s + \mathbf{h}_s \end{bmatrix}, \tag{99b}$$

$$\mathbf{S}_s(\mathbf{U}_s) = \begin{bmatrix} \mathcal{C}_s^{[0]} + \mathcal{S}_s^{[0]} \\ q_s n_s (\mathbf{E} + \mathbf{u}_s \times \mathbf{B}) + \boldsymbol{\mathcal{C}}_s^{[1]} + \boldsymbol{\mathcal{S}}_s^{[1]} \\ q_s n_s \mathbf{u}_s \cdot \mathbf{E} + \mathcal{C}_s^{[2]} + \mathcal{S}_s^{[2]} \end{bmatrix}. \tag{99c}$$

Given a convex domain $\Omega \subset \mathbb{R}^3$ with boundary $\partial\Omega$, let $\mathcal{T}_h$ be a collection of elements K that partition the domain Ω such that $\Omega = \cup_{e=1}^{N_e} K_e$, where N_e and N_h are the number of elements and nodes in the mesh, respectively. Let V^h denote the finite element space of continuous piecewise-linear functions such that each $u^h \in V^h$ satisfies $u^h|_K \in P^1(K)$ for each $K \in \mathcal{T}_h$. Let $\mathbf{U}_s^h$ denote the finite element approximation of the solution $\mathbf{U}_s$. The finite element discretization is based on the weak form

$$\int_\Omega v \partial_t \mathbf{U}_s \, d\Omega - \int_\Omega \underline{\mathbf{F}}(\mathbf{U}_s) \cdot \nabla v \, d\Omega + \int_{\partial\Omega} v \underline{\mathbf{F}}(\mathbf{U}_s) \cdot \mathbf{n} \, ds - \int_\Omega v \mathbf{S}_s(\mathbf{U}_s) \, d\Omega = \mathbf{0}. \tag{100}$$

Let $\{v_k\}_{k=1}^{N_h}$ denote the standard nodal basis for V^h, so that $\mathbf{U}_s^h = \sum_k \mathbf{U}_{s,k} v_k$ where $\mathbf{U}_{s,k}$ is the vector of nodal solution values at node k. Let $\boldsymbol{\mathcal{U}}_s^h = [\mathbf{U}_{s,1}, \ldots, \mathbf{U}_{s,N_h}]^T$ denote the vector of all nodal unknowns. Then the semidiscrete scheme can be written in matrix form as

$$\underline{\boldsymbol{\mathcal{M}}}_{\mathrm{C}} \partial_t \boldsymbol{\mathcal{U}}_s^h + \boldsymbol{\mathcal{K}}_s(\boldsymbol{\mathcal{U}}_s^h) + \boldsymbol{\mathcal{B}}_s(\boldsymbol{\mathcal{U}}_s^h) + \boldsymbol{\mathcal{S}}_s(\boldsymbol{\mathcal{U}}_s^h) = \mathbf{0}, \tag{101}$$

where

$$\underline{\boldsymbol{\mathcal{M}}}_{\mathrm{C}} = \left\{ \underline{\mathbf{M}}_{k,\ell} \right\}_{k,\ell=1}^{N_h}, \qquad \underline{\mathbf{M}}_{k,\ell} = m_{k,\ell} \underline{\mathbf{I}}_{m \times m}, \qquad m_{k,\ell} = \int_\Omega v_k v_\ell \, d\Omega \tag{102a}$$

$$\boldsymbol{\mathcal{K}}_s(\boldsymbol{\mathcal{U}}_s^h) = \left\{ (\mathbf{K}_s)_k \right\}_{k=1}^{N_h}, \qquad (\mathbf{K}_s)_k = -\int_\Omega \underline{\mathbf{F}}(\mathbf{U}_s^h) \cdot \nabla v_k \, d\Omega \tag{102b}$$

$$\boldsymbol{\mathcal{B}}_s(\boldsymbol{\mathcal{U}}_s^h) = \left\{ (\mathbf{B}_s)_k \right\}_{k=1}^{N_h} \qquad (\mathbf{B}_s)_k = \int_{\partial\Omega} v_k \underline{\mathbf{F}}(\mathbf{U}_s^h) \cdot \mathbf{n} \, ds \tag{102c}$$

$$\boldsymbol{\mathcal{S}}_s(\boldsymbol{\mathcal{U}}_s^h) = \left\{ (\mathbf{S}_s)_k \right\}_{k=1}^{N_h} \qquad (\mathbf{S}_s)_k = -\int_\Omega v_k \mathbf{S}_s(\mathbf{U}_s^h) \, d\Omega \tag{102d}$$

and m is the number of conserved variables in $\mathbf{U}_s$.

The semidiscrete formulation (101) may produce solutions with spurious oscillations, particularly when steep gradients or discontinuities are present. Stabilization must therefore be applied in order to produce solutions without these features. Here we use an algebraic flux correction scheme that introduces artificial dissipation into the system to smooth out these oscillatory characteristics.

5.2. AFC stabilization

The AFC stabilization scheme for each fluid system uses the algebraic flux correction (AFC) method of [47, 48, 58, 59] with the iterative limiting strategy used in [58, 59]. This scheme requires three modifications to the semidiscrete formulation (101):

(i) Lumping the mass matrix applied to the time derivative term,

(ii) Adding a low-order artificial dissipation operator applied to each of the conserved variables, and

(iii) Adding an anti-diffusive correction to remove the lower-order artificial dissipation in regions where the solution is sufficiently smooth.

With these modifications, (101) becomes

$$\underline{\boldsymbol{\mathcal{M}}}_{\mathrm{L}}\partial_t \boldsymbol{\mathcal{U}}_s^h + \boldsymbol{\mathcal{K}}_s(\boldsymbol{\mathcal{U}}_s^h) + \boldsymbol{\mathcal{B}}_s(\boldsymbol{\mathcal{U}}_s^h) + \boldsymbol{\mathcal{S}}_s(\boldsymbol{\mathcal{U}}_s^h) + \underline{\boldsymbol{\mathcal{D}}}_s \cdot \boldsymbol{\mathcal{U}}_s^h - \boldsymbol{\mathcal{A}}_\alpha(\boldsymbol{\mathcal{U}}_s^h) = \mathbf{0}. \tag{103}$$

The global lumped mass matrix is given by summing over all elements $\underline{\boldsymbol{\mathcal{M}}}_{\mathrm{L}} = \sum_e \underline{\boldsymbol{\mathcal{M}}}_{\mathrm{L}}^{(e)}$, where

$$\underline{\boldsymbol{\mathcal{M}}}_{\mathrm{L}}^{(e)} = \left\{\underline{\mathbf{M}}_k^{(e)}\right\}_{k=1}^{N_h}, \qquad \underline{\mathbf{M}}_k^{(e)} = m_k^{(e)}\underline{\mathbf{I}}_{m\times m}, \qquad m_k^{(e)} = \sum_\ell m_{k,\ell}^{(e)}, \qquad m_{k,\ell}^{(e)} = \int_{K_e} \nu_k \nu_\ell \, d\Omega. \tag{104}$$

The diffusion operators are composed of element-wise contributions $\underline{\boldsymbol{\mathcal{D}}}_s = \sum_e \underline{\boldsymbol{\mathcal{D}}}_s^{(e)}$ where each component is constructed using Rusanov diffusion:

$$\underline{\boldsymbol{\mathcal{D}}}_s^{(e)} = \left\{\left[\underline{\mathbf{D}}_s^{(e)}\right]_{k,\ell}\right\}_{k,\ell=1}^{N_h}, \qquad \left[\underline{\mathbf{D}}_s^{(e)}\right]_{k,\ell} = [d_s^{(e)}]_{k,\ell}\underline{\mathbf{I}}_{N_s\times N_s} \tag{105}$$

and N_s is the number of equations in the Euler subsystem (five for three-dimensional problems). The form of $[d_s^{(e)}]_{k,\ell}$ depends on the approach taken. Initial development utilized discrete diffusion operators computed separately for each species. In this case the values of $[d_s^{(e)}]_{k,\ell}$ for species s are given by

$$[d_s^{(e)}]_{k,\ell} = \max\left\{\|\mathbf{c}_{k,\ell}^{(e)}\|\lambda_{\max}\left(\mathbf{n}_{k,\ell}^{(e)}\cdot\mathfrak{J}_s(\mathbf{U}_{s,\ell})\right), \quad \|\mathbf{c}_{\ell,k}^{(e)}\|\lambda_{\max}\left(\mathbf{n}_{\ell,k}^{(e)}\cdot\mathfrak{J}_s(\mathbf{U}_{s,k})\right)\right\}, \qquad k\neq\ell, \tag{106a}$$

$$[d_s^{(e)}]_{k,k} = -\sum_{k\neq\ell}[d_s^{(e)}]_{k,\ell}, \tag{106b}$$

where

$$\mathfrak{J}_s = \frac{\partial \underline{\mathbf{F}}_s}{\partial \mathbf{U}_s} \tag{107}$$

is the physical flux Jacobian, $\lambda_{\max}(\cdot)$ denotes the maximum eigenvalue magnitude, and $\mathbf{c}_{k,\ell}^{(e)}$ is the element convection operator given by

$$\mathbf{c}_{k,\ell}^{(e)} = \int_{K_e} \nu_\ell \nabla\nu_k \, d\Omega, \qquad \mathbf{n}_{k,\ell}^{(e)} = \frac{\mathbf{c}_{k,\ell}^{(e)}}{\|\mathbf{c}_{k,\ell}^{(e)}\|}. \tag{108}$$

The eigenvalues of the flux Jacobian may be bounded by [78]

$$\lambda_{\max}\left(\mathbf{n}_{k,\ell}^{(e)}\cdot\mathfrak{J}_s\left(\mathbf{U}_{s,\ell}\right)\right) \leq \|\mathbf{n}_{k,\ell}^{(e)}\cdot\mathbf{u}_{s,\ell}\| + (c_s)_{s,\ell}, \tag{109}$$

where $\mathbf{u}_{s,\ell}$ and $(c_s)_{s,\ell}$ denote the fluid velocity and sound speed for species s, respectively, at the node ℓ.

Unfortunately, the above strategy for generating the diffusion operators was found to produce unsatisfactory results, even when only the low-order method was considered. The issue is that the diffusion operators are computed separately for each species. When physical particle masses are used, the electron sound speed will tend to be more than an order of magnitude larger than that of the atomic species, resulting in significantly more diffusion being added to the electron species. This can cause the electrons to diffuse past the ions, even if no fluid convective motion is present, artificially producing charge separation between the species, and ultimately resulting in non-physical behavior and the development of severe instabilities.

As an alternative, the same diffusion operator is used for all species. This is done by setting $[d_s^{(e)}]_{k,\ell} = d_{k,\ell}^{(e)}$ for all species s, where

$$d_{k,\ell}^{(e)} = \max\left\{\|\mathbf{c}_{k,\ell}^{(e)}\|\max_s\lambda_{\max}\left(\mathbf{n}_{k,\ell}^{(e)}\cdot\mathfrak{J}_s(\mathbf{U}_{s,\ell})\right), \quad \|\mathbf{c}_{\ell,k}^{(e)}\|\max_s\lambda_{\max}\left(\mathbf{n}_{\ell,k}^{(e)}\cdot\mathfrak{J}_s(\mathbf{U}_{s,k})\right)\right\} \tag{110}$$

for $k \neq \ell$. This constructs a diffusion operator based on the maximum characteristic speed across all fluid species. While this strategy is ultimately more diffusive, it has been found to be significantly more robust.

The anti-diffusive term $\mathcal{A}_\alpha(\mathcal{U}_s^h)$ is constructed in terms of element-wise contributions:

$$\mathcal{A}_\alpha(\mathcal{U}_s^h) = \sum_e \alpha^{(e)} \mathcal{A}^{(e)}(\mathcal{U}_s^h) \tag{111}$$

where

$$\mathcal{A}^{(e)}(\mathcal{U}_s^h) = \left(\underline{\mathcal{M}}_{\mathrm{L}}^{(e)} - \underline{\mathcal{M}}_{\mathrm{C}}^{(e)}\right) \partial_t \mathcal{U}_s^h + \underline{\mathcal{D}}^{(e)} \cdot \mathcal{U}_s^h \tag{112}$$

and $\alpha^{(e)}$ is the element limiter. One may alternatively neglect the mass matrix terms in (112), which results in a scheme where the mass matrix is always fully lumped.

The element limiter is designed to detect when the solution is smooth and the anti-diffusive term should be used to remove the artificial dissipation from the system. It should be noted that we assume that the limiter $\alpha^{(e)}$ is computed synchronously across all fluid species in the system as follows (hence the lack of species index s). Let $u : \Omega \to \mathbb{R}$ be a scalar function with a finite element approximation $u^h = \sum_k u_k^h v_k$, and let $\bar{u}^{(e)}$ be the average of u^h on the mesh cell K_e; that is,

$$\bar{u}^{(e)} = \frac{1}{|K_e|} \int_{K_e} u^h \, d\Omega, \qquad\qquad |K_e| = \int_{K_e} d\Omega. \tag{113}$$

The nodal limiter $\Phi_k : \mathbb{R} \to [0,1]$ is defined by [59]

$$\Phi_k(u^h) = 1 - \left[\frac{\left| \sum_e \int_{K_e} v_k \left(u^h - \bar{u}^{(e)}\right) d\Omega \right|}{\sum_e \left| \int_{K_e} v_k \left(u^h - \bar{u}^{(e)}\right) d\Omega \right| + \varepsilon h} \right]^q, \tag{114}$$

where ε is a small number that is used to prevent division by zero without distinguishing between the cases of vanishing and nonvanishing denominators. The parameter $q \geq 1$ acts as a steepener: increasing this value reduces the amount of numerical dissipation that is included when away from local extrema. In cases where all limited quantities u^h have magnitudes on the order of 1, a constant value for ε in the vicinity of the machine epsilon generally works well (eg., $\varepsilon = 10^{-14}$). However, problems defined in physical units often produce quantities that have magnitudes significantly smaller or larger than 1: For example, the electron mass density ρ_e given in units of $\mathrm{kg/m^3}$ is typically much less than 1. In these cases, we use a scaled value $\varepsilon = \varepsilon_0 \bar{u}^h$ where ε_0 is on the order of machine epsilon (eg., $\varepsilon_0 = 10^{-14}$) and

$$\bar{u}^h = \frac{1}{|\Omega|} \int_\Omega u^h \, d\Omega \tag{115}$$

is the average value of u^h across the problem domain Ω.

Given a set of quantities u^h for which the nodal limiters are calculated, the element limiters $\alpha^{(e)}$ are computed from the nodal limiters as

$$\alpha^{(e)} = \min_u \min_{k \in N_h(K_e)} \Phi_k(u^h), \tag{116}$$

where $N_h(K_e) = \{k : \mathbf{x}_k \in \overline{K_e}\}$ is the set of nodes adjacent to the element K_e. For the leftmost minimum in (116), u ranges over a set of limited quantities which may depend on the problem. For example, to compute limiters based on the mass density and pressure of every species s in the system, u ranges over the union

$$\bigcup_s \{\rho_s, p_s\}. \tag{117}$$

The limiter (114) differs from the one used previously in [59] only in that the εh term is not included in the numerator, which changes the behavior of the limiter when the quantity u^h is constant. Using (114) for constant u^h yields $\Phi_k(u^h) = 1$, resulting in the high-order method being used. If the εh term is included in the numerator, then for constant u^h the limiter yields the value zero, and the low-order method is used. If all of the conserved quantities are also constant, then both cases yield the same behavior. However, suppose that a system contains two species i and e, and that ρ_i is constant, ρ_e is not, and $\alpha^{(e)}$ is computed as a function of $u \in \{\rho_i, \rho_e\}$. Then the limiter used in [59] would cause the low-order scheme to be used regardless of the behavior of ρ_e, whereas the limiter (114) would only cause the low-order scheme to be used if it was required to stabilize ρ_e. This therefore prevents the low-order scheme from being used in cases where it is not needed and would adversely affect the solution.

6. ELECTROMAGNETICS

We consider several cases: an electrostatic model, a parabolic divergence cleaning method and an implicit projection method for the traditional curl formulation of Maxwell's equations, a purely-hyperbolic potential-based formulation of Maxwell's equations, and a mixed hyperbolic-elliptic potential-based formulation of Maxwell's equations.

6.1. Electrostatic model

We consider a standard electrostatic model in which the electric field $\mathbf{E}$ is described by a scalar potential ϕ satisfying

$$\epsilon_0 \nabla^2 \phi + q = 0, \tag{118}$$

with $\mathbf{E} = -\nabla\phi$. By construction, the electrostatic model satisfies the electric field divergence constraint (Gauss's Law) (121a) to numerical precision.

6.1.1. Finite element discretization

Given a convex domain $\Omega \subset \mathbb{R}^3$ with boundary $\partial\Omega$, the finite element discretization of (118) is based on the weak form

$$-\epsilon_0 \int_\Omega \nabla\phi \cdot \nabla v \, d\Omega + \int_\Omega q v \, d\Omega = 0. \tag{119}$$

In general, we do not include the boundary flux term in the weak form, thereby weakly enforcing the condition $\mathbf{E} \cdot \mathbf{n} = 0$ along the boundary of the domain.

6.2. Curl form of Maxwell's equations

In first-order form, Maxwell's equations may be written as

$$\partial_t \mathbf{E} - c^2 \nabla \times \mathbf{B} + \frac{1}{\epsilon_0}\mathbf{J} = \mathbf{0}, \tag{120a}$$

$$\partial_t \mathbf{B} + \nabla \times \mathbf{E} = \mathbf{0}, \tag{120b}$$

where the electric field $\mathbf{E}$ and magnetic field $\mathbf{B}$ are required to satisfy their respective Gauss's Laws:

$$\nabla \cdot \mathbf{E} = \frac{q}{\epsilon_0}, \tag{121a}$$

$$\nabla \cdot \mathbf{B} = 0. \tag{121b}$$

6.2.1. Finite element discretization

Given a convex domain $\Omega \subset \mathbb{R}^3$ with boundary $\partial\Omega$, the finite element discretization of (120) over Ω is based on the weak form

$$\int_\Omega v \partial_t \mathbf{E} \, d\Omega - c^2 \int_\Omega \mathbf{B} \times \nabla v \, d\Omega + \int_{\partial\Omega} v \underline{\mathbf{F}}_{\mathbf{E}} \cdot \mathbf{n} \, ds + \frac{1}{\epsilon_0} \int_\Omega v \mathbf{J} \, d\Omega = 0, \tag{122a}$$

$$\int_\Omega v \partial_t \mathbf{B} \, d\Omega + \int_\Omega \mathbf{E} \times \nabla v \, d\Omega + \int_{\partial\Omega} v \underline{\mathbf{F}}_{\mathbf{B}} \cdot \mathbf{n} \, ds = 0, \tag{122b}$$

where the fluxes $\underline{\mathbf{F}}_{\mathbf{E}}$ and $\underline{\mathbf{F}}_{\mathbf{B}}$ along the boundary are given by

$$\underline{\mathbf{F}}_{\mathbf{E}} \stackrel{\text{def}}{=} \begin{pmatrix} 0 & -c^2 B_z & c^2 B_y \\ c^2 B_z & 0 & -c^2 B_x \\ -c^2 B_y & c^2 B_x & 0 \end{pmatrix} \quad \text{and} \quad \underline{\mathbf{F}}_{\mathbf{B}} \stackrel{\text{def}}{=} \begin{pmatrix} 0 & E_z & -E_y \\ -E_z & 0 & E_x \\ E_y & -E_x & 0 \end{pmatrix}. \tag{123}$$

6.2.2. Eliminated parabolic divergence cleaning

Accumulation of numerical errors can cause the electromagnetic fields computed through (120) to deviate from the divergence constraints (121). The eliminated parabolic cleaning method introduces penalty terms into each equation of (120), producing the following set of equations:

$$\partial_t \mathbf{E} - c^2 \nabla \times \mathbf{B} + \frac{1}{\epsilon_0}\mathbf{J} - \nabla \cdot \left[c_p^2 \left(\nabla \cdot \mathbf{E} - \frac{q}{\epsilon_0} \right) \underline{\mathbf{I}} \right] = \mathbf{0}, \tag{124a}$$

$$\partial_t \mathbf{B} + \nabla \times \mathbf{E} - \nabla \cdot \left[c_p^2 \left(\nabla \cdot \mathbf{B} \right) \underline{\mathbf{I}} \right] = \mathbf{0}, \tag{124b}$$

where $\underline{\mathbf{I}}$ is the 3×3 identity matrix and $c_p \in \mathbb{R}$ is a given penalty parameter. The finite element discretization of (124) is based on the weak form

$$\int_\Omega v \partial_t \mathbf{E} \, d\Omega - c^2 \int_\Omega \mathbf{B} \times \nabla v \, d\Omega + \int_{\partial\Omega} v \underline{\mathbf{F}}_{\mathbf{E}} \cdot \mathbf{n} \, ds + c_p^2 \int_\Omega \left(\nabla \cdot \mathbf{E} - \frac{q}{\epsilon_0} \right) \nabla v \, d\Omega + \frac{1}{\epsilon_0} \int_\Omega v \mathbf{J} \, d\Omega = 0, \tag{125a}$$

$$\int_\Omega v \partial_t \mathbf{B} \, d\Omega + \int_\Omega \mathbf{E} \times \nabla v \, d\Omega + \int_{\partial\Omega} v \underline{\mathbf{F}}_{\mathbf{B}} \cdot \mathbf{n} \, ds + c_p^2 \int_\Omega \left(\nabla \cdot \mathbf{B} \right) \nabla v \, d\Omega = 0. \tag{125b}$$

One of the primary difficulties with the use of this form of divergence cleaning is the selection of a suitable value for c_p. In general, this value must be chosen large enough to sufficiently penalize any deviation from the divergence constraints, but our experience also suggests that values that are too large can either degrade the numerical conditioning of the resulting finite element system significantly, or produce erroneous solutions. We have generally found that most problems tend to be rather insensitive to the value chosen for c_p when relatively coarse meshes are used. In these these situations, the value $c_p = \sqrt{0.18c}$ recommended in [30] typically works sufficiently well. However, solutions on much finer meshes tend to be much more sensitive to the value chosen for c_p, and the value $c_p = \sqrt{0.18c}$ is often too large. Motivated by the simple dimensional analysis in [27, 66], we have found that $c_p = \sqrt{hc}$ (where h denotes the size of the mesh) is a much more effective choice for the problems we have considered.

6.2.3. Implicit projection

In some cases, the divergence error in the electric field grows faster than the eliminated parabolic cleaning can address, regardless of the value chosen for c_p. In order to sufficiently constrain the evolution of the electromagnetic fields in these situations, we propose the following implicit projection scheme. It should be noted that this method is currently in the initial stages of development, and some unresolved issues (eg., solvability and enforcement of boundary conditions) are still being examined.

Over each timestep, the fields $\mathbf{E}$ and $\mathbf{B}$ are evolved as in (120). A pair of corrected fields

$$\hat{\mathbf{E}} \overset{\text{def}}{=} \mathbf{E} + \nabla \phi_{\mathbf{E}} \qquad \text{and} \qquad \hat{\mathbf{B}} \overset{\text{def}}{=} \mathbf{B} + \nabla \phi_{\mathbf{B}} \tag{126}$$

are evolved alongside the original fields, where the potentials $\phi_{\mathbf{E}}$ and $\phi_{\mathbf{B}}$ satisfy the equations

$$\epsilon_0 \nabla^2 \phi_{\mathbf{E}} + \epsilon_0 \nabla \cdot \mathbf{E} - q = 0, \tag{127a}$$

$$\nabla^2 \phi_{\mathbf{B}} + \nabla \cdot \mathbf{B} = 0. \tag{127b}$$

Using the definitions (126) in the divergence constraints (121) and applying the relations (127), it is clear that the corrected fields $\hat{\mathbf{E}}$ and $\hat{\mathbf{B}}$ satisfy the divergence constraints exactly.

The finite element discretization of (127) is based on the weak form

$$-\epsilon_0 \int_\Omega \left(\mathbf{E} + \nabla \phi_{\mathbf{E}} \right) \cdot \nabla v \, d\Omega + \epsilon_0 \int_{\partial\Omega} v \mathbf{E} \cdot \mathbf{n} \, ds - \int_\Omega v q \, d\Omega = 0, \tag{128a}$$

$$-\int_\Omega \left(\mathbf{B} + \nabla \phi_{\mathbf{B}} \right) \cdot \nabla v \, d\Omega + \int_{\partial\Omega} v \mathbf{B} \cdot \mathbf{n} \, ds = 0. \tag{128b}$$

Two observations should be made concerning the form of (128). First, by excluding the gradients of the potentials from the boundary fluxes, the conditions

$$\nabla\phi_{\mathbf{E}}\cdot\mathbf{n}=0 \qquad \text{and} \qquad \nabla\phi_{\mathbf{B}}\cdot\mathbf{n}=0 \tag{129}$$

are enforced weakly along the boundary. This is generally required in order to obtain good solutions. Second, the potentials $\phi_{\mathbf{E}}$ and $\phi_{\mathbf{B}}$ are defined only up to an additive constant. In order to remove the null space from the linear system that is obtained in the finite element discretization of (128), the values of the potentials may be fixed at a single point chosen in the interior of the computational domain. It is important to emphasize that this point should be chosen on the interior of the domain (not on the boundary), in order for the conditions (129) to be enforced along the boundary of the computational domain. If, for example, one chooses to remove this null space by utilizing a Dirichlet condition along some segment of the boundary (as is commonly done for the computation of electrostatic potentials) the corrected fields $\hat{\mathbf{E}}$ and $\hat{\mathbf{B}}$ that are produced will tend to be incorrect, and severe instabilities may result.

To ensure that the fluids are evolved consistently with the divergence constraints (121), the corrected fields $\hat{\mathbf{E}}$ and $\hat{\mathbf{B}}$ are used to evaluate the Lorentz force terms in the fluid equations: ie.,

$$\partial_t\left(\rho_s\mathbf{u}_s\right)+\nabla\cdot\left(\rho_s\mathbf{u}_s\otimes\mathbf{u}_s+p_s\underline{\mathbf{I}}+\underline{\boldsymbol{\Pi}}_s\right)=q_sn_s\left(\hat{\mathbf{E}}+\mathbf{u}_s\times\hat{\mathbf{B}}\right)+\cdots \tag{130a}$$

$$\partial_t\mathcal{E}_s+\nabla\cdot\left[\left(\mathcal{E}_s+p_s\right)\mathbf{u}_s+\mathbf{u}_s\cdot\underline{\boldsymbol{\Pi}}_s+\mathbf{h}_s\right]=q_sn_s\mathbf{u}_s\cdot\hat{\mathbf{E}}+\cdots \tag{130b}$$

Finally, at the end of each timestep, the original field $\mathbf{E}$ is overwritten by the corrected field $\hat{\mathbf{E}}$ before beginning the next timestep.

Our results have shown that this approach is able to reduce the divergence errors in the electromagnetic fields to machine precision. However, one significant disadvantage of this method is that the prescription of appropriate electromagnetic boundary conditions is much more complicated, and it is not always clear what the appropriate conditions are for a given situation. Periodic boundary conditions have proven to be particularly troublesome for this formulation. Our current hypothesis is that these non-physical potentials are unable to correctly represent this divergence error in the presence of periodic boundary conditions. This is consistent with the fact that the field generated by a periodic potential must have mean zero. If the vector field representing the divergence error has nonzero mean, then a periodic potential will be unable to represent (and correct for) this error. Possible approaches for resolving this issue include (i) not enforcing periodic conditions on $\phi_{\mathbf{E}}$ and $\phi_{\mathbf{B}}$ when periodic conditions are used for the physical variables, and (ii) adding an additional set of unknowns to represent the mean value of the divergence error, so that (126) becomes

$$\hat{\mathbf{E}}\overset{\text{def}}{=}\mathbf{E}+\nabla\phi_{\mathbf{E}}+\overline{\boldsymbol{\Phi}}_{\mathbf{E}} \qquad \text{and} \qquad \hat{\mathbf{B}}\overset{\text{def}}{=}\mathbf{B}+\nabla\phi_{\mathbf{B}}+\overline{\boldsymbol{\Phi}}_{\mathbf{B}}, \tag{131}$$

where $\overline{\boldsymbol{\Phi}}_{\mathbf{E}}$ and $\overline{\boldsymbol{\Phi}}_{\mathbf{B}}$ are functions of time only. Unfortunately, at this point we have not been able to test any of the suggested approaches for applying this method to problems with periodic boundary conditions.

6.3. Potential form of Maxwell's equations

The evolution of the electric field $\mathbf{E}$ and magnetic field $\mathbf{B}$ may alternatively be described by an electric potential ϕ and a magnetic vector potential $\mathbf{A}$, such that

$$\mathbf{E}=-\nabla\phi-\partial_t\mathbf{A}, \tag{132a}$$

$$\mathbf{B}=\nabla\times\mathbf{A}. \tag{132b}$$

Under the Lorenz gauge

$$\partial_t\phi+c^2\nabla\cdot\mathbf{A}=0, \tag{133}$$

the potentials satisfy the system of wave equations

$$\partial_t^2\phi-c^2\nabla^2\phi=\frac{c^2}{\varepsilon_0}q, \tag{134a}$$

$$\partial_t^2\mathbf{A}-c^2\nabla^2\mathbf{A}=\frac{1}{\epsilon_0}\mathbf{J}. \tag{134b}$$

Introducing a set of auxiliary variables

$$\mathbf{C} \stackrel{\text{def}}{=} \frac{1}{c}\partial_t \mathbf{A} \qquad \text{and} \qquad \psi \stackrel{\text{def}}{=} \frac{1}{c}\partial_t \phi, \tag{135}$$

the system (134) can be written in the following first-order form:

$$\partial_t \psi - c\nabla^2 \phi = \frac{c}{\epsilon_0} q, \tag{136a}$$

$$\partial_t \phi - c\psi = 0, \tag{136b}$$

$$\partial_t \mathbf{C} - c\nabla^2 \mathbf{A} = \frac{1}{c\epsilon_0}\mathbf{J}, \tag{136c}$$

$$\partial_t \mathbf{A} - c\mathbf{C} = \mathbf{0}, \tag{136d}$$

so that (132) becomes

$$\mathbf{E} = -\nabla\phi - c\mathbf{C}, \tag{137a}$$

$$\mathbf{B} = \nabla \times \mathbf{A}. \tag{137b}$$

6.3.1. Finite element discretization

Given a convex domain $\Omega \subset \mathbb{R}^3$ with boundary $\partial\Omega$, the finite element discretization of (136) is based on the weak form

$$\int_\Omega v\partial_t \psi \, d\Omega + c\int_\Omega \nabla\phi \cdot \nabla v \, d\Omega + \int_{\partial\Omega} v\mathbf{F}_\phi \cdot \mathbf{n} \, ds - \frac{c}{\epsilon_0}\int_\Omega v q \, d\Omega = 0, \tag{138a}$$

$$\int_\Omega v\partial_t \phi \, d\Omega - c\int_\Omega v\psi \, d\Omega = 0, \tag{138b}$$

$$\int_\Omega v\partial_t \mathbf{C} \, d\Omega + c\int_\Omega \nabla\mathbf{A} \cdot \nabla v \, d\Omega + \int_{\partial\Omega} v\underline{\mathbf{F}}_\mathbf{A} \cdot \mathbf{n} \, ds - \frac{1}{c\epsilon_0}\int_\Omega v\mathbf{J} \, d\Omega = 0, \tag{138c}$$

$$\int_\Omega v\partial_t \mathbf{A} \, d\Omega - c\int_\Omega v\mathbf{C} \, d\Omega = 0. \tag{138d}$$

The fluxes $\mathbf{F}_\phi$ and $\underline{\mathbf{F}}_\mathbf{A}$ may be chosen to enforce a range of boundary conditions. The natural fluxes, given by

$$\mathbf{F}_\phi = -c\nabla\phi, \tag{139a}$$

$$\underline{\mathbf{F}}_\mathbf{A} = -c\nabla\mathbf{A}, \tag{139b}$$

are typically used in combination with a set of constraints to be enforced.

To enforce the condition $\mathbf{E}\cdot\mathbf{n} = 0$, (137a) implies that replacing the natural flux (139a) with

$$\mathbf{F}_\phi = c^2\mathbf{C} \tag{140}$$

is sufficient.

The radiation conditions [80, 84]

$$\partial_t \phi + c\nabla\phi \cdot \mathbf{n} = 0, \tag{141a}$$

$$\partial_t \mathbf{A} + c\nabla\mathbf{A} \cdot \mathbf{n} = \mathbf{0}, \tag{141b}$$

may be used to permit waves traveling in a direction exactly normal to the boundary to exit the computational domain without reflections, where $\mathbf{n}$ is the unit outward normal along the boundary. To enable outflow in numerical simulations, we utilize the fluxes

$$\mathbf{F}_\phi = c\psi\mathbf{n}, \tag{142a}$$

$$\underline{\mathbf{F}}_\mathbf{A} = c\mathbf{C} \otimes \mathbf{n}. \tag{142b}$$

It should be noted that a well-known difficulty associated with radiation conditions of this form is that components of waves that do not propagate in a direction that is exactly perpendicular to the boundary will be reflected in numerical simulations. In general, we therefore restrict the use of these outflow conditions to one-dimensional geometries.

6.3.2. An elliptic equation for the scalar potential

One of the advantages offered by the potential formulation (134) is control over the divergence error of **B**. In general, the divergence error in **B** is bounded by the discretization error of the discrete curl operator that is used to evaluate (132b). More importantly, this divergence error is not cumulative, since the time evolution of the potentials is not dependent on the value of **B**. However, satisfaction of the divergence constraint (121a) on **E** relies on the extent to which the computed potentials satisfy the gauge condition (133). Substituting (132a) followed by (134a) into the expression $\nabla \cdot \mathbf{E}$ shows this explicitly:

$$\nabla \cdot \mathbf{E} = -\nabla^2 \phi - \partial_t \nabla \cdot \mathbf{A} = \frac{q}{\varepsilon_0} - \frac{1}{c^2} \partial_t \Big(\partial_t \phi + c^2 \nabla \cdot \mathbf{A} \Big). \tag{143}$$

In most cases, we have found that this error is well controlled without having to apply any additional gauge cleaning procedures, which agrees with the observations of [36].

However, there are occasions where the numerical implementation fails to adequately satisfy the gauge condition, and the solution becomes unstable. In these situations, we can replace (134a) with an equivalent elliptic equation that necessarily ensures that the divergence constraint (121a) on **E** is satisfied to numerical precision [99]. Using the gauge condition (133) to substitute for $\partial_t \phi$ in (134a) yields

$$-\nabla \cdot \big(\nabla \phi + \partial_t \mathbf{A} \big) - \frac{q}{\varepsilon_0} = 0. \tag{144}$$

The equation (144) is used in combination with (134b) to produce the full electromagnetics model. Using the definition (132a) for **E** in (144) implies that the divergence constraint (121a) is directly enforced to numerical precision by this formulation.

The finite element discretization of (144) is based on the weak form

$$\int_\Omega \nabla v \cdot \big(\nabla \phi + c\mathbf{C} \big) \, d\Omega + \int_{\partial\Omega} v \mathbf{F}_\phi \cdot \mathbf{n} \, ds - \frac{1}{\varepsilon_0} \int_\Omega v q \, d\Omega = 0, \tag{145}$$

where we have used the auxiliary vector potential defined in (135). In this case, the natural flux for $\mathbf{F}_\phi$ is given by

$$\mathbf{F}_\phi = -\nabla \phi - c\mathbf{C} = \mathbf{E}. \tag{146}$$

Enforcement of the condition $\mathbf{E} \cdot \mathbf{n} = 0$ can be achieved by simply setting

$$\mathbf{F}_\phi = 0. \tag{147}$$

Substituting for $\partial_t \phi$ in (141a) using the gauge condition (133) yields the equivalent relation

$$-c \nabla \cdot \mathbf{A} + \nabla \phi \cdot \mathbf{n} = 0. \tag{148}$$

Thus the flux

$$\mathbf{F}_\phi = -c \, (\nabla \cdot \mathbf{A}) \, \mathbf{n} + c\mathbf{C} \tag{149}$$

is used to enable outflow in one-dimensional simulations.

When used in combination with the first order equations (138c) and (138d) for the vector potential, this model yields a system consisting of only seven equations, whereas the previous potential formulation in purely hyperbolic form requires eight. More importantly, we have observed no stability issues with this formulation in any of the verification problems we have considered.

7. IMPLEMENTATION VERIFICATION

7.1. Spatially homogeneous plasma oscillations

A collection of tests are considered here with the aim of verifying that the various source terms required for the general multifluid model described in section 2 are correctly implemented. For the tests in this subsection it is assumed that:

(i) all quantities lack spatial gradients; and

(ii) all external source terms ($\mathcal{S}_s^{[0]}$, $\boldsymbol{\mathcal{S}}_s^{[1]}$, $\mathcal{S}_s^{[2]}$) are zero.

In this case, the fluid equations (5) reduce to

$$\partial_t \rho_s = \mathcal{C}_s^{[0]}, \tag{150a}$$

$$\partial_t \left(\rho_s \mathbf{u}_s\right) = \frac{q_s}{m_s}\rho_s \left(\mathbf{E} + \mathbf{u}_s \times \mathbf{B}\right) + \boldsymbol{\mathcal{C}}_s^{[1]}, \tag{150b}$$

$$\partial_t \mathcal{E}_s = \frac{q_s}{m_s}\rho_s \mathbf{u}_s \cdot \mathbf{E} + \mathcal{C}_s^{[2]}. \tag{150c}$$

7.1.1. Collisional relaxation

First, we consider the transfer of momentum and energy between a collection of two or more species through elastic collisions. Including only interactions due to elastic scattering collisions, the momentum and energy sources for each species, using (43) and (59), are given by

$$\boldsymbol{\mathcal{C}}_s^{[1]} = \sum_{t \neq s} \alpha_{s;t}\rho_s\rho_t \left(\mathbf{u}_t - \mathbf{u}_s\right), \tag{151a}$$

$$\mathcal{C}_s^{[2]} = \sum_{t \neq s} \left[\alpha_{s;t}\rho_s\rho_t \mathbf{u}_s \cdot \left(\mathbf{u}_t - \mathbf{u}_s\right) + \frac{\alpha_{s;t}\rho_s\rho_t}{m_s + m_t}\left[3k_\mathrm{B}\left(T_t - T_s\right) + m_t\left(\mathbf{u}_t - \mathbf{u}_s\right)^2\right]\right]. \tag{151b}$$

An equation of state for an ideal monatomic gas is assumed for each species, so that the internal energy densities satisfy

$$\rho_s e_s = \frac{1}{\gamma - 1} n_s k_\mathrm{B} T_s, \tag{152}$$

with $\gamma = 5/3$. The electric field $\mathbf{E}$ and magnetic field $\mathbf{B}$ are both assumed to be zero (ie., external fields are assumed to be absent and the contributions from any fields induced by the motion of charged particles are neglected).

In these tests, the species simply relax to common velocity and temperature values $\mathbf{u}_*$ and T_* as $t \to \infty$. By conservation of momentum, it must hold that

$$\sum_s \rho_s \mathbf{u}_s = \mathbf{u}_* \sum_s \rho_s \tag{153a}$$

for all times, which implies that

$$\mathbf{u}_* = \frac{\sum_s \rho_s \mathbf{u}_s}{\sum_s \rho_s}. \tag{153b}$$

Similarly, conservation of energy requires that

$$\sum_s \mathcal{E}_s = \sum_s \left(\frac{1}{2}\rho_s \mathbf{u}_s^2 + \frac{1}{\gamma - 1} n_s k_\mathrm{B} T_s\right) = \frac{1}{2}\mathbf{u}_*^2 \sum_s \rho_s + \frac{1}{\gamma - 1} k_\mathrm{B} T_* \sum_s n_s, \tag{153c}$$

for all times, which implies that

$$T_* = \frac{\sum_s \mathcal{E}_s - \frac{1}{2}\mathbf{u}_*^2 \sum_s \rho_s}{\frac{1}{\gamma - 1} k_\mathrm{B} \sum_s n_s}. \tag{153d}$$

We consider two settings: a two-fluid configuration and a three-fluid configuration. The initial conditions for both tests are shown in table 7.1. Only ions and electrons are included in the two-fluid case. Solutions computed using the Drekar code were compared to: (i) the time evolution of an explicit ODE solver applied to a reduced system for the velocities and temperatures of the species, and (ii) the analytic equilibrium values given by (153). Deviations of all values from the equilibrium quantities are computed in a relative sense; eg.,

$$\left|\frac{T_s - T_*}{T_*}\right|. \tag{154}$$

	Neutral (n)	Ion (i)	Electron (e)
m_s	3.0E-27	2.0E-27	1.0E-27
T_s	1.0E+3	1.0E+4	2.0E+4
$\mathbf{u}_s$	$\begin{bmatrix}0.0\\0.0\\0.0\end{bmatrix}$	$\begin{bmatrix}1.0\text{E}{+4}\\0.0\\0.0\end{bmatrix}$	$\begin{bmatrix}-1.4\text{E}{+4}\\0.0\\0.0\end{bmatrix}$
n_s	4.0E+16	2.0E+16	2.0E+16

	Neutral (n)	Ion (i)	Electron (e)
ρ_s	1.2E-10	4.0E-11	2.0E-11
$\rho_s\mathbf{u}_s$	$\begin{bmatrix}0.0\\0.0\\0.0\end{bmatrix}$	$\begin{bmatrix}4.0\text{E}{-7}\\0.0\\0.0\end{bmatrix}$	$\begin{bmatrix}-2.8\text{E}{-7}\\0.0\\0.0\end{bmatrix}$
$\rho_s e_s$	8.2860E-4	4.1430E-3	8.2860E-3
$\mathcal{E}_s$	8.2860E-4	6.1430E-3	1.0246E-2

TABLE 7.1. Initial conditions for verification problems for implementation of elastic collision sources.

If the friction coefficients $\alpha_{s;t}$ are assumed to be constant, analytic solutions may be derived for the two-fluid case. The velocity difference between species is given by

$$\mathbf{u}_e(t) - \mathbf{u}_i(t) = \left(\mathbf{u}_e(t_0) - \mathbf{u}_i(t_0)\right)\exp\left(-A_{e;i}\,t\right), \tag{155a}$$

where

$$A_{e;i} = \alpha_{e;i}\left(\rho_e + \rho_i\right), \tag{155b}$$

and the temperature difference between species is given by

$$T_e(t) - T_i(t) = \left(T_e(t_0) - T_i(t_0)\right)\exp\left(-B_{e;i}\,t\right) + \frac{C_{e;i}}{B_{e;i} - 2A_{e;i}}\left[\exp\left(-2A_{e;i}\,t\right) - \exp\left(-B_{e;i}\,t\right)\right], \tag{155c}$$

where

$$B_{e;i} = 3\left(\gamma - 1\right)\alpha_{e;i}\frac{m_e m_i}{m_e + m_i}\left(n_e + n_i\right), \tag{155d}$$

$$C_{e;i} = \frac{\gamma - 1}{k_\text{B}}\alpha_{e;i}\left(\rho_i - \rho_e\right)\frac{m_e m_i}{m_e + m_i}\left(\mathbf{u}_e(t_0) - \mathbf{u}_i(t_0)\right)^2. \tag{155e}$$

The time evolution of numerically computed velocity and temperature values from Drekar and an explicit ODE solver are compared in fig. 7.2. Further, each solver is compared to the analytic solutions (155) for the two-fluid case. We observe that: (i) the numerical implementations are in very good agreement, (ii) each numerical implementation relaxes toward the appropriate equilibrium values, and (iii) both numerical implementations yield small errors relative to the analytic solutions for the two-fluid case. The results of convergence studies using various implicit time-integration schemes made available through the Tempus library are shown in fig. 7.1 at time $t = 4.0\text{E}{-8}$. The expected convergence orders are observed for all schemes considered.

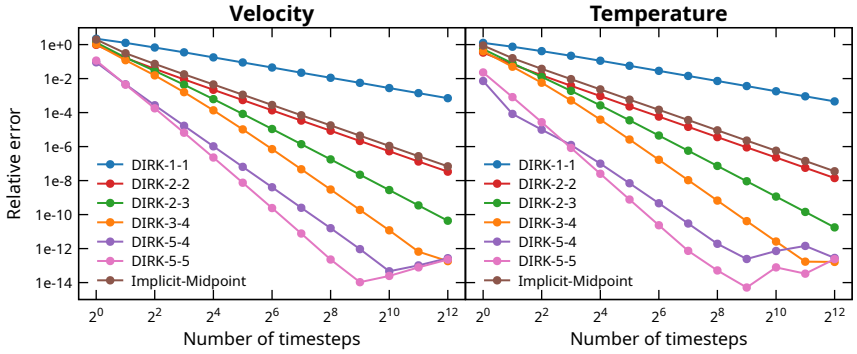

FIGURE 7.1. Convergence of velocity and temperature values for two-fluid collisional relaxation problems using a variety of implicit time integration schemes from the Tempus library. Error values are computed in a relative norm using the analytic values (155) at the final time $t = 4.0\text{E}{-8}$.

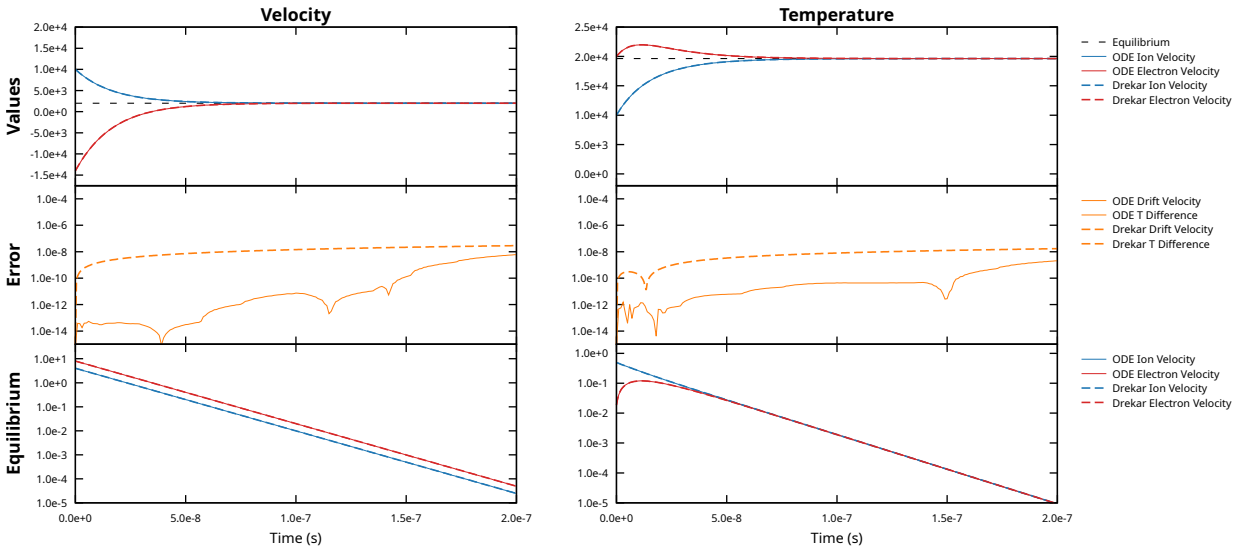

(A) Two-fluid velocity and temperature relaxation with $\alpha_{e;i} = 1.0\text{E}{+}18$.

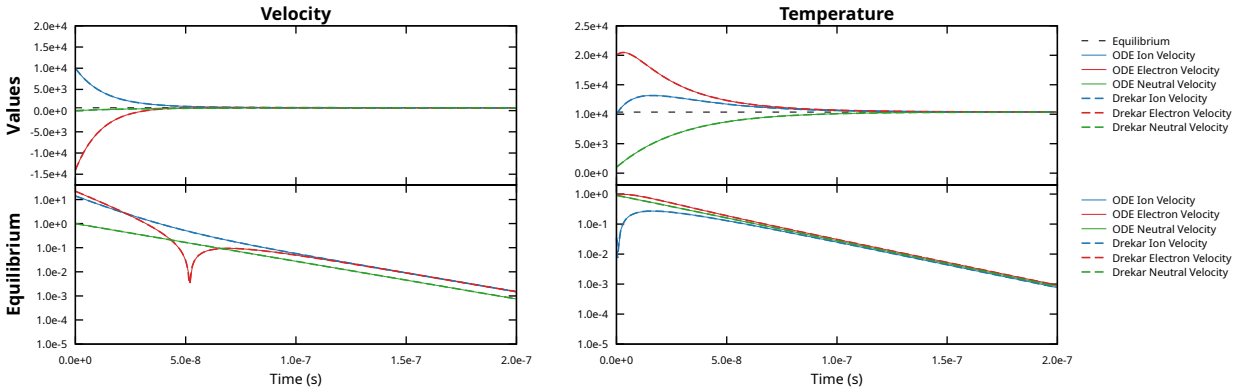

(B) Three-fluid velocity and temperature relaxation with $\alpha_{e;i} = 1.0\text{E}{+}18$ and $\alpha_{n;e} = \alpha_{n;i} = 2.0\text{E}{+}17$.

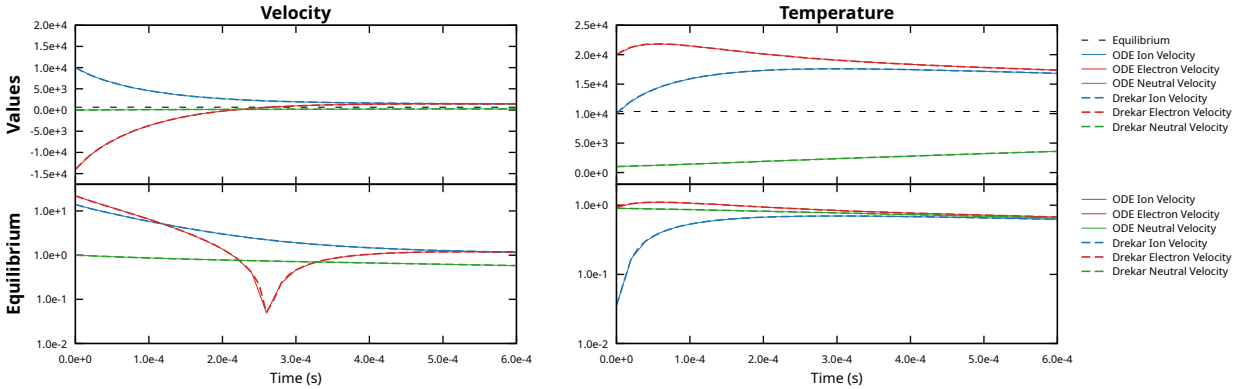

(C) Three-fluid velocity and temperature relaxation with friction coefficients computed using (45) and (48).

FIGURE 7.2. Velocity and temperature values for two- and three-fluid collisional relaxation problems. The rows of each subfigure show: (i) the computed velocity and temperature values ("Values"), (ii) the relative error in the computed velocity and temperature difference between species compared to the analytic solutions (155) ("Error"), and (iii) the deviation (in a relative sense) of the computed velocity and temperature values from the equilibrium values (153) ("Equilibrium").

7.1.2. Damped plasma oscillation

We now consider configurations where the effects of electric fields induced by the motion of charged particles are included, but contributions due to magnetic fields and external electric fields are omitted. Here the evolution of the electric field $\mathbf{E}$ is described by

$$\epsilon_0 \partial_t \mathbf{E} + \mathbf{J} = \mathbf{0}, \tag{156}$$

where ϵ_0 is the permittivity of free space and the total current density $\mathbf{J}$ is given by

$$\mathbf{J} \stackrel{\text{def}}{=} \sum_s \frac{q_s}{m_s} \rho_s \mathbf{u}_s. \tag{157}$$

We consider three scenarios:

(i) A collisionless two-fluid system containing an ion and an electron species interacting only through the electric field coupling. The result is a perfect harmonic oscillator.

(ii) A collisional two-fluid system containing an ion and an electron species with constant friction coefficients with the value $\alpha_{e;i} = 1.0\text{E}{+}18$. The result is a damped oscillation.

(iii) A collisional three-fluid system containing an ion, an electron, and a neutral species with constant friction coefficients $\alpha_{e;i} = 1.0\text{E}{+}18$ and $\alpha_{n;e} = \alpha_{n;i} = 2.0\text{E}{+}17$. The result is again a damped oscillation.

If the friction coefficients $\alpha_{s;t}$ are assumed to be constant, analytic solutions may be derived for the two-fluid case with the additional assumption of charge-neutrality; ie., we assume that $n_i = n_e$ in this case. For the velocity difference between the two charged species, the analytic solution is given by

$$\mathbf{u}_e(t) - \mathbf{u}_i(t) = \big(\mathbf{u}_e(t_0) - \mathbf{u}_i(t_0)\big) \exp\left(-\frac{\nu_{e;i}\, t}{2}\right) \frac{\cos\big(\eta_{e;i}\, t - \phi_{e;i}\big)}{\cos\phi_{e;i}}, \tag{158a}$$

where

$$\nu_{e;i} = \alpha_{e;i}\big(\rho_e + \rho_i\big), \qquad \omega_{e;i}^2 = \frac{q_e^2}{\epsilon_0} n_i \left(\frac{1}{m_e} + \frac{1}{m_i}\right), \tag{158b}$$

$$\eta_{e;i}^2 = \omega_{e;i}^2 - \frac{\nu_{e;i}^2}{4}, \qquad \phi_{e;i} = \tan^{-1}\left(-\frac{\nu_{e;i}}{2\eta_{e;i}}\right). \tag{158c}$$

The electric field $\mathbf{E}$, which is initially zero, is given by

$$\begin{aligned}\mathbf{E}(t) = -\big(\mathbf{u}_e(t_0) - \mathbf{u}_i(t_0)\big) \frac{q_e n_i}{\epsilon_0} \frac{\exp\big(-\nu_{e;i}\, t/2\big)}{\omega_{e;i}^2 \cos\phi_{e;i}} \Big[\eta_{e;i} \sin\big(\eta_{e;i}\, t - \phi_{e;i}\big) - \frac{\nu_{e;i}}{2} \cos\big(\eta_{e;i}\, t - \phi_{e;i}\big) \\ + \exp\big(\nu_{e;i}\, t/2\big)\Big(\frac{\nu_{e;i}}{2} \cos\phi_{e;i} + \eta_{e;i} \sin\phi_{e;i}\Big)\Big].\end{aligned} \tag{158d}$$

The temperature difference between the charge species is given by

$$\begin{aligned}T_e(t) - T_i(t) = \exp\big(-A_{e;i}\, t\big) C_{e;i} + \frac{D_{e;i} \exp\big(-\nu_{e;i}\, t\big)}{\cos^2\phi_{e;i}} \Big[4\eta_{e;i}^2 + 2G_{e;i}^2 \cos^2\big(\eta_{e;i}\, t - \phi_{e;i}\big) \\ + 4\eta_{e;i} G_{e;i} \sin\big(\eta_{e;i}\, t - \phi_{e;i}\big) \cos\big(\eta_{e;i}\, t - \phi_{e;i}\big)\Big]\end{aligned} \tag{158e}$$

where

$$A_{e;i} = 2\alpha_{e;i} \frac{m_e m_i}{m_e + m_i} (n_e + n_i), \tag{158f}$$

$$B_{e;i} = \frac{\gamma - 1}{k_{\text{B}}} \alpha_{e;i} \big(\rho_i - \rho_e\big) \frac{m_e m_i}{m_e + m_i} \big(\mathbf{u}_e(t_0) - \mathbf{u}_i(t_0)\big)^2, \tag{158g}$$

$$C_{e;i} = \big(T_e(t_0) - T_i(t_0)\big) - D_{e;i} \left[\frac{4\eta_{e;i}^2}{\cos^2\phi_{e;i}} + 2G_{e;i}\Big(G_{e;i} - 2\eta_{e;i} \tan\phi_{e;i}\Big)\right], \tag{158h}$$

$$D_{e;i} = \frac{B_{e;i}}{2G_{e;i}\left(4\eta_{e;i}^2 + G_{e;i}^2\right)}, \tag{158i}$$

$$G_{e;i} = A_{e;i} - \nu_{e;i}. \tag{158j}$$

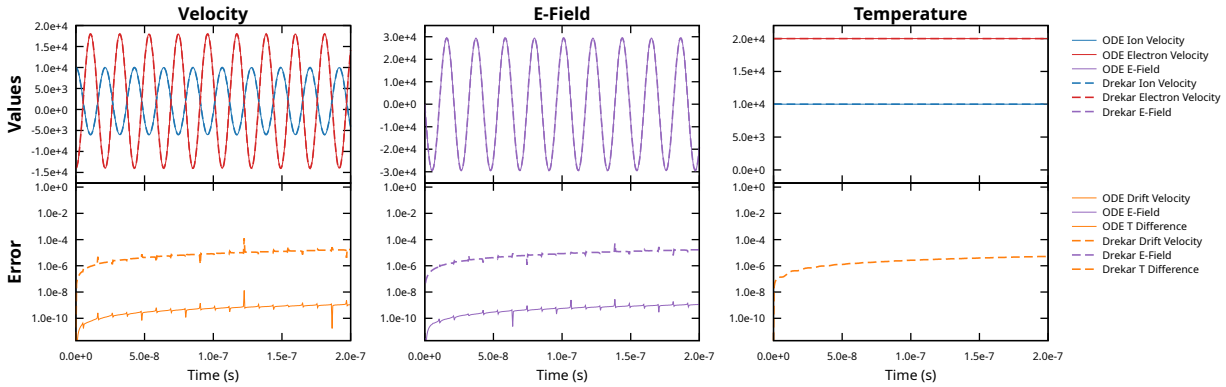

(A) Two-fluid collisionless oscillation.

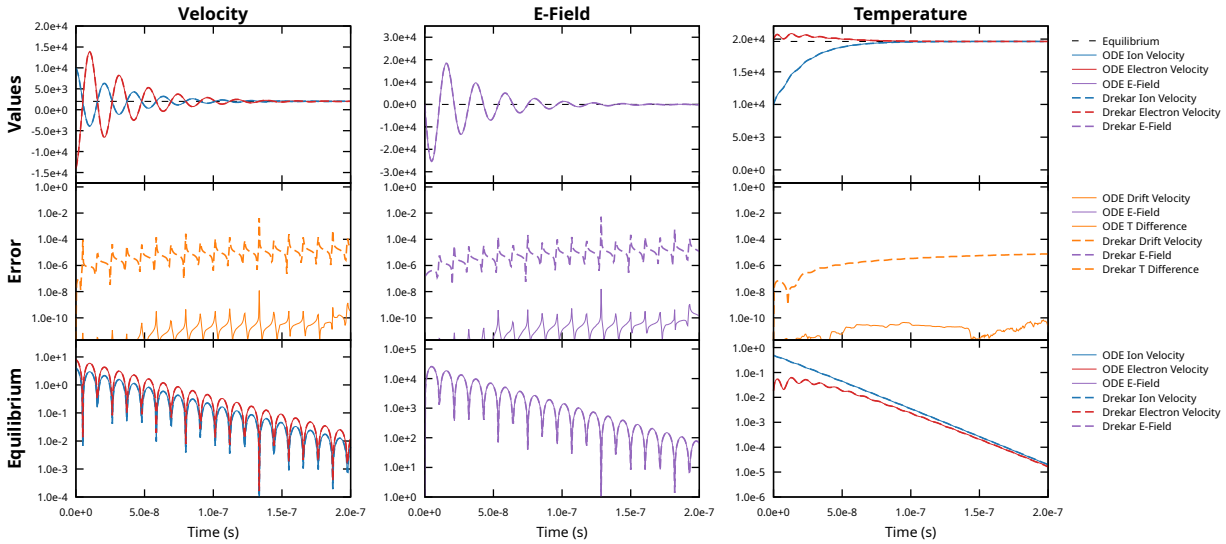

(B) Two-fluid damped oscillation with $\alpha_{e;i} = 1.0\text{E}{+}18$.

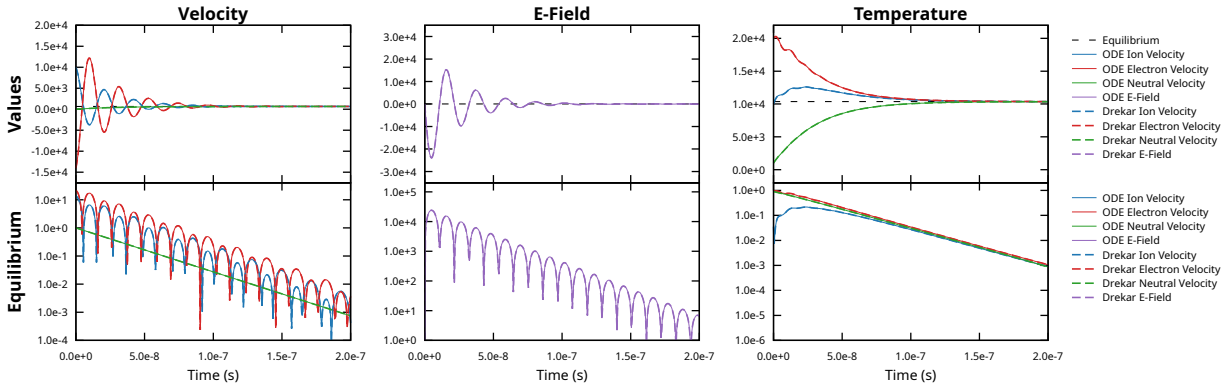

(C) Three-fluid damped oscillation with $\alpha_{e;i} = 1.0\text{E}{+}18$ and $\alpha_{n;e} = \alpha_{n;i} = 2.0\text{E}{+}17$.

FIGURE 7.3. Velocity, temperature, and electric field values for two- and three-fluid collisional and collisionless plasma oscillations using the curl form of Maxwell's equations. The rows of each subfigure show: (i) the computed velocity, temperature, and electric field values ("Values"), (ii) the relative error in the computed velocity difference, temperature difference, and generated electric field values compared to the analytic solutions (158) ("Error"), and (iii) the deviation (in a relative sense) of the computed velocity and temperature values from the equilibrium values (153) ("Equilibrium").

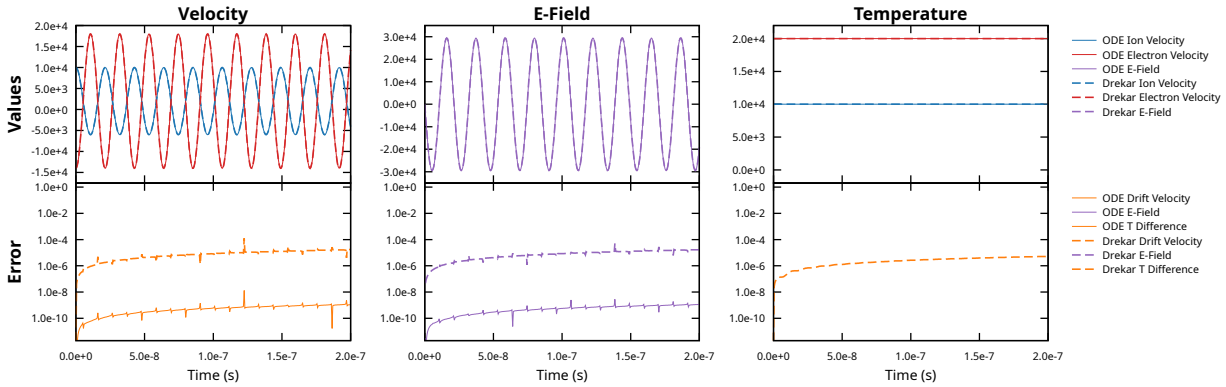

(A) Two-fluid collisionless oscillation.

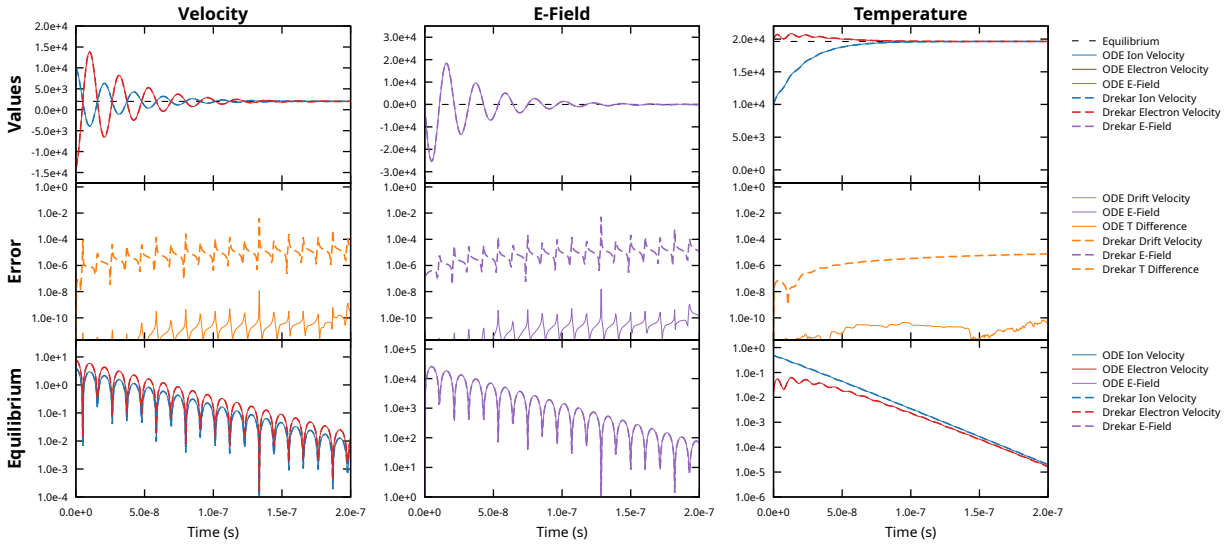

(B) Two-fluid damped oscillation with $\alpha_{e;i} = 1.0\text{E}{+}18$.

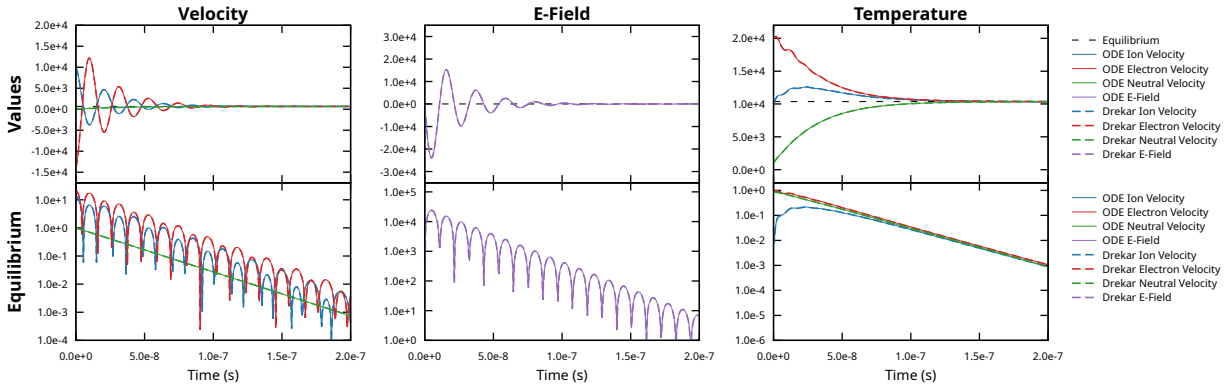

(C) Three-fluid damped oscillation with $\alpha_{e;i} = 1.0\text{E}{+}18$ and $\alpha_{n;e} = \alpha_{n;i} = 2.0\text{E}{+}17$.

FIGURE 7.4. Velocity, temperature, and electric field values for two- and three-fluid collisional and collisionless plasma oscillations using the potential form of Maxwell's equations. The rows of each subfigure show: (i) the computed velocity, temperature, and electric field values ("Values"), (ii) the relative error in the computed velocity difference, temperature difference, and generated electric field values compared to the analytic solutions (158) ("Error"), and (iii) the deviation (in a relative sense) of the computed velocity and temperature values from the equilibrium values (153) ("Equilibrium").

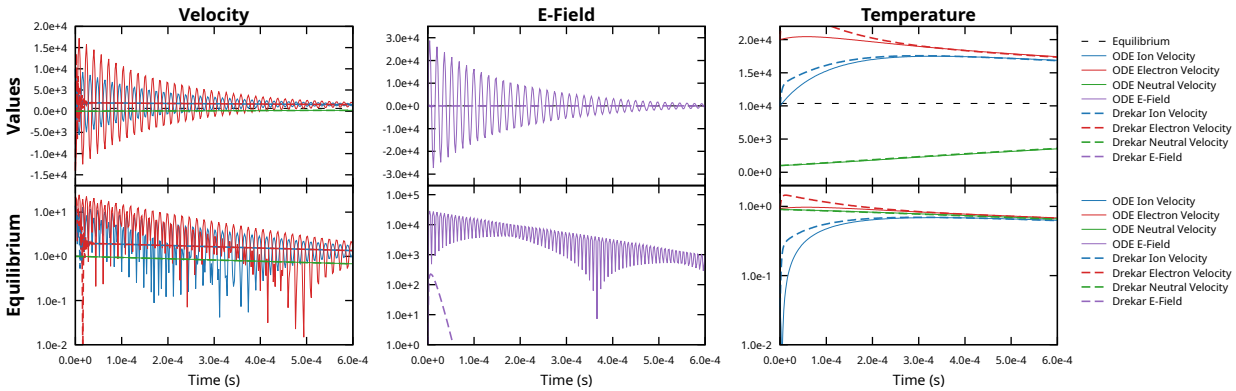

(A) Curl form of Maxwell's equations, A-stable integrator.

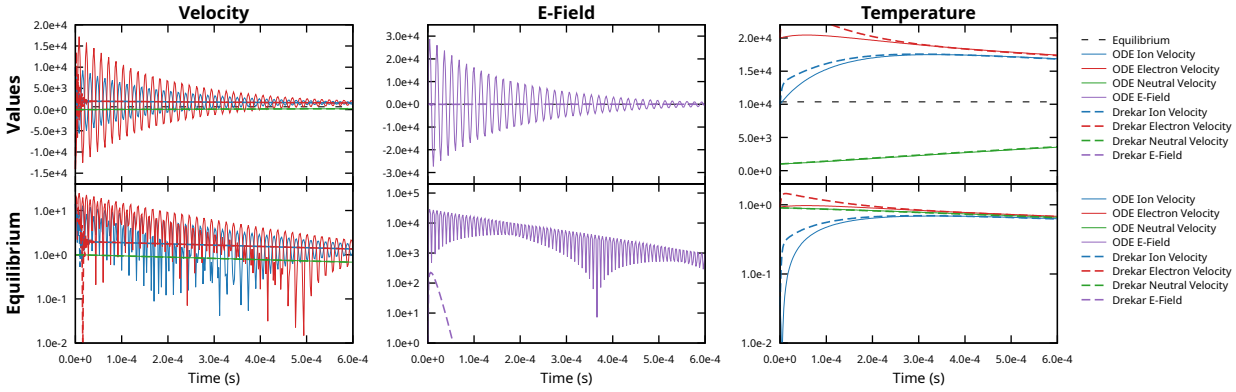

(B) Potential form of Maxwell's equations, A-stable integrator.

FIGURE 7.5. Same as figs. 7.3 and 7.4 with friction coefficients computed by (45) and (48). Timesteps for the ODE solver are adaptively chosen to be small enough to resolve the oscillation frequency, while the Drekar code leverages an A-stable implicit DIRK scheme with a timestep size of $2\text{E}{-6}$ to step over the timescale of the plasma oscillation.

The time evolution of numerically computed velocity and temperature values from Drekar and an explicit ODE solver (written in python) are compared in figs. 7.3 and 7.4, using the curl form and potential form of Maxwell's equations, respectively. Further, each solver is compared to the analytic solutions (158) for the two-fluid cases. We again observe that: (i) the numerical implementations are in very good agreement, (ii) each numerical implementation relaxes toward the appropriate equilibrium values, and (iii) both numerical implementations yield small errors relative to the analytic two-fluid solutions.

Additional results are shown in figs. 7.5 and 7.6 for the three-fluid case with friction coefficients computed using (45) and (48). In this case, the timescale of the collisional relaxation process is significantly longer than that of the plasma oscillation of the charged species. In order to numerically integrate the solution at a time scale that is larger than that required to resolve the oscillation, an implicit time integration scheme with appropriate stability properties may be used. Here we consider diagonally implicit Runge-Kutta (DIRK) schemes. In general, the construction of DIRK schemes involves a tradeoff between order of accuracy and stability properties. For a two-stage DIRK method, the typical choice of methods is either a second-order L-stable scheme, or a third-order A-stable scheme [43]. In figs. 7.5 and 7.6, the impact of L-stability over A-stability is clear: the L-stable method integrates over the fast plasma oscillation with essentially no oscillatory features, whereas the A-stable method is able to integrate over the fast plasma oscillation, but produces some amount of unresolved oscillatory behavior. The two methods nevertheless produce similar behavior in the longer-time limit, but the L-stable scheme is better able to damp the effects of the unresolved physics.

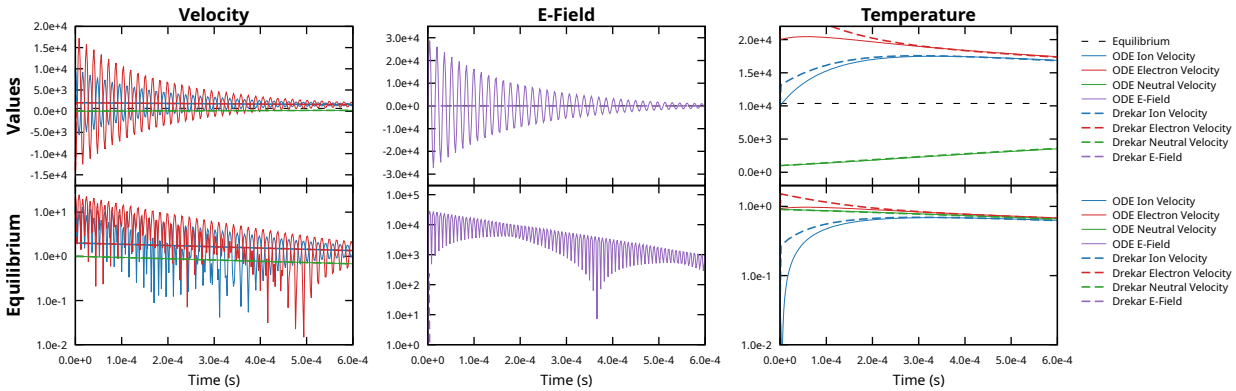

(A) Curl form of Maxwell's equations, L-stable integrator.

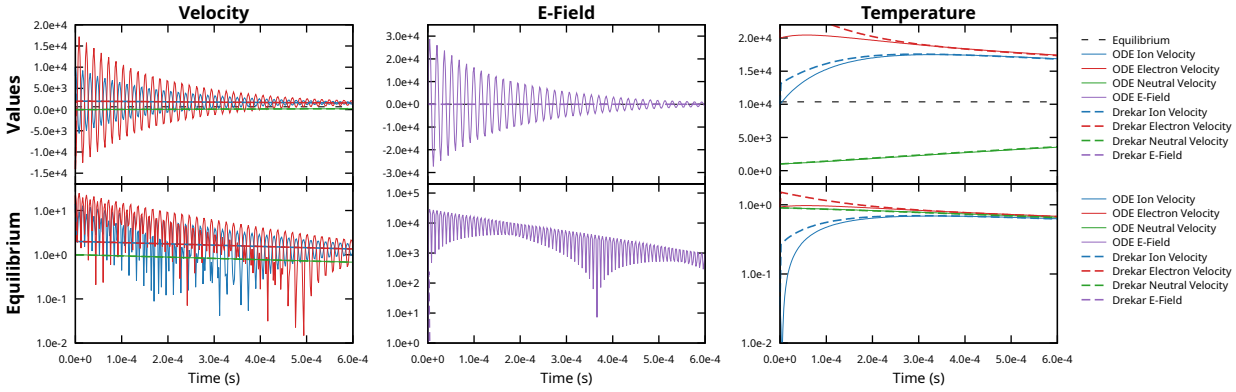

(B) Potential form of Maxwell's equations, L-stable integrator.

FIGURE 7.6. Same as figs. 7.3 and 7.4 with friction coefficients computed by (45) and (48). Timesteps for the ODE solver are adaptively chosen to be small enough to resolve the oscillation frequency, while the Drekar code leverages an L-stable implicit DIRK scheme with a timestep size of 2E−6 to step over the timescale of the plasma oscillation.

The results of convergence studies for the two-fluid oscillations (for which analytic solutions are available) using various implicit time-integration schemes made available through the Tempus library are shown in fig. 7.7 at time $t = 4\text{E}{-8}$.

7.2. Ionization and recombination

We now turn our attention to the implementation of the ionization and recombination rates. To ensure that the implemented rate values are correct, we compare the average charge state values generated by: (i) directly computing equilibrium ionization fractions (using the QSS-CIE approach described in section 3.2), and (ii) integrating the time-dependent fluid system in Drekar to reach an equilibrium state. Here only the ionization and recombination source terms are included in (150). Further, we do not evolve the total energy variables for each fluid in this case, but simply assume that all fluids have a common constant temperature value. Each test contains an electron species and all charge states of one atomic species, with a total ion number density of 10^{24} m^{-3}. The ionization fractions for each charge state are initially equal. In order to ensure that the reactions progress reasonably quickly even in the low-temperature limit (where the average charge state would be near zero) we do not assume quasi-neutrality: instead, we increase the initial electron number density by 10^{24} m^{-3} beyond the quasi-neutral density value. That is, the initial electron number density is given by $10^{24}(1+\overline{Z}_0)$, where $\overline{Z}_0$ is the initial average ion charge state.

The temperature of all species is set to the same constant value, and each system is integrated to a final time of

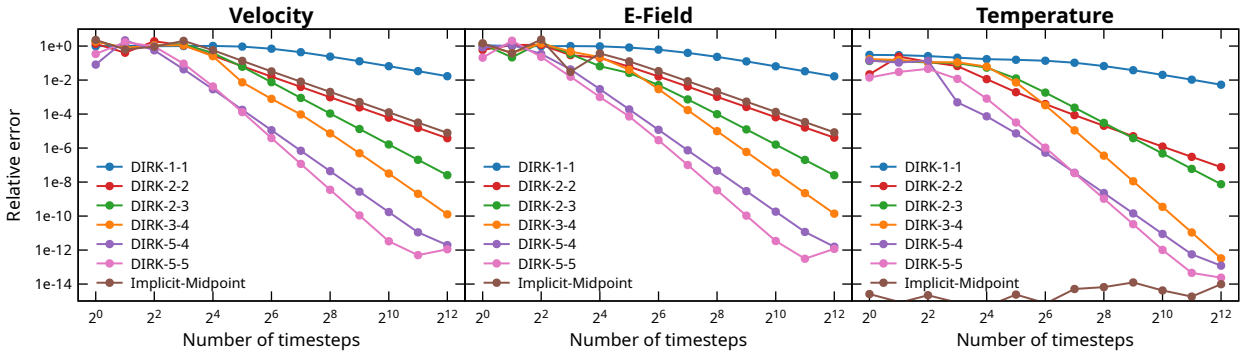

(A) Collisionless; Maxwell curl form; Implicit methods (Tempus).

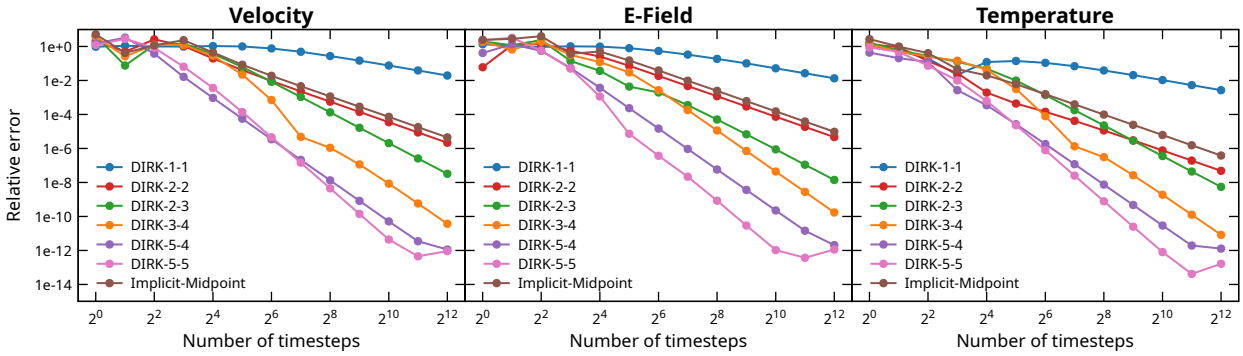

(B) Collisional ($\alpha_{e;i}$ = 1.0E+18); Maxwell curl form; Implicit methods (Tempus).

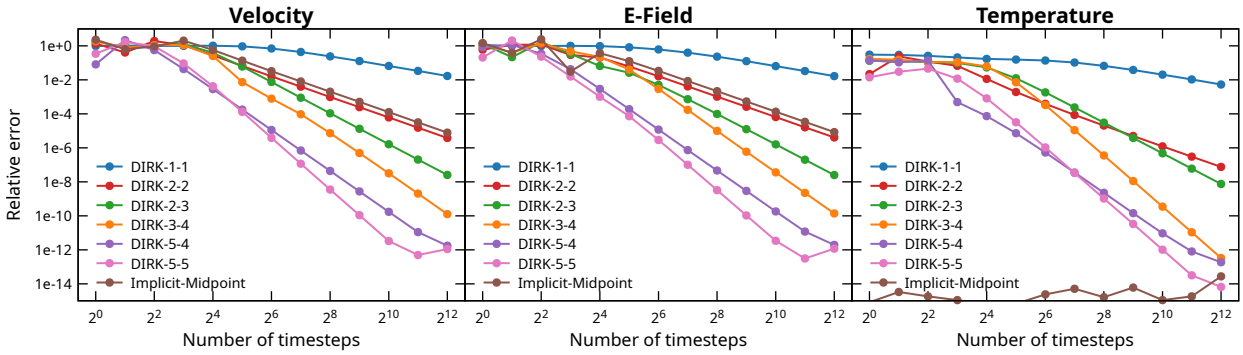

(C) Collisionless; Maxwell potential form; Implicit methods (Tempus).

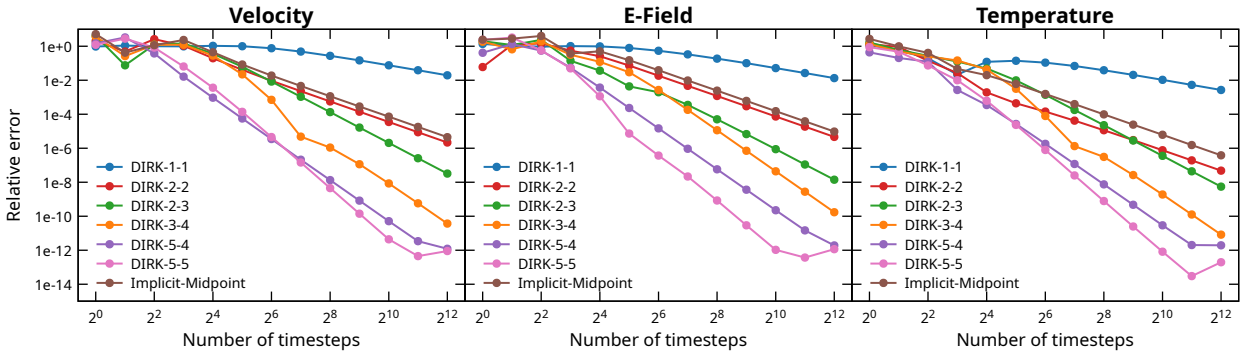

(D) Collisional ($\alpha_{e;i}$ = 1.0E+18); Maxwell potential form; Implicit methods (Tempus).

FIGURE 7.7. Convergence tests for collisionless and collisional two-fluid oscillation problems.

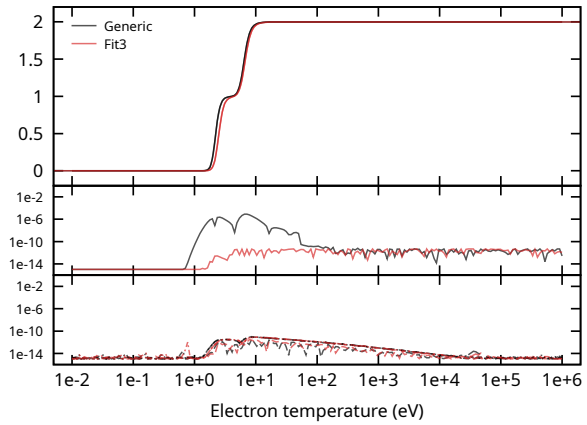

(A) He.

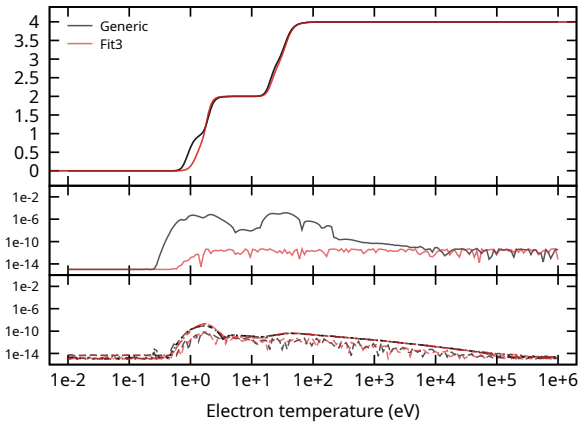

(B) Be.

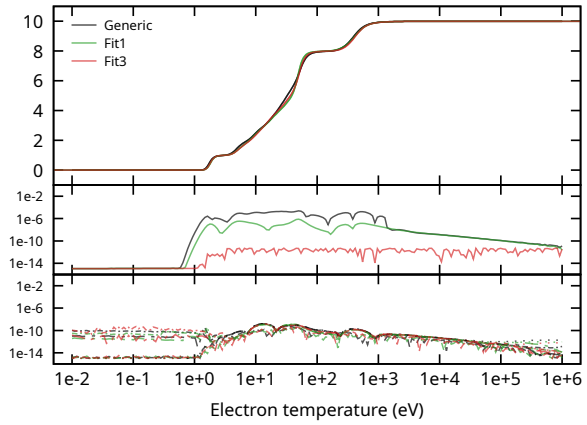

(C) Ne.

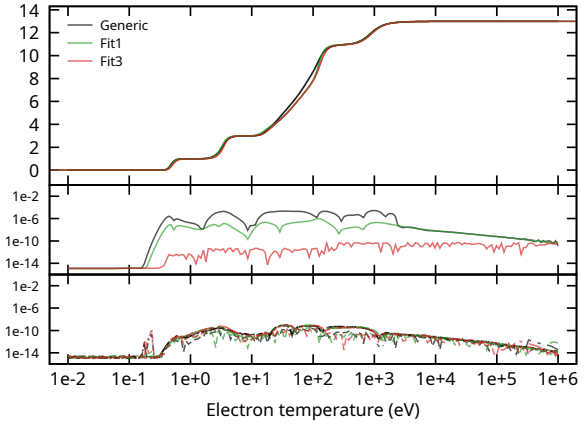

(D) Al.

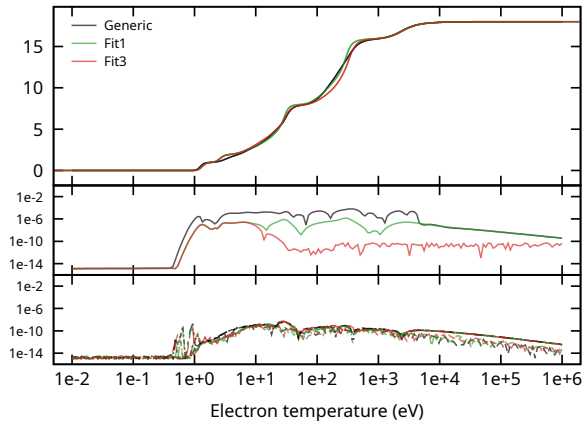

(E) Ar.

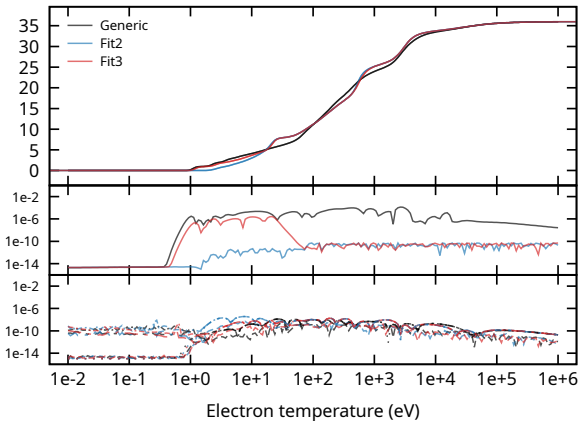

(F) Kr.

FIGURE 7.8. Comparison of equilibrium ionization fractions (top) computed directly (solid lines) or through time-evolution using the Drekar code (dashed lines). The various sources of ionization and recombination rates used for each case are summarized in table 2.1. Each plot shows the final average charge state (top), the absolute difference between the expected equilibrium values and the time-evolved values from Drekar (middle), and relative errors in the conservation of total mass and momentum in the system across all species (bottom). Note that the difference between the reference (solid lines) and Drekar results (dashed lines) is small enough that the two cases are indistinguishable in the top section of each subfigure.

δ	ω_{pi}	ω_{pe}	ω_{ci}	ω_{ce}	Ion Fluid Sod	Ion Fluid Brio-Wu	Electron Fluid Sod	Electron Fluid Brio-Wu
1.00E+0	6.28E−2	1.99E−3	5.02E+0	5.02E−3	2.84E−5	1.85E−5	1.68E−6	1.63E−6
1.00E−1	6.28E−3	1.99E−4	5.02E−1	5.02E−4	2.84E−5	1.85E−5	1.68E−6	1.63E−6
1.00E−2	6.28E−4	1.99E−5	5.02E−2	5.02E−5	2.84E−5	1.85E−5	1.68E−6	1.63E−6
1.00E−3	6.28E−5	1.99E−6	5.02E−3	5.02E−6	2.84E−5	1.85E−5	1.68E−6	1.63E−6
1.00E−4	6.28E−6	1.99E−7	5.02E−4	5.02E−7	2.84E−5	1.85E−5	1.68E−6	1.63E−6

FIGURE 7.9. Characteristic timescales associated with the hydrodynamics, plasma frequencies, and cyclotron frequencies of the electron and ion species for the two-fluid Sod and Brio-Wu problems with $\varepsilon = 10^{-3}$ and $\tau = 10^{-2}$. Fluid timescales are computed for the case of 20,000 mesh cells using representative values from the two-fluid initial conditions and the maximum velocities observed in highly-refined single-fluid simulations of each problem.

$t = 10^{-4}$ using the implicit Euler method. This final time is specifically chosen to be large enough that each configuration should reach a state that is close to the equilibrium ionization distribution by the end of the simulation. The results of the tests for a selection of species of interest over a broad range of temperatures are shown in fig. 7.8. The agreement between the expected equilibrium values and the time-evolved values is very good in each case.

7.3. Two-fluid Sod problem

We consider a two-fluid version of the single-fluid Sod problem [83]. The problem is defined over the spatial domain $x \in [0,1]$ and time interval $t \in [0,0.1]$. In the single-fluid case, the velocity is initially zero everywhere, and the initial density and pressure values are given by

$$\rho = \begin{cases} 1.0, & x < 0.5, \\ 0.125, & x > 0.5, \end{cases} \qquad p = \begin{cases} 1.0, & x < 0.5, \\ 0.1, & x > 0.5. \end{cases} \tag{159}$$

We employ a non-dimensional scaling of the two-fluid system similar to that used by [9] based on three scaling parameters: ε, τ, and δ. These parameters determine the values of the ion/electron mass ratio, vacuum permittivity, and unit charge magnitude in the nondimensional setting:

$$m_e = \frac{\varepsilon}{1+\varepsilon}, \qquad m_i = \frac{1}{1+\varepsilon}, \qquad \epsilon_0 = \tau^2, \qquad \mathrm{e} = |q_e| = \frac{1}{\delta}. \tag{160}$$

It is useful to note the asymptotic behavior of various plasma parameters relative to these scaling parameters for fixed density, temperature, magnetic field strength, etc. In the non-dimensional setting, the electron plasma frequency scales as $\omega_{pe} \sim (\tau\delta\sqrt{\varepsilon})^{-1}$, the electron and ion cyclotron frequencies scale as $\omega_{ce} \sim (\delta\sqrt{\varepsilon})^{-1}$ and $\omega_{ci} \sim \delta^{-1}$, respectively, and the Debye length scales as $\lambda_D \sim \tau\delta$. It can be observed from these values that the quasineutral ideal MHD limit is recovered as $\varepsilon, \tau, \delta \to 0$. Timescales associated with a range of specific cases considered for the two-fluid Sod (here) and Brio-Wu (section 7.4) problems are shown in fig. 7.9. All timescales are computed for the case of $\varepsilon = 10^{-3}$, $\tau = 10^{-2}$, and 20,000 mesh cells using representative values from the two-fluid initial conditions and the maximum velocities observed in highly-refined single-fluid simulations of each problem.

The decomposition of the initial conditions for the two-fluid case is done using a mass weighting for the initial densities of the species

$$\rho_i = m_i \rho, \qquad \rho_e = m_e \rho, \tag{161a}$$

and an equal weighting for the pressure of each species:

$$p_i = p_e = \frac{p}{2}. \tag{161b}$$

The values of other parameters in the nondimensional setting are given by $\mu_0 = 1$, $k_\mathrm{B} = 1$, and $c = (\epsilon_0\mu_0)^{-1/2}$.

We use the two-fluid Sod problem to explore issues relating to the AFC stabilization applied to the fluid equations. Two approaches are considered for stabilizing the multifluid system. The first approach, which we refer to as the

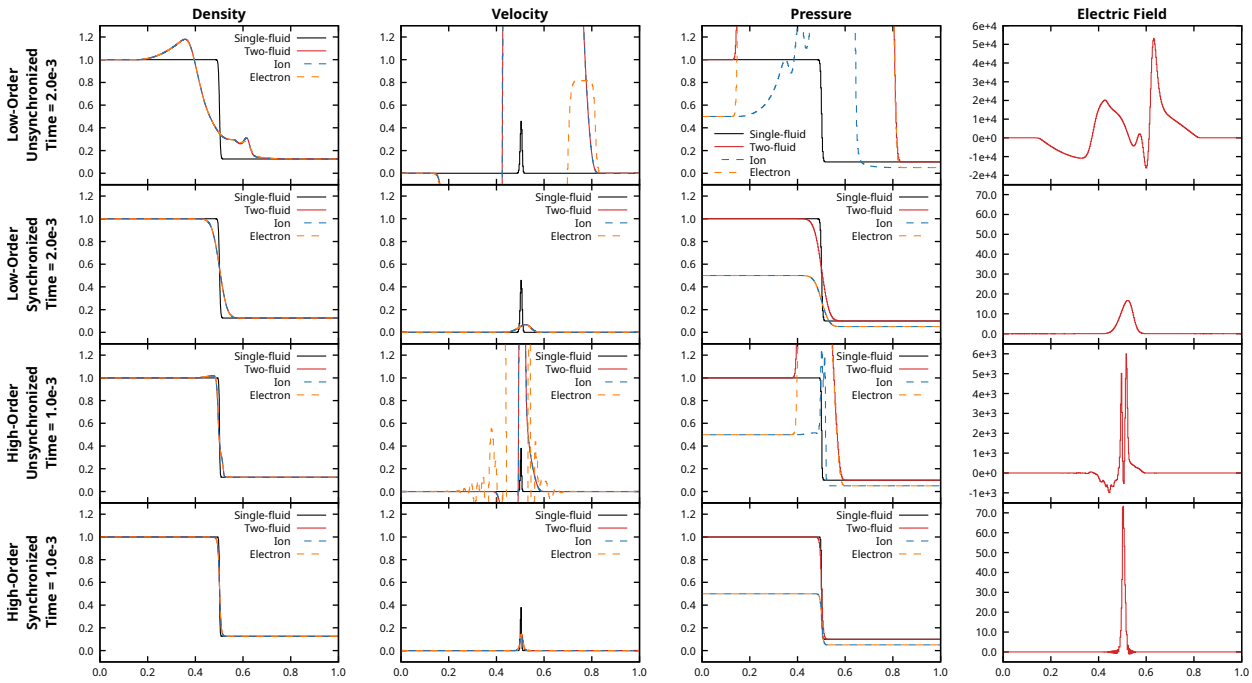

FIGURE 7.10. The effect of synchronizing the AFC stabilization between electrons and ions in the two-fluid Sod problem. In each case, 400 mesh cells are used with an electrostatic model, and the scaling parameters are set to $\varepsilon = 10^{-4}$, $\tau = 10^{-4}$, and $\delta = 1.0$. High-order methods use a value of $q = 2$ and $(\rho_s, p_s, \mathcal{E}_s)$ limiting for each species s.

unsynchronized approach, simply stabilizes the Euler subsystem for each fluid independently. Two fluids with different sound speeds will therefore receive different amounts of dissipation in this case. The second approach, which we refer to as the synchronized approach, applies equivalent stabilization to all fluids simultaneously. In this case, the dissipation applied to each species depends on the maximum sound speed across all species. Further, the same limiter parameter α is used for all species, again determined by the species that requires the most stabilization.

The impact of synchronizing the stabilization across the fluid species is shown in fig. 7.10 at early simulation times. In each case, 400 mesh cells and an electrostatic approximation are used, and the scaling parameters are set to $\varepsilon = 10^{-4}$, $\tau = 10^{-4}$, and $\delta = 1.0$. The high-order methods use a value of $q = 2$ and $(\rho_s, p_s, \mathcal{E}_s)$ limiting for each species s. In the unsynchronized cases, the system rapidly becomes unstable, and the profiles of the electron velocity and pressure both differ significantly from that of the ions and the single-fluid solution. When the stabilization applied to the fluids is synchronized, the electron and ion species remain coupled, as would be expected in this scaling limit, and the results agree well with the single-fluid solution (albeit with more dissipation than is observed in the single-fluid solution). These results indicate that synchronizing the fluid stabilization is a crucial component of the overall robustness of the implementation.

Additional comparisons for the two-fluid Sod problem using various electromagnetics formulations are shown in figs. 7.11 and 7.12 using mass ratios of $\varepsilon = 10^{-2}$ and $\varepsilon = 10^{-3}$, respectively, with $\tau = 10^{-2}$ and

$$\delta \in \{10^{-0}, 10^{-1}, 10^{-2}\}. \tag{162}$$

We run each test using an electrostatic model (ES), the curl form of Maxwell's equations using the eliminated parabolic divergence cleaning (Par) or the implicit projection approach (Proj), and the potential form of Maxwell's equations in both the purely hyperbolic form (Pot) or using the elliptic form equation for the scalar potential (E Pot). The cleaning parameter for the eliminated parabolic divergence cleaning formulation is set to $c_p = \sqrt{hc}$ in all cases, where h is a measure of the finite element mesh size. Each simulation uses a two-stage SDIRK scheme that is L-stable with second-order accuracy [3]. Timesteps are chosen based on the characteristic speed of the ion fluid with a CFL number of 1.2. The computational domain is extended beyond the original range of $x \in [0, 1]$

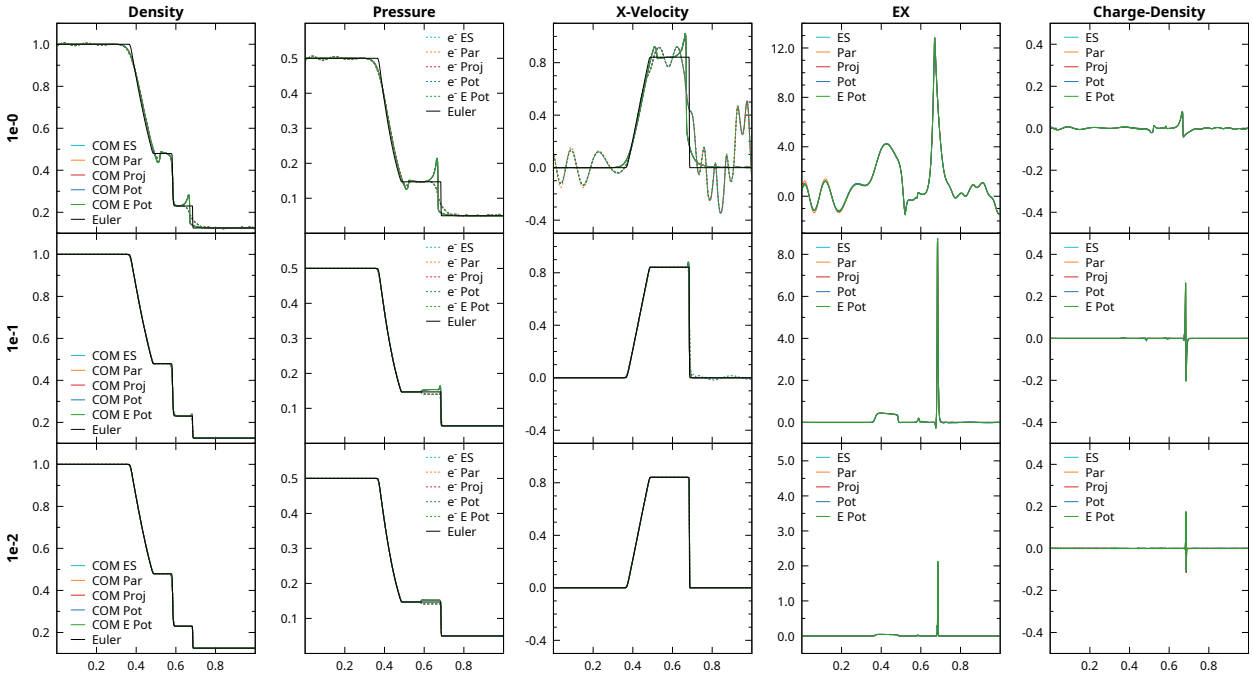

(A) 2,000 mesh cells.

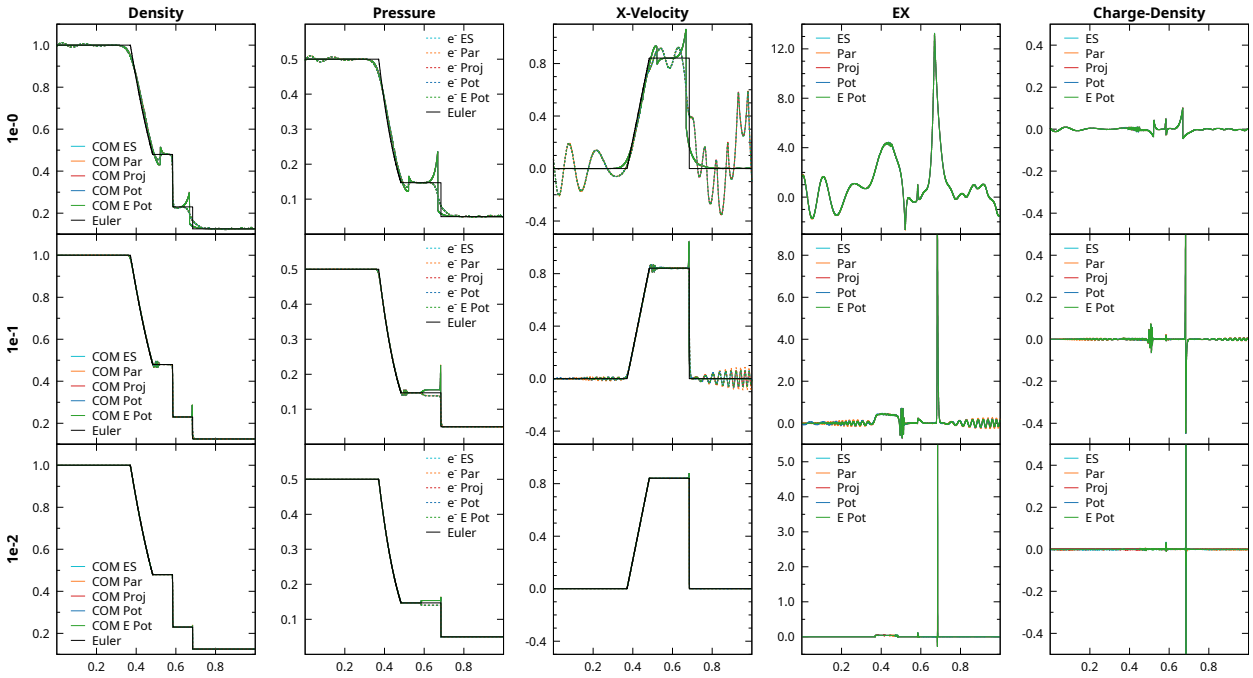

(B) 20,000 mesh cells.

FIGURE 7.11. Solutions of the two-fluid Sod problem for $\delta = 10^{-0}$, $\delta = 10^{-1}$, and $\delta = 10^{-2}$. All simulations use $\varepsilon = 10^{-2}$ and $\tau = 10^{-2}$. Solutions are shown for two mesh resolutions (coarse and fine). The pressure plot for the single-fluid solution (Euler) is scaled to one-half the pressure value from the simulation.

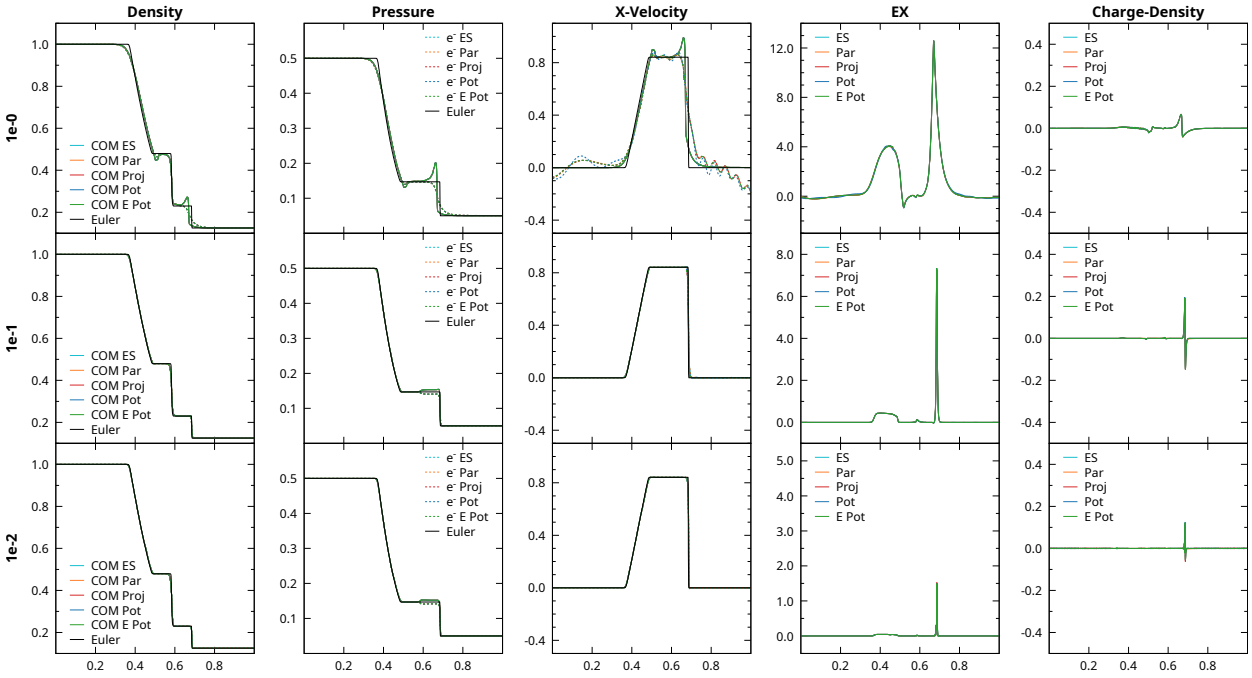

(A) 2,000 mesh cells.

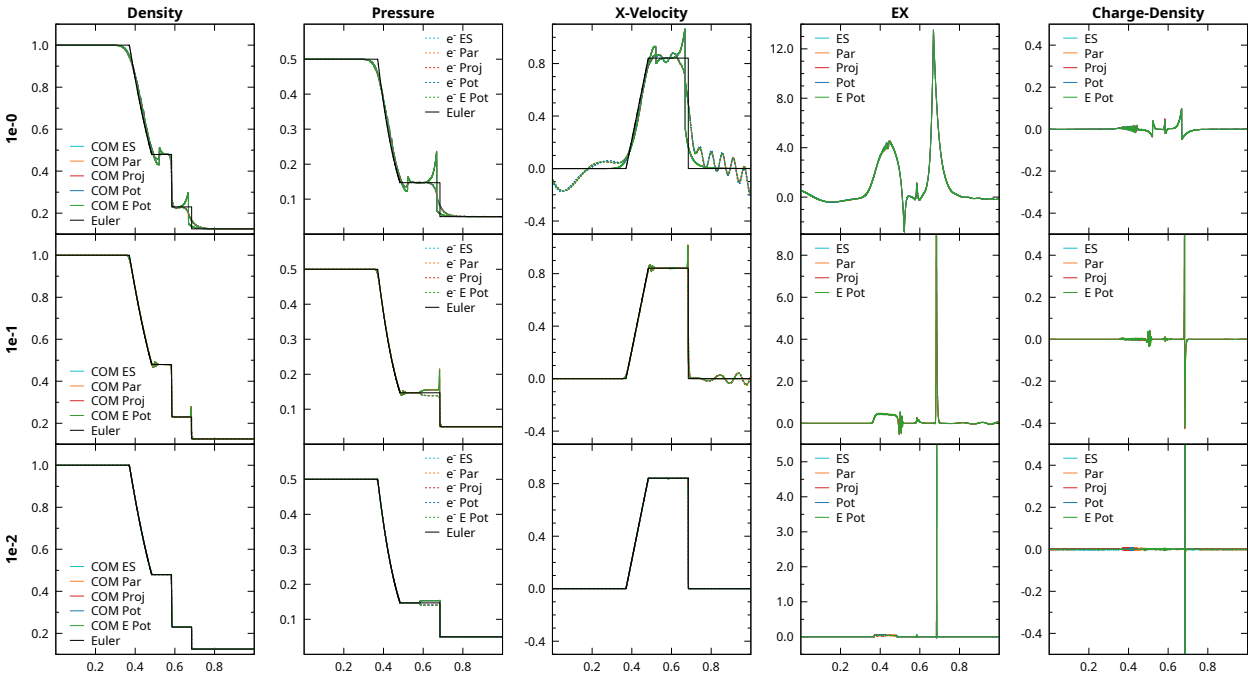

(B) 20,000 mesh cells.

FIGURE 7.12. Solutions of the two-fluid Sod problem for $\delta = 10^{-0}$, $\delta = 10^{-1}$, and $\delta = 10^{-2}$. All simulations use $\varepsilon = 10^{-3}$ and $\tau = 10^{-2}$. Solutions are shown for two mesh resolutions (coarse and fine). The pressure plot for the single-fluid solution (Euler) is scaled to one-half the pressure value from the simulation.

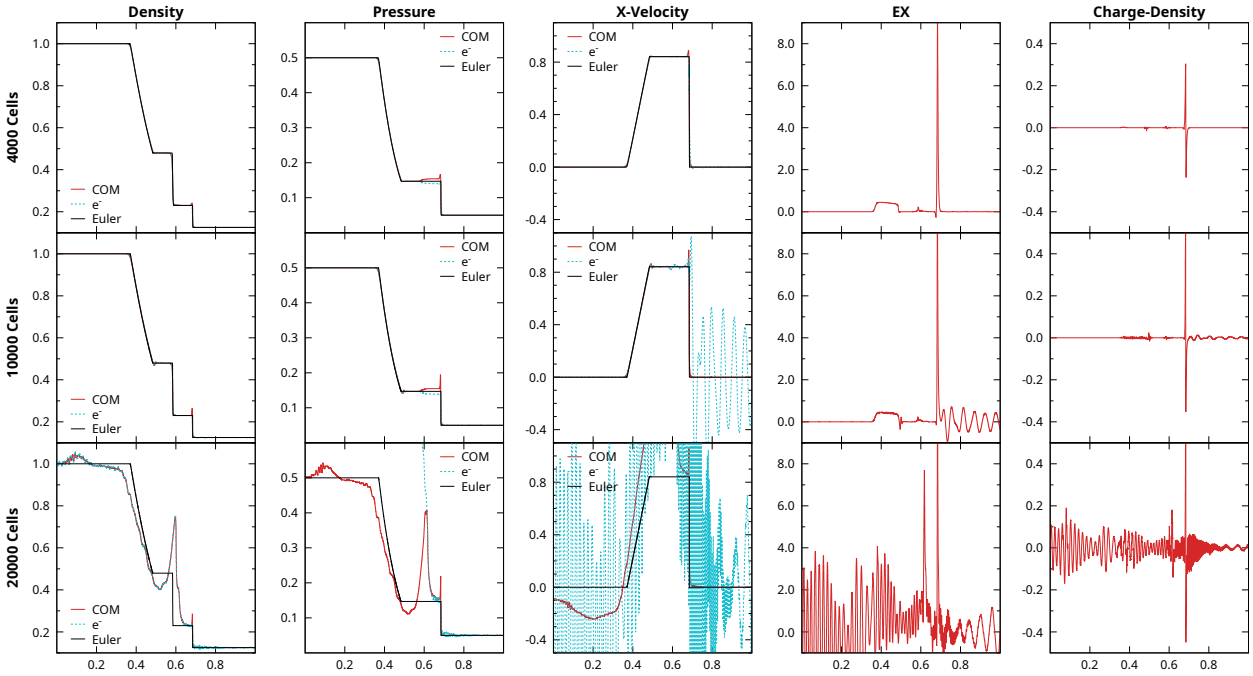

FIGURE 7.13. Solutions of the two-fluid Sod problem for $\varepsilon = 10^{-3}$, $\tau = 10^{-2}$, and $\delta = 10^{-1}$ using the purely hyperbolic potential formulation of Maxwell's equations for various mesh resolutions. Some solutions develop severe instabilities due to a failure of the method to properly control the gauge error and divergence error in the electric field.

in order to emulate the effects of outflow boundary conditions. Each figure also includes results for a simulation using a single-fluid Euler model with matching temporal and spatial discretizations.

In most instances, the results obtained show the expected behavior. When the value of δ is large, a much greater degree of charge separation exists between the electron and ion species, and dispersive waves propagating from the shock change the structure of the fluid expansion. Decreasing the value of δ increases the electrostatic coupling between the electrons and ions, pushing the two-fluid solution towards quasineutrality, and producing solutions that agree well with the single-fluid model.

A careful examination of fig. 7.12b shows that results using the purely hyperbolic potential formulation of Maxwell's equations (Pot) are absent from the middle row ($\delta = 10^{-1}$) of this figure. This is done because this method becomes unstable for this parameter setting ($\varepsilon = 10^{-3}$, $\tau = 10^{-2}$, $\delta = 10^{-1}$) as the mesh is refined. To prevent these results from obscuring the plots of the other formulations, we have plotted the solutions for this potential formulation by themselves in fig. 7.13 using three different mesh resolutions. The source of this instability seems to be associated with a lack of sufficient control over the divergence in the electric field.

For each electromagnetics formulation, we compute the norm of the error in the divergence involution for each field. The divergence error for the electric field is computed using an L^2 norm

$$\frac{1}{|\Omega|}\left(\int_{\Omega}\left|\epsilon_0 \nabla\cdot\mathbf{E} - q\right|^2 d\Omega\right)^{1/2} \tag{163}$$

scaled by the domain volume, and is plotted as a function of time in fig. 7.14 using various parameter scalings and mesh resolutions. In section 6.3 it was noted that the divergence error in the electric field for the potential formulation depends on the degree to which the computed potentials satisfy the gauge condition. We have also measured this gauge error (not shown), and found that its evolution closely tracks that of the divergence error in the electric field in cases where this instability occurs. It is worth noting that the authors in [36] did not observe any such instability when this formulation was used for Maxwell's equations coupled to a two-fluid model, though our numerical approach (continuous finite elements) differs from theirs (finite volumes). It is possible that the

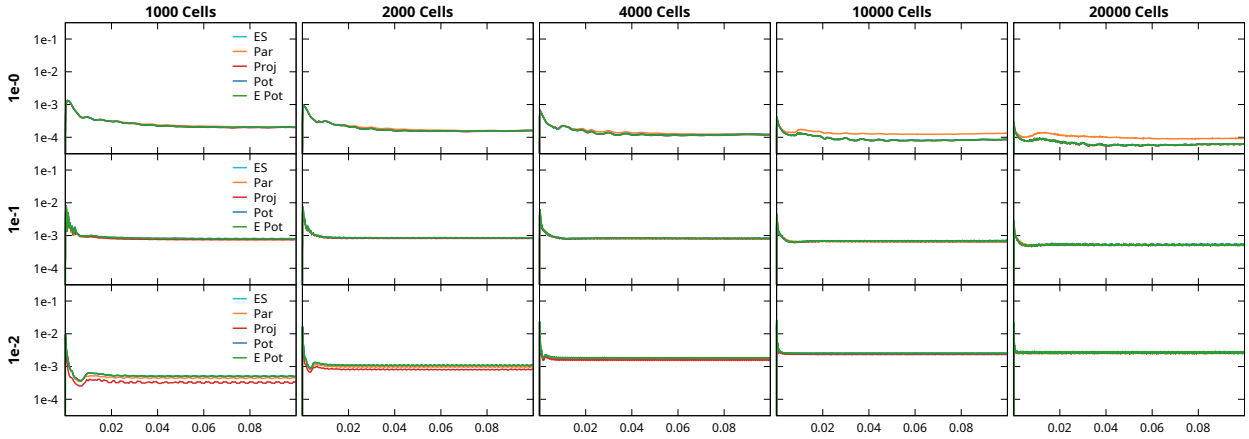

(A) Mass ratio $\varepsilon = 10^{-2}$.

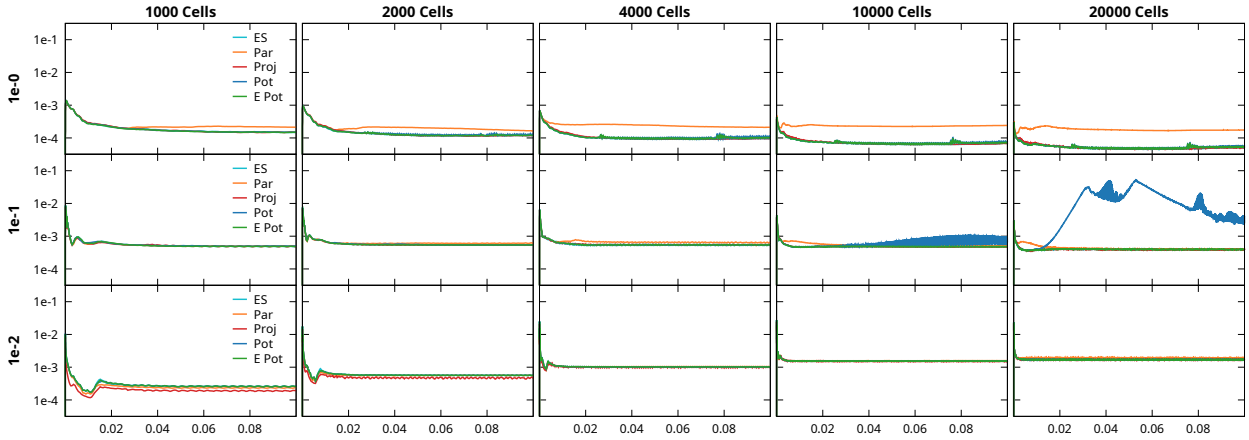

(B) Mass ratio $\varepsilon = 10^{-3}$.

FIGURE 7.14. Divergence errors in the electric field for the two-fluid Sod problem with $\delta = 10^{-0}$, $\delta = 10^{-1}$, and $\delta = 10^{-2}$. All simulations use $\tau = 10^{-2}$.

occurrence of this instability is associated with our particular finite element discretization, and that additional stabilization is required to ensure robustness in this scheme in all cases. However, we have not observed any such instabilities in any of the problems we have run when using the elliptic potential formulation, and hence it may be preferable to simply use that approach instead.

7.4. Two-fluid Brio-Wu problem

We consider a two-fluid version of the Brio-Wu electromagnetic shock problem [20]. This problem is a common test for two-fluid systems in a variety of limits: see [9, 36, 56] for some examples. The same non-dimensional scaling used for the two-fluid Sod problem is used here as well. The initial conditions for the fluids are the same as that of the two-fluid Sod problem described in section 7.3, and magnetic fields are added with the initial conditions

$$\mathbf{B} = \begin{cases} (0.75, +1.0, 0.0), & x < 0.5, \\ (0.75, -1.0, 0.0), & x > 0.5. \end{cases} \tag{164}$$

When using the potential form of Maxwell's equations, the y component of the magnetic field is specified through an appropriate initial condition on the vector potential $\mathbf{A}$. Since the x component of the magnetic field is constant in both space and time, we treat this component as an externally applied field separate from the vector potential $\mathbf{A}$.

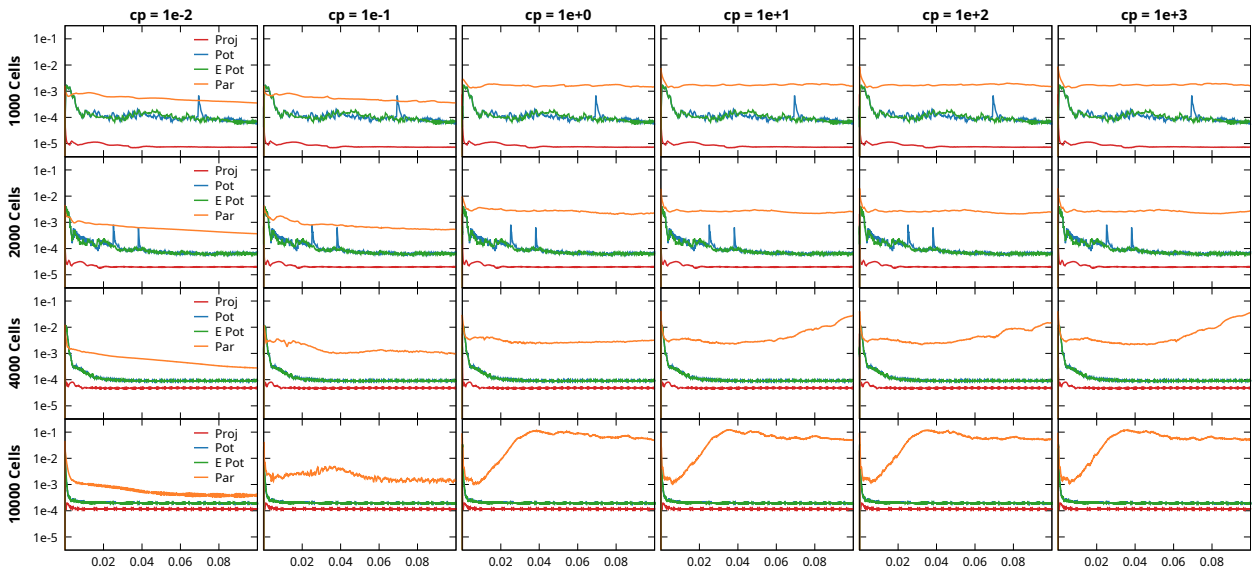

FIGURE 7.15. Norm of the electric field divergence error (163) versus simulation time for the two-fluid Brio-Wu problem under the scaling $\varepsilon = 10^{-3}$, $\tau = 10^{-2}$, $\delta = 10^{-4}$. Each column uses a different value for the parameter c_p used in the parabolic divergence cleaning for Maxwell's equations.

Thus, the magnetic field is given by

$$\mathbf{B} = \mathbf{B}_{\text{ext}} + \nabla \times \mathbf{A}, \tag{165a}$$

where

$$\mathbf{B}_{\text{ext}} = \begin{pmatrix} 0.75 \\ 0.0 \\ 0.0 \end{pmatrix}, \tag{165b}$$

and the initial condition for the vector potential is given by

$$\mathbf{A} = \begin{pmatrix} 0.0 \\ 0.0 \\ |x - 0.5| \end{pmatrix}. \tag{165c}$$

Each test is run using the same configuration that was used for the two-fluid Sod problem (time integration, extended domain size, etc.) using mass ratios of $\varepsilon = 10^{-2}$ and $\varepsilon = 10^{-3}$, respectively, with $\tau = 10^{-2}$ and

$$\delta \in \{10^{-2}, 10^{-3}, 10^{-4}\}. \tag{166}$$

Since the evolution of the magnetic field is an important component of this problem, the electrostatic model is not used, and comparisons are made to a single-fluid ideal MHD model with matching temporal and spatial discretizations, based on the implicit stabilization approach in [58].

Determining an effective value for the parabolic divergence cleaning parameter c_p proved to be more challenging for this problem than for the two-fluid Sod problem. Initially, we ran both problems using the value $c_p = \sqrt{0.18c}$ recommended in [30]. We found that this value generally worked reasonably well for the two-fluid Sod problem and for most of the cases considered for the two-fluid Brio-Wu problem. However, for the case of $\varepsilon = 10^{-3}$, $\tau = 10^{-2}$, $\delta = 10^{-4}$ applied to the two-fluid Brio-Wu problem, we found this value for c_p to work sufficiently well on coarser meshes, but the solutions became increasingly unstable as the mesh was refined. As a result, we ran a parameter sweep for the value of c_p using these scaling parameters on a range of meshes: The norm of the divergence error in the electric field as a function of time for a range of mesh sizes and values for c_p with these parameter settings is shown in fig. 7.15. The results suggest that the maximum effective value for c_p is roughly proportional to the mesh size h. Our subsequent choice of $c_p = \sqrt{hc}$ was motivated by this parameter sweep and the dimensional

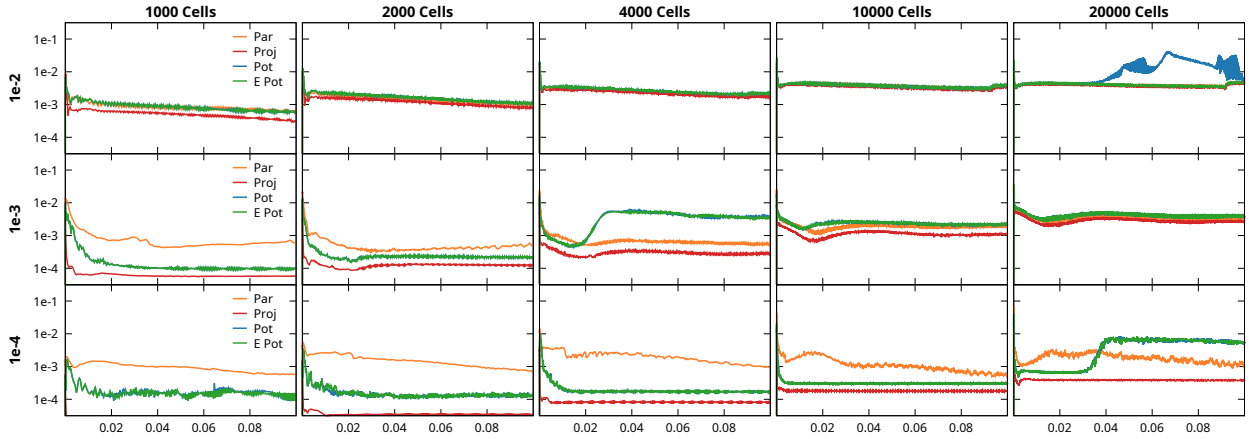

(A) Mass ratio $\varepsilon = 10^{-2}$.

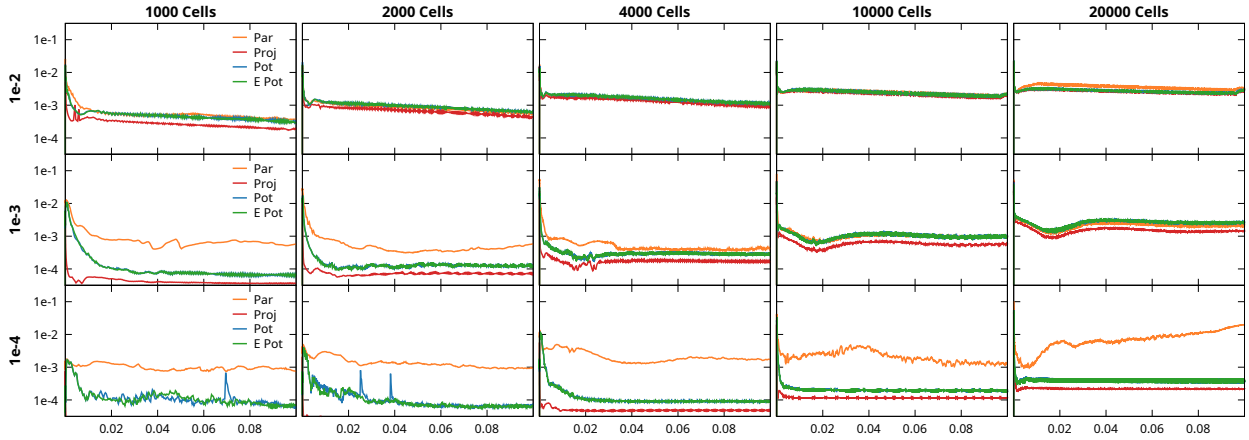

(B) Mass ratio $\varepsilon = 10^{-3}$.

FIGURE 7.16. Divergence errors in the electric field for the two-fluid Brio-Wu problem with $\delta = 10^{-2}$, $\delta = 10^{-3}$, and $\delta = 10^{-4}$. All simulations use $\tau = 10^{-2}$.

arguments in [27, 66]. All remaining results for the two-fluid Brio-Wu problem use this choice for c_p, which has thus far proven to be effective for all of the two-fluid Sod and Brio-Wu simulations we have considered.

Comparisons of solutions for the two-fluid Brio-Wu problem using various electromagnetics formulations are shown in figs. 7.17 and 7.18. In most instances, the results behave as expected. Dispersive waves propagating from the shock are present, with the frequency of the waves scaling as δ (and hence the cyclotron radii) varies. The structure of the solutions compares favorably with results published elsewhere, eg. [9, 36, 56], and the two-fluid solutions approach that of the ideal MHD model as δ decreases.

We note that the purely hyperbolic formulation of Maxwell's equations again became unstable in certain cases: specifically for $\varepsilon = 10^{-2}$, $\tau = 10^{-2}$, $\delta = 10^{-2}$ on finer meshes. These results are therefore not included in the first row of fig. 7.17b. This instability can be observed in the divergence errors plotted for each formulation in fig. 7.16. The divergence errors in other cases are generally satisfactory, though the increase in the divergence error later in time for the parabolic cleaning formulation in the case of $\varepsilon = 10^{-3}$, $\delta = 10^{-4}$ with 20,000 mesh cells is cause for some concern on the general applicability of the choice of $c_p = \sqrt{hc}$.

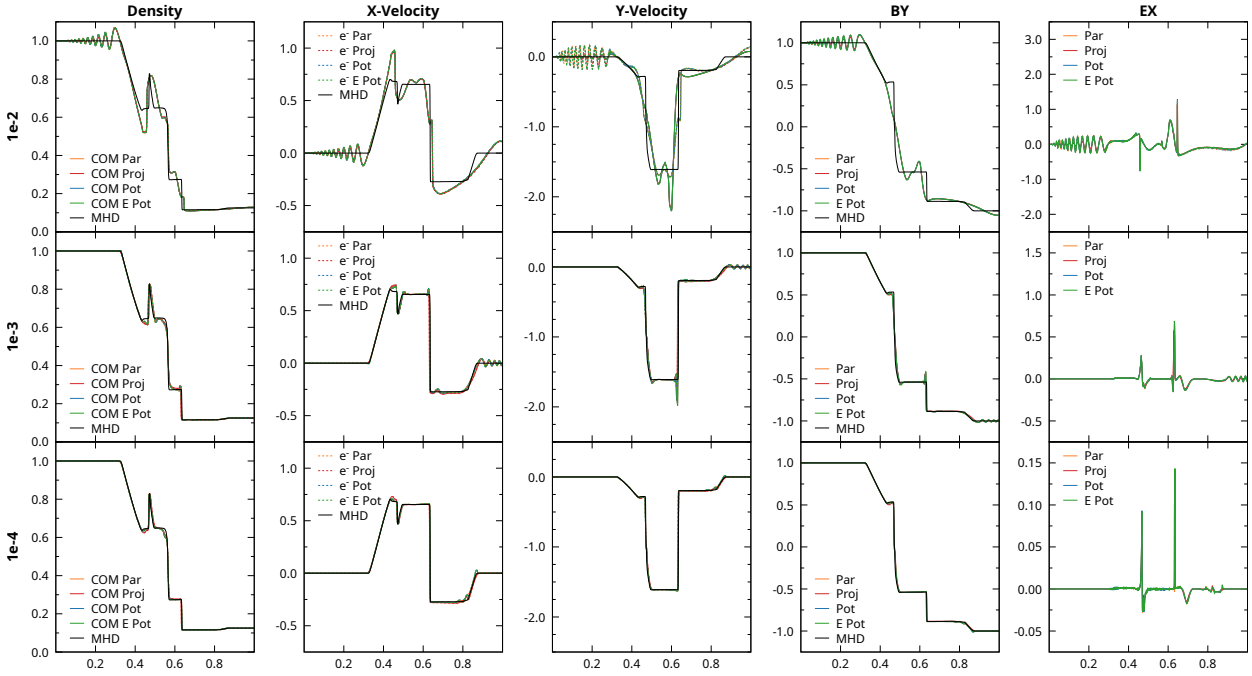

(A) 2,000 mesh cells.

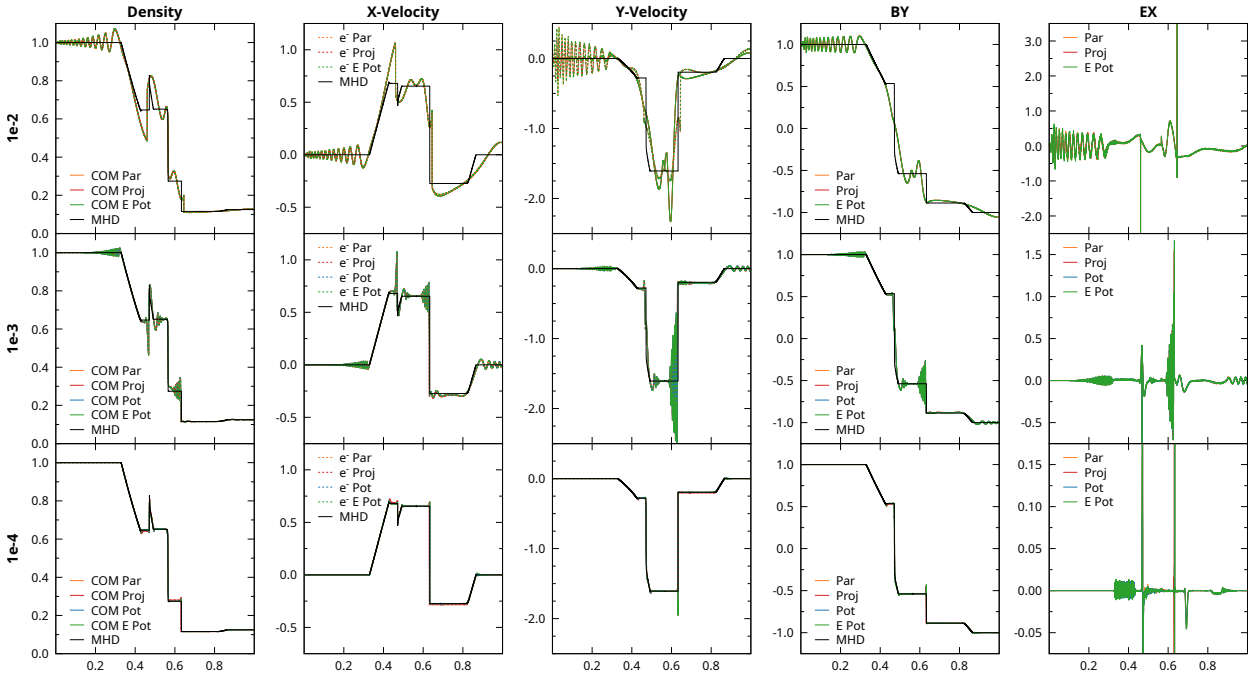

(B) 20,000 mesh cells.

FIGURE 7.17. Solutions of the two-fluid Brio-Wu problem for $\delta = 10^{-2}$, $\delta = 10^{-3}$, and $\delta = 10^{-4}$. All simulations use $\varepsilon = 10^{-2}$ and $\tau = 10^{-2}$. Solutions are shown for two mesh resolutions (coarse and fine).

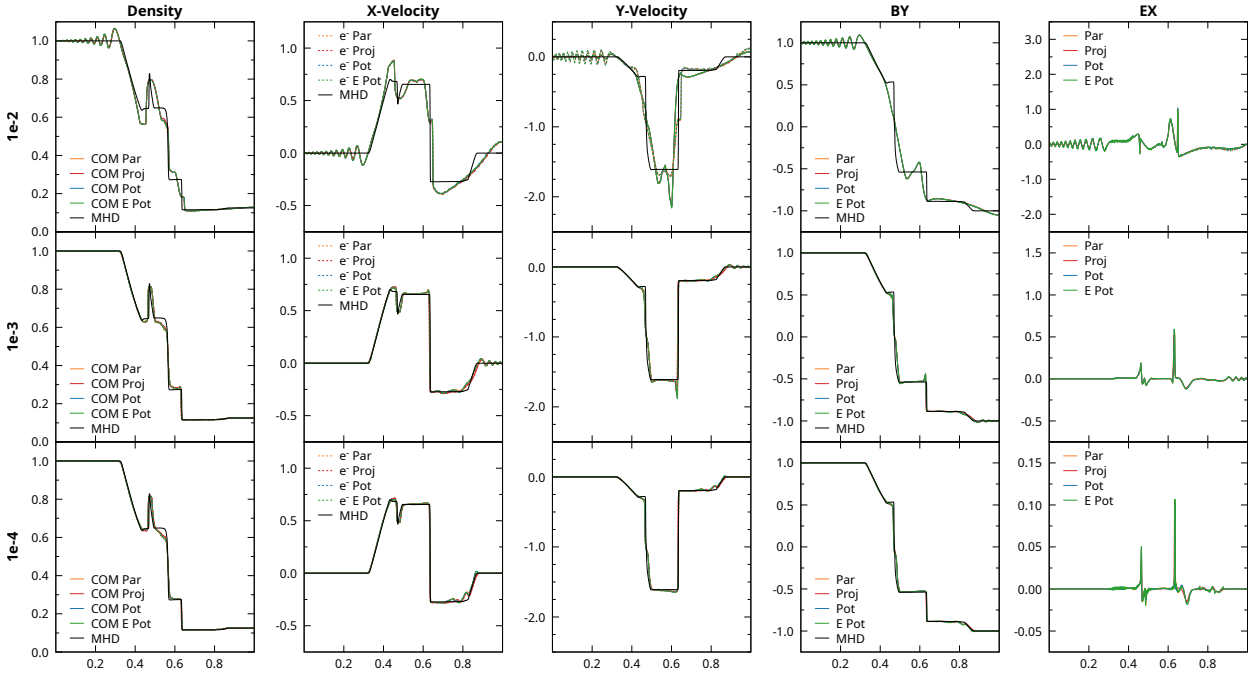

(A) 2,000 mesh cells.

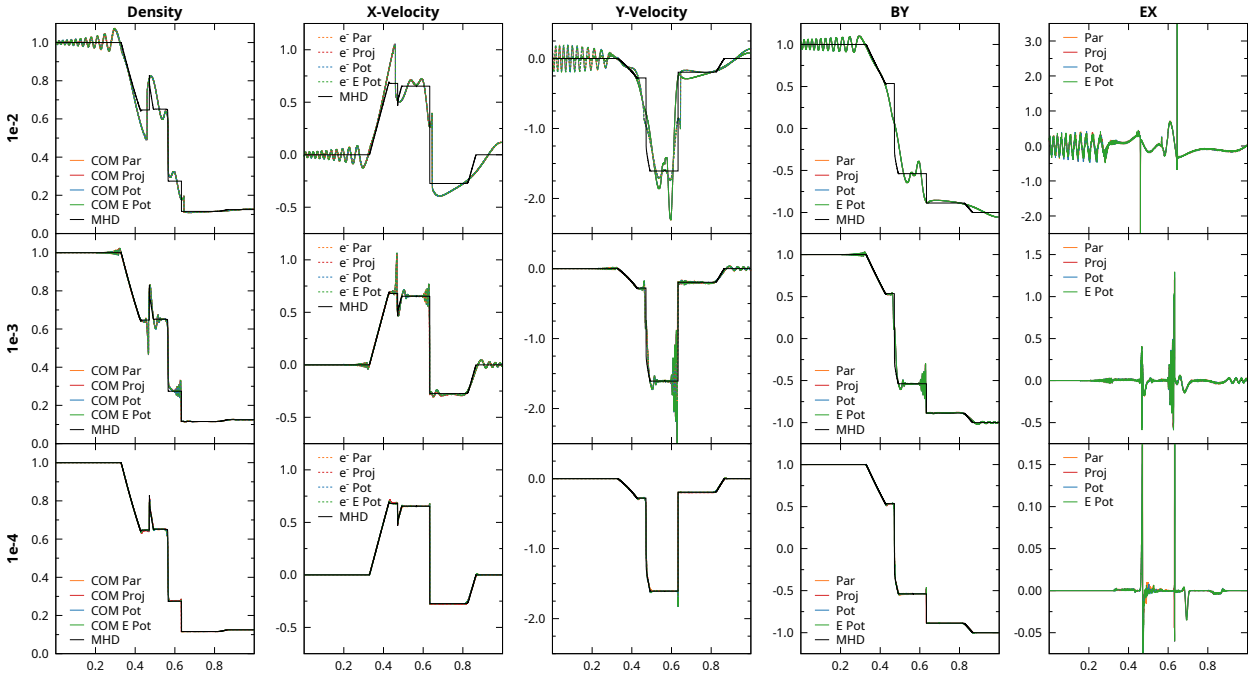

(B) 20,000 mesh cells.

FIGURE 7.18. Solutions of the two-fluid Brio-Wu problem for $\delta = 10^{-2}$, $\delta = 10^{-3}$, and $\delta = 10^{-4}$. All simulations use $\varepsilon = 10^{-3}$ and $\tau = 10^{-2}$. Solutions are shown for two mesh resolutions (coarse and fine).

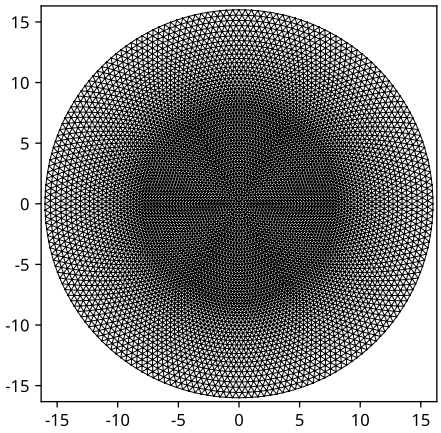

FIGURE 7.19. Diagram of the top surface of the initial coarse mesh for the cylindrical diocotron instability problem.

7.5. Two-dimensional diocotron instability

Diocotron instabilities [28], which are driven by velocity shear in non-neutral electron columns, have been studied experimentally and computationally in beam [44, 51] and cylindrical geometries [44, 73, 74]. We consider a configuration consisting of a cylindrical electron beam inside a uniform axial magnetic field. In this case, a rotational velocity is produced in the plasma column due to $\mathbf{E}\times\mathbf{B}$ forces exerted on the electron fluid. A sufficiently strong shear in this rotational velocity drives the development of the cylindrical diocotron instability. Because the development of the instability is dominated by $\mathbf{E}\times\mathbf{B}$ forces, the electric drift approximation is often used to reduce the particle velocity equation to that of a guiding center model, which removes the cyclotron motion of the particles. In the present context, such reductions to the momentum equation (5b) for the electron fluid are not considered, so that the cyclotron motion is retained in the model.

The problem is defined on a two-dimensional circular domain of radius $r_w = 16$ using the polar coordinates

$$(r,\theta) \in [0, r_w] \times [0, 2\pi]. \tag{167}$$

The nominal initial electron number density is given by

$$n_e^0(r) = \begin{cases} n_0\Delta, & r < r_b^-, \\ n_0, & r_b^- < r < r_b^+, \\ n_0\Delta_b, & r_b^+ < r < r_w, \end{cases} \tag{168}$$

where $n_0 = 1$ is the peak nominal electron number density, $\Delta = 0.1$ determines the jump in density between the outer shell and the inner core, and $\Delta_b = 10^{-4}$ determines the jump in density between the outer shell and the low-density background. The outer radius is taken to be $r_b^+ = 8$ and the inner radius of the shell is determined based on theoretical considerations which depend on the particular configuration that is used. A background of immobile ions with constant number density $n_i = n_0\Delta_b$ is used to ensure the initial charge density is zero for $r > r_b^+$.

The same non-dimensional scaling is used here as was used for the two-fluid Sod and Brio-Wu problems in the preceding sections. In this case, we fix $\varepsilon = 10^{-2}$, $\tau = 10^{-1}$, and $\delta = 1$. The initial electron density is seeded with a perturbation with azimuthal mode $\ell = 5$:

$$\rho_e = m_e n_e^0 \left(1 + \beta\cos(\ell\theta)\right), \tag{169}$$

where the magnitude of the perturbation is $\beta = 10^{-3}$. A constant axial magnetic field $B_z = 5$ orthogonal to the computational plane is assumed, and an electrostatic model is used to compute the evolution of the electric field. Since the diocotron instability is most commonly discussed in the context of a low-density regime, we assume a low-temperature, low-density limit in which the electron pressure is zero ($p_e = 0$). Accordingly, it is assumed that the sound speed used in the AFC stabilization is zero everywhere.

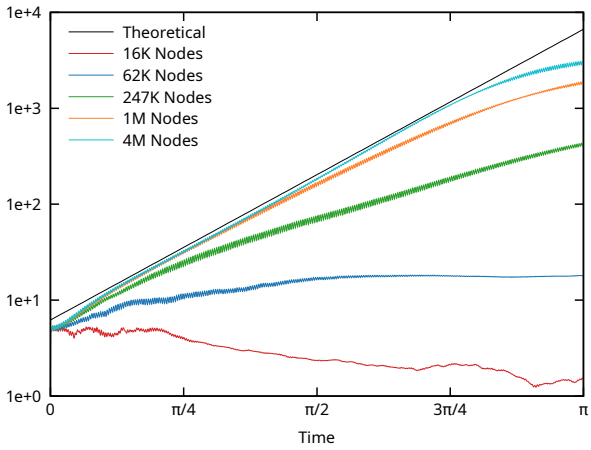

(A) Mode 5 amplitude.

Mesh	Rate	Error
16K nodes	−0.7338	2.96E+0
62K nodes	0.5376	1.68E+0
247K nodes	1.5881	6.34E−1
1M nodes	2.1307	9.12E−2
4M nodes	2.1790	4.29E−2
Theoretical	2.2218	

(B) Fit values for the growth rate.

FIGURE 7.20. Comparison of numerically computed growth rates in mode 5 for the cylindrical diocotron instability problem at different levels of mesh refinement. Mesh resolution is compared by counting the total number of nodes in the mesh at each level of refinement. All node counts are given as approximate values rounded to either thousands (K suffix) or millions of nodes (M suffix). Fit values for the growth rate are computed using a least-squares fit to an exponential function over the time interval $t \in [\pi/8, 3\pi/8]$.

The two-dimensional problem is solved using a three-dimensional tetrahedral mesh with one element of thickness in the z dimension. A diagram depicting the triangular mesh that lies on the circular faces of the computational domain is shown in fig. 7.19 for the coarsest mesh considered. Refined meshes are generated by recursively subdividing each triangle of the coarse mesh into three smaller triangles with vertices corresponding to the centroid of the coarse triangle and the midpoints of each edge. Periodic boundary conditions are used on the mesh faces orthogonal to the z axis, and the boundary conditions on the outer cylindrical boundary are taken to be $\phi = 0$ for the electrostatic potential and $\mathbf{u}_e = \mathbf{0}$ for the electron fluid. The electron fluid is initially at rest, but due to the relatively small mass of the electrons, the fluid quickly accelerates to a velocity profile determined by electromagnetic forces, regardless of the initial velocity profile that is used. For this problem, the limiter used for the AFC stabilization is computed based on the electron kinetic energy ($\rho_e \mathbf{u}_e^2/2$), with a value of $q = 2$.

The shape of the initial electron number density profile is chosen in accordance with the theoretical analysis in [29]. For the intended step-function density profile with $r_w = 2r_b^+ = 16$, the azimuthal mode 5 is unstable when $r_b^- = 6$ with a theoretical growth rate of $\omega \approx 2.2218$. The theoretical rate is compared to the amplitude of the azimuthal mode 5 in the numerical solution, which is computed by taking a discrete Fourier transform of the nodal values of the electrostatic potential at the radius $r = r_b^-$ and taking the norm of the coefficient corresponding to mode 5.

A comparison between numerically computed rates of growth in the solution and the theoretical rate is shown in fig. 7.20 for various levels of mesh refinement. Approximate values for the growth rate of the instability are computed as the exponent obtained from fitting an exponential function to the computed amplitude for azimuthal mode 5 over the time interval $t \in [\pi/8, 3\pi/8]$. The computed magnitudes qualitatively show convergence of the solutions to the rate predicted by the theoretical analysis in [29], though there is some low-frequency oscillation in the computed magnitudes (most apparent at later times) that causes the computed growth rates to deviate slightly from the theoretical rate. The exact cause of these deviations is unknown, but could be associated with nonlinear dynamics, the inclusion of the cyclotron motion in the electron fluid model (which is absent in the theoretical analysis in [29]), the use of a non-stationary electron fluid background in the outer region, the approach used to estimate the magnitude of the computed azimuthal mode, or simply due to the fact that the numerical solutions are not fully converged. The agreement between the computed growth rate and the theoretical value at fine mesh resolutions is nevertheless quite good, particularly at earlier times.

A selection of solution quantities at three simulation times are shown in fig. 7.21 for the most highly refined simu-

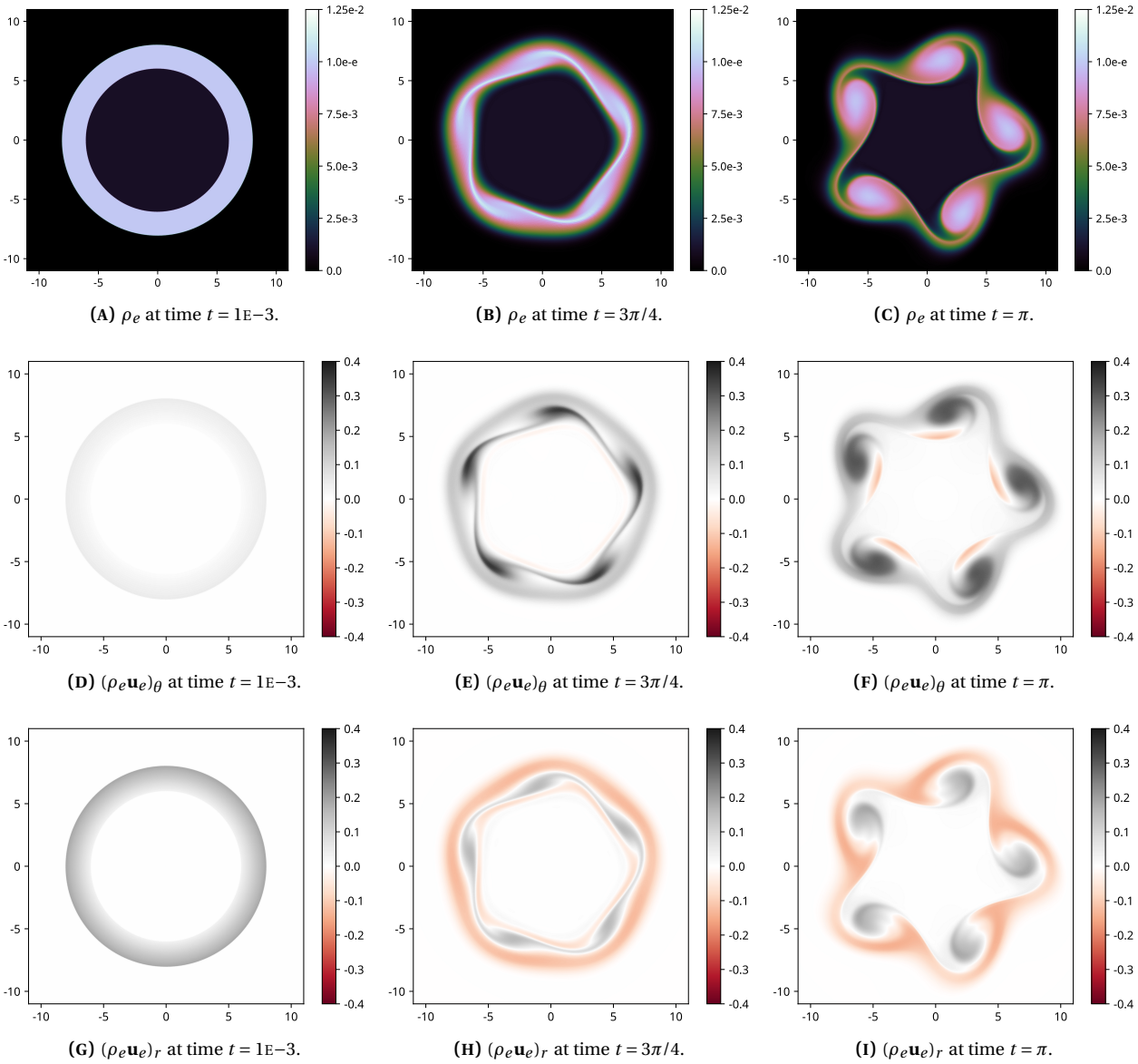

(A) ρ_e at time $t = 1\text{E}{-3}$. **(B)** ρ_e at time $t = 3\pi/4$. **(C)** ρ_e at time $t = \pi$.

(D) $(\rho_e \mathbf{u}_e)_\theta$ at time $t = 1\text{E}{-3}$. **(E)** $(\rho_e \mathbf{u}_e)_\theta$ at time $t = 3\pi/4$. **(F)** $(\rho_e \mathbf{u}_e)_\theta$ at time $t = \pi$.

(G) $(\rho_e \mathbf{u}_e)_r$ at time $t = 1\text{E}{-3}$. **(H)** $(\rho_e \mathbf{u}_e)_r$ at time $t = 3\pi/4$. **(I)** $(\rho_e \mathbf{u}_e)_r$ at time $t = \pi$.

FIGURE 7.21. Profiles of mass density and the polar components of momentum for the electron fluid at three times for the cylindrical diocotron instability problem. Each frame is taken from a simulation using a highly-refined tetrahedral mesh containing approximately 4 million nodes.

lation considered, which used a mesh containing approximately 4 million nodes. At each time, the electron mass density and the polar components of the electron momentum are shown. The polar components of the electron momentum are computed by projecting the momentum vector onto the unit vectors $\hat{\mathbf{r}}$ and $\hat{\boldsymbol{\theta}}$:

$$\big(\rho_e \mathbf{u}_e\big)_r = \rho_e \mathbf{u}_e \cdot \hat{\mathbf{r}}, \qquad \big(\rho_e \mathbf{u}_e\big)_\theta = \rho_e \mathbf{u}_e \cdot \hat{\boldsymbol{\theta}}, \tag{170}$$

where

$$\hat{\mathbf{r}} = \Big(\frac{x}{r}, \frac{x}{r}, 0\Big), \qquad \hat{\boldsymbol{\theta}} = \big(-\sin(\theta), \cos(\theta), 0\big), \tag{171}$$

are the unit vectors specifying the positive radial and azimuthal directions at each position, respectively. At time $1\text{E}{-3}$, the shear in the azimuthal velocity that drives the instability is evident. As the simulation progresses, the electron density begins to break up into a collection of vortices associated with the azimuthal pattern of the initial density perturbation.

7.6. Two-fluid GEM challenge

The GEM challenge problem [18] is a common example of a configuration in which electron dynamics play a crucial role in the evolution of the solution. In this problem, models beyond ideal or resistive MHD are required to adequately reproduce the rate of magnetic reconnection predicted by fully-kinetic multispecies models.

The problem is defined as follows. The species masses are given by $m_i = 25m_e = 1$, and the unit charge and magnetic permeability are both set to 1 ($|q_e| = \mu_0 = 1$). The speed of light is given a specified value, from which the permittivity is determined: $\epsilon_0^{-1} = \mu_0 c^2$. The problem is defined over the domain

$$\left[-\frac{L_x}{2}, \frac{L_x}{2}\right] \times \left[-\frac{L_y}{2}, \frac{L_y}{2}\right] \tag{172}$$

with $L_x = 25.6$ and $L_y = 12.8$. The initial number density of each species is given by

$$n_i = n_e = n_0\left(n_1 + \operatorname{sech}^2\left(y/\lambda\right)\right), \tag{173}$$

where $n_0 = 5n_1 = 1$ and λ determines the thickness of the current sheet. Each species uses an ideal gas equation of state with $\gamma = 5/3$ and $k_\mathrm{B} = 1$, and the fluids are initialized with uniform temperatures of

$$T_i = 5T_e = \frac{5B_0^2}{12\mu_0 n_0 k_\mathrm{B}} \tag{174}$$

where we take $B_0 = 1$. The ions are initially at rest, and the initial current is carried entirely by the electron species, with the initial electron momentum given by

$$\left(\rho_e \mathbf{u}_e\right)_z = \frac{m_e}{|q_e|}\frac{B_0}{\mu_0 \lambda}\operatorname{sech}^2\left(\frac{y}{\lambda}\right) \tag{175}$$

in the z direction, and zero in the x and y directions.

The electric field is initially zero, and the initial conditions for the components of the magnetic field are given by

$$B_x = B_0 \tanh\left(\frac{y}{\lambda}\right) - \frac{B_0 \delta \pi}{L_y}\cos\left(\frac{2\pi x}{L_x}\right)\sin\left(\frac{\pi y}{L_y}\right), \tag{176a}$$

$$B_y = \frac{B_0 \delta 2\pi}{L_x}\sin\left(\frac{2\pi x}{L_x}\right)\cos\left(\frac{\pi y}{L_y}\right), \tag{176b}$$

$$B_z = 0, \tag{176c}$$

where $\delta = 0.1$ is the magnitude of the perturbation with respect to the current sheet equilibrium. The initial conditions for the potential formulations of electromagnetics are $\phi = 0$, $\psi = 0$ for the scalar potential, and $\mathbf{C} = \mathbf{0}$, $A_x = A_y = 0$, and

$$A_z = \lambda B_0 \ln\left(\cosh\left(\frac{y}{\lambda}\right)\right) + B_0 \delta \cos\left(\frac{2\pi x}{L_x}\right)\cos\left(\frac{\pi y}{L_y}\right) \tag{177}$$

for the vector potential.

The boundary conditions at $x = \pm L_x/2$ are periodic. The boundary conditions at $y = \pm L_y/2$ are set such that fluid flow across the boundary and charge at the boundary are zero

$$\mathbf{u}_i \cdot \mathbf{n} = \mathbf{u}_e \cdot \mathbf{n} = 0 \qquad\qquad q = 0, \tag{178}$$

and the electromagnetic boundary conditions are set such that

$$\mathbf{B} \cdot \mathbf{n} = 0, \qquad \mathbf{E} \times \mathbf{n} = \mathbf{0}, \tag{179a}$$

$$\phi = \psi = 0, \qquad A_x = C_x = C_z = 0, \qquad A_z = \lambda B_0 \ln\left(\cosh\left(\frac{y}{\lambda}\right)\right), \tag{179b}$$

depending on the formulation.

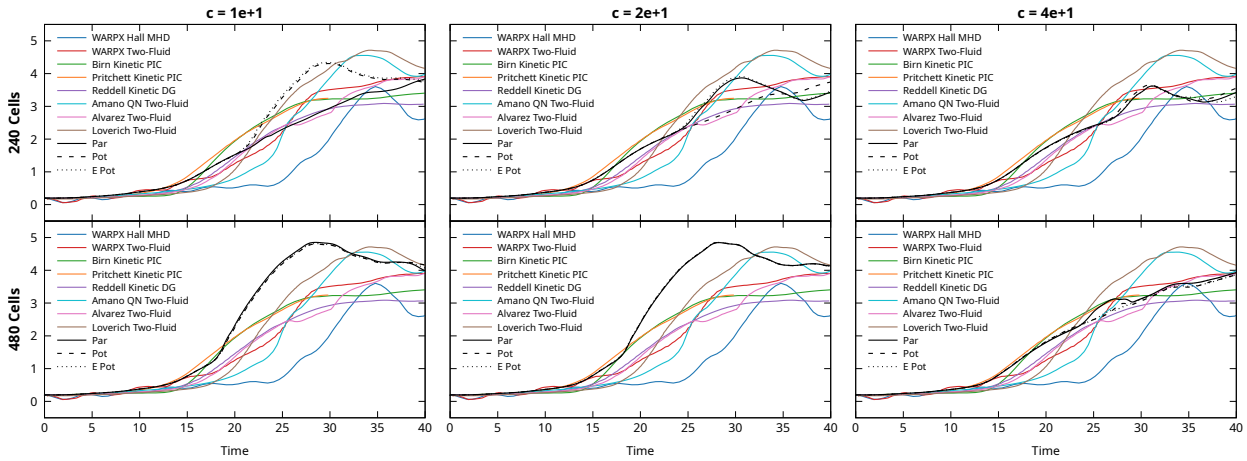

(A) $\lambda = 1/2$.

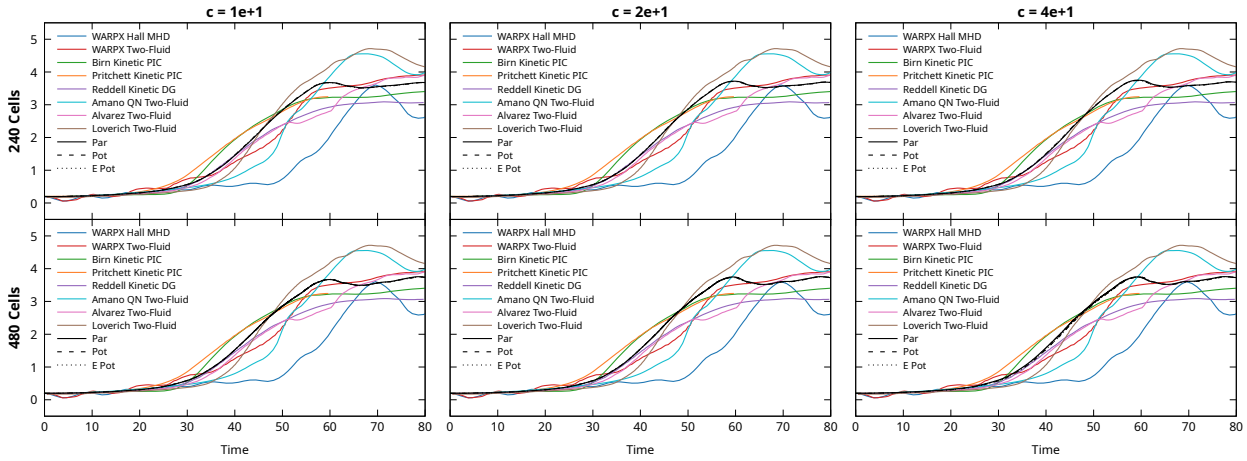

(B) $\lambda = 1$.

FIGURE 7.22. Magnetic reconnection measured by (180) as a function of time for simulations of the GEM challenge problem using different mesh resolutions (rows), and speed of light values (columns), and electromagnetics formulations (solid/dashed/dotted lines).

The standard approach for comparing results for this problem is by measuring the reconnected magnetic flux across the line $y = 0$

$$\Phi_B = \frac{1}{2B_0} \int_{-L_x/2}^{L_x/2} \left| B_y(x, y = 0) \right| \, dx \tag{180}$$

as a function of simulation time. We consider two cases: the first case takes the more common value of $\lambda = 1/2$, and the second uses $\lambda = 1$, which results in a thicker current sheet. The rate of magnetic reconnection is compared to the kinetic PIC results from Pritchett [76] and Birn [18], the continuum kinetic results from Reddell [77], the two-fluid and Hall MHD results from Srinivasan and Shumlak using the WARPX code [85], the two-fluid results from Alvarez Laguna [9] and Loverich [57], and the quasi-neutral two-fluid results from Amano [10]. For the case of $\lambda = 1$, the time values for data taken from external sources are scaled by a factor of 2 to account for the expected difference in the reconnection rate associated with the thicker current sheet. It should be noted that the results in [57] used a physical mass ratio between the electrons and ions instead of the more common value of $m_i/m_e = 25$ for this problem. Based on the results in [39, 82], this change in the mass ratio may be expected to delay the onset of reconnection by some amount.

A comparison of the reconnected flux for simulations using different mesh resolutions, speed of light values, and

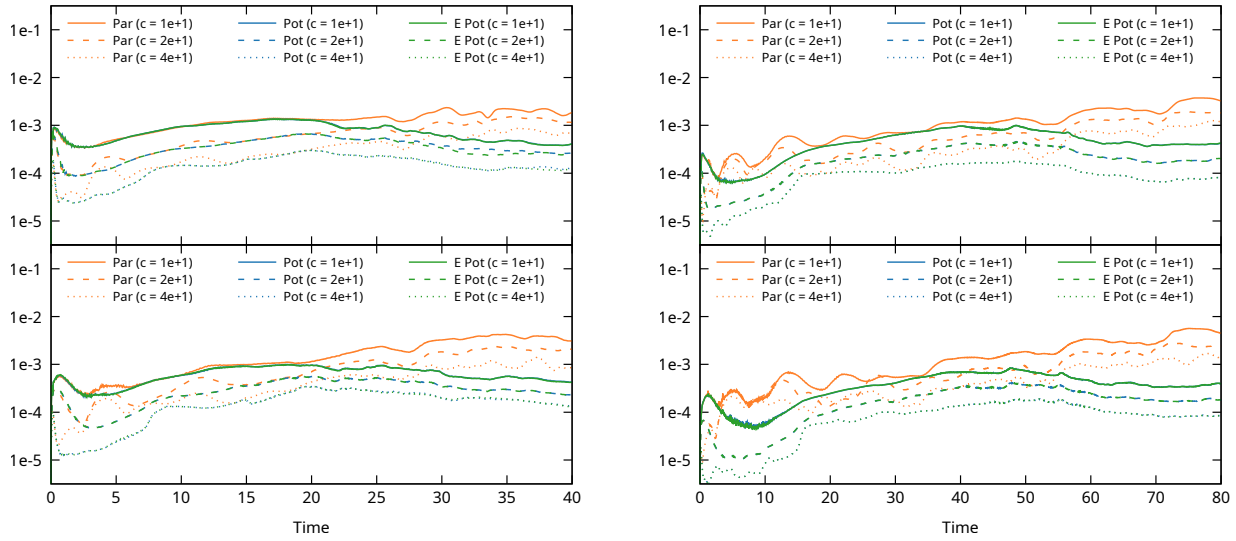

(A) $\lambda = 1/2$.

(B) $\lambda = 1$.

FIGURE 7.23. Divergence errors in the electric field for the GEM challenge problem as a function of simulation time.

electromagnetics formulations is shown in fig. 7.22. The number of mesh cells given in each case indicates the number of cells along the y dimension, with twice as many cells used along the x dimension to produce square cells. The size of each timestep in all simulations is selected based on the characteristic speed of the ion fluid only. We consider three electromagnetics formulations for this problem: The potential form of Maxwell's equations in both the purely hyperbolic form (Pot) or using the elliptic form equation for the scalar potential (E Pot), and the curl form of Maxwell's equations using the eliminated parabolic divergence cleaning approach with $c_p = \sqrt{hc}$ (Par). We were unable to run simulations of this problem using the implicit projection method for the curl form of Maxwell's equations, which we believe is due to the use of periodic boundary conditions at $x = \pm L_x/2$.

At early times, our results fall firmly within the range of values observed in published results. In some cases, we observe larger variations later in time depending on how the structure of the solution evolves. The formation of additional magnetic islands (plasmoids) near the central reconnection region tends to increase the peak magnitude of magnetic flux that is measured in the solution. It has been noted previously that the GEM challenge problem is subject to bifurcation [39, 56], and that increasing the thickness of the current sheet stabilizes the system and prevents the formation of additional magnetic islands. Our results clearly demonstrate this effect. For the case of the thinner current sheet ($\lambda = 1/2$) the existence, shape, and evolution of any additional magnetic islands in the solutions changes depending on the problem configuration (eg., mesh resolution, speed of light, etc.). In contrast, no additional magnetic islands form in any of the solutions computed for the thicker current sheet case ($\lambda = 1$), and the resulting magnetic reconnection rates are very consistent regardless of the specific problem configuration.

Many of our simulations using the finer mesh resolution (480×960 cells) form a larger, relatively stable magnetic island in the center of the computational domain that slowly drifts to either side. This behavior (and the formation of additional magnetic islands in general) has been a matter of some discussion in the literature. Many codes report an absence of magnetic islands in their solutions [11, 15, 37, 67, 77, 79, 94], and some codes report that their results contain a large central magnetic island [93]. Others report that the formation of a large central magnetic island varies from case to case, depending on the fluid model that is used (eg., five- versus ten-moment fluid model [57]), the inclusion of resistivity [10], the use of different numerical limiters [9], divergence correction techniques [85], mesh resolutions [69], or methods of different orders [56]. Mesh refinement studies conducted in [69] using a ten-moment multifluid model found that a larger, relatively stable magnetic island was observed in simulations above a certain mesh resolution, but not in simulations using coarser meshes. Since most references within the literature restrict their discussion of this problem to only one or a few computational configurations that may or may not be well converged, questions remain about the structure and formation of magnetic islands in this problem.

An additional observation is that the formation of a large central magnetic island in our results seems to be corre-

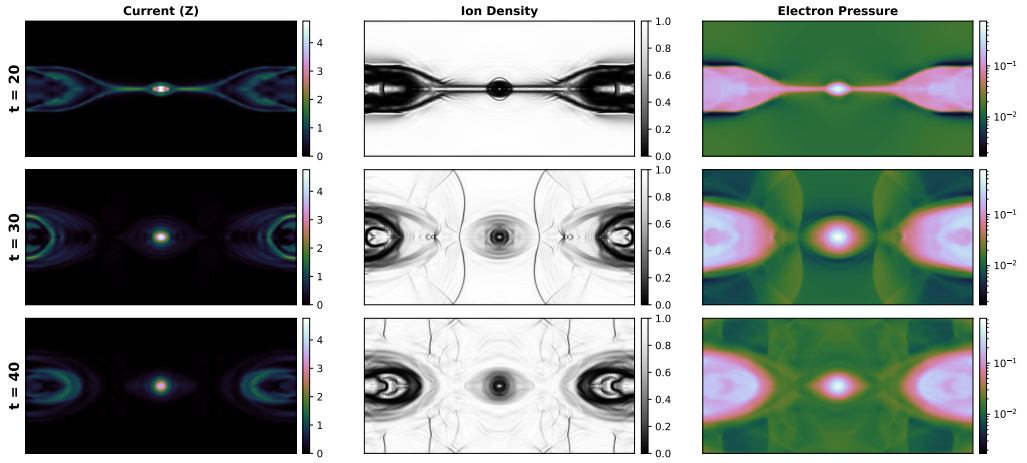

(A) $\lambda = 1/2$, $c = 20$.

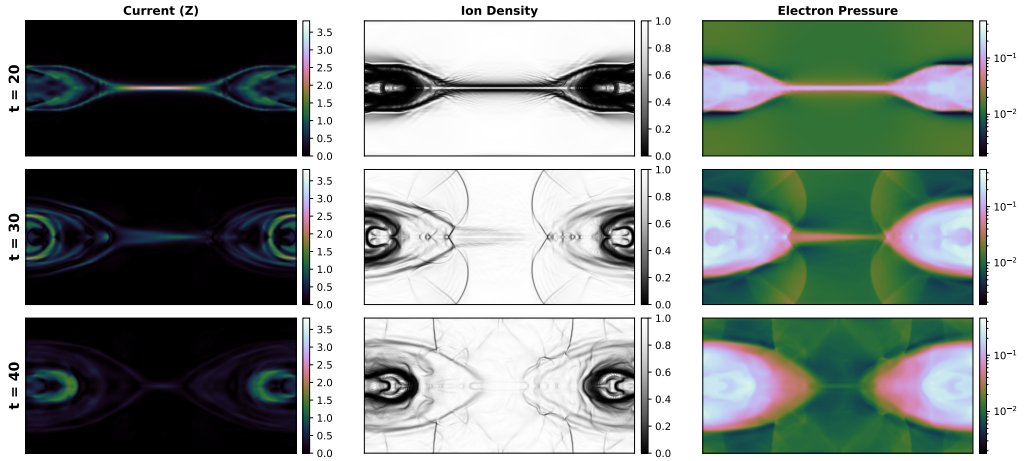

(B) $\lambda = 1/2$, $c = 40$.

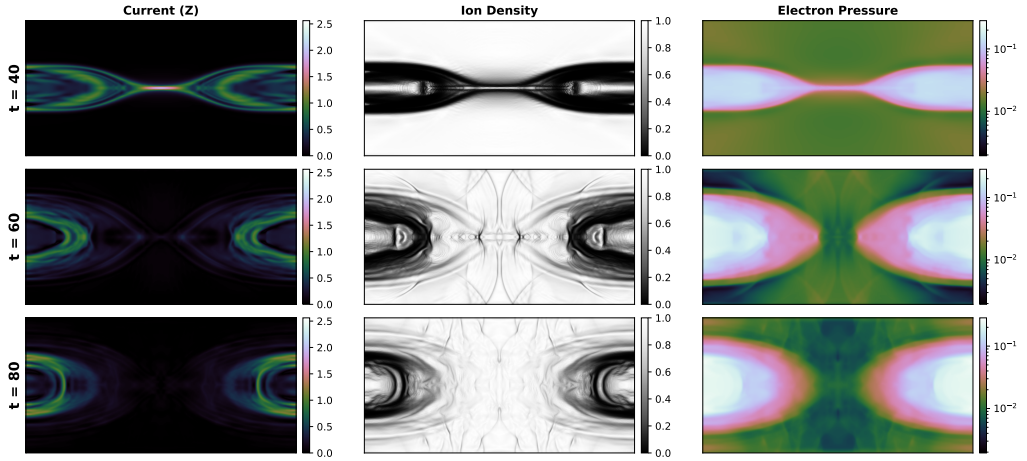

(C) $\lambda = 1$, $c = 20$.

FIGURE 7.24. Plots of the z component of current, simulated Schlieren images of ion density, and electron pressure for the two-dimensional GEM challenge problem using different configurations at different points in time. Each simulation was conducted using a spatial mesh of 960×480 cells, and the elliptic potential formulation of Maxwell's equations.

lated with whether or not the timestep size is small enough to resolve the electron plasma frequency. The configuration used for this problem is such that the electron plasma frequency scales proportionally to the value that is used for the speed of light. Thus, smaller timestep sizes are required to resolve the electron plasma oscillation as the the speed of light increases. In general, the simulations in which we observe the formation of a large central magnetic island correspond to cases where the electron plasma frequency is better resolved by the timestep size that is used. This behavior appears similar to that observed in the mesh refinement studies of [69], in the sense that the formation of a large central magnetic island is associated with finer mesh resolutions that better resolve smaller-scale behavior.

As stated previously, the formation of a large magnetic island at the center of the computational domain is associated with an increase in the peak magnitude of the magnetic flux that is measured in the solution, which is expected based on the results reported for other codes. Our results show that this behavior also tends to be associated with the reconnection process occurring at an earlier time than is reported by other codes. It is not fully clear why this is the case. However, given the bifurcation behavior present in the thin current sheet case ($\lambda = 1/2$) and the wide range of results reported in the literature, we believe these results are nevertheless reasonable.

Divergence errors in the electric field are shown in fig. 7.23 for different configurations. The divergence errors for the results shown are adequately controlled regardless of the electromagnetics formulation that is used. However, we have run additional simulations (results not shown) in which the size of each timestep is selected based on the characteristic speeds of both the electron and ion fluids. This approach typically results in timesteps that are approximately five times smaller than would be the case if only the ion fluid is considered, due to the faster electron sound speed. Some simulations did develop moderate instabilities when the purely hyperbolic potential formulation was used with these smaller timesteps. These moderate instabilities tended to produce more oscillatory solutions than would otherwise be expected, but did not blow up or cause the simulation to crash before the final simulation time was reached.

A selection of plots showing the structure of the solutions of two simulations are shown in fig. 7.24. In fig. 7.24a, a large magnetic island forms in the center of the computational domain, and remains stationary throughout the duration of the simulation. For the case in fig. 7.24b, a very small magnetic island forms towards the left of the domain and merges with the larger island towards the left, producing some small asymmetrical structures in the solution. In the thicker current sheet case shown in fig. 7.24c, no additional magnetic islands form in the solution, and very good symmetry is maintained.

8. EXEMPLAR PROBLEMS

8.1. Gas Puff

A one-dimensional simplified prototype of a gas puff configuration from Sandia's Z-machine is used as a demonstration to exercise the full range of capabilities associated with the general multifluid model. This is done on a quasi-one-dimensional Cartesian domain for $x \in [-0.25, 0.25]$ (in units of meters) using a mesh with one cell in the y and z dimensions and periodic boundary conditions along those axes. The geometric configuration is based primarily on the description in [40], though we consider an argon gas puff in this case.

The shape of the initial mass density of the argon gas was determined by visually fitting two Gaussian profiles to [40, Figure 1(b)]. The result is

$$\rho_0(x) = n_0 a_1 \exp\left(-\frac{(x-b_1)^2}{2c_1^2}\right) + n_0 a_2 \exp\left(-\frac{(x-b_2)^2}{2c_2^2}\right), \tag{181a}$$

given in units of kg/m^3, where $n_0 = 10^{24}$ and

$$a_1 = 1.1, \qquad b_1 = 0.011, \qquad c_1 = 0.006, \tag{181b}$$

$$a_2 = 0.35, \qquad b_2 = 0.034, \qquad c_2 = 0.004. \tag{181c}$$

Although gas puff experiments on Sandia's Z-machine have not at this point applied a pre-ionization stage to the gas, we assume an initial ionized fraction of 10^{-5} in the first charge state to enable the generation of axial current

Ref.	Shot	Type	Gap (m)	Volt. (V)	Load (MA)	MITL (MA)	t_{rise} (ns)	$E_{\max}$
[91]	Z1590	Ar puff	3.2E-2	5.5E+6	13.5	18	100	1.7E+8
[91]	AASC 22:30:250	Ar puff	2.5E-2	8.0E+6	18	23.5	100	3.2E+8
[90]	Z2381 (AASC)	Ar puff	2.5E-2		13		107	
[90, 92]	Z2559-61 (AASC)	Ar puff	2.5E-2	9.0E+6	16	26	120	3.6E+8
[89]	Z2603	Ar, Xe, Kr puff			14	25	120	
[89]	Z2605	Ar, Kr puff			16	25	120	
[41]	Z1098	W Wire	1.0E-2	1.25E+6	17	21	100	1.3E+8

TABLE 8.1. Summary of electromagnetic quantities (measured or simulated) for pinches on Sandia's Z-Machine.

and initiation of further ionization in the simulation.[3] The initial mass densities of Ar^0 and Ar^+ are therefore given by

$$\rho_{(\text{Ar},0)}(x) = \left(1 - 10^{-5}\right)\rho_0(x) \qquad \text{and} \qquad \rho_{(\text{Ar},1)}(x) = 10^{-5}\rho_0(x), \tag{182}$$

respectively. All other charge states are set to a density floor 10 orders of magnitude below the peak mass density; that is, $n_{(\text{Ar},k)}(x) = 10^{14}$ for $k \geq 2$. The initial number density of electrons is set such that the system exists in a quasi-neutral state at the initial time. All fluids are initially at rest with a temperature of 8,000 degrees Kelvin, which is the temperature at which the steady state ionization equilibrium of our ionization and recombination models yields a value of $\overline{Z} \approx 10^{-5}$. An ideal gas equation of state with $\gamma = 5/3$ is used for each fluid.

The problem is driven by specifying a time-dependent Dirichlet condition for E_z at both the left and right boundaries:

$$E_z(t) = E_{\max} \sin^2\left(\frac{\pi}{2}\frac{t}{t_{\text{rise}}}\right), \tag{183}$$

where $E_{\max}$ is the maximum electric field value and t_{rise} is the time at which the peak electric field value is attained. Given a gap size h_{gap} and maximum voltage $V_{\max}$, the maximum electric field magnitude is computed as

$$E_{\max} = \frac{V_{\max}}{h_{\text{gap}}}. \tag{184}$$

Measurements of the voltage generated in the post-hole convolute of Sandia's Z-machine show peak values in the range of 2.5 to 3 MV [98]. For a gap size of 2.5 cm (as informed by [40]), this result suggests $E_{\max}$ values in the range of 1E+8 to 1.2E+8. Additional references are shown in table 8.1 for comparison, which generally imply similar values. Since we consider a one-dimensional Cartesian geometry (instead of a one-dimensional cylindrical geometry) the geometric effect on the compressive field strength is absent. We therefore artificially increase the magnitude of the electric field condition at the boundary to a value of $E_{\max} = 5\text{E}{+}9$ to ensure that reasonably strong compression occurs, and set the rise time to $t_{\text{rise}} = 2.24\text{E}{-}7$.

The simulation is run using the purely hyperbolic potential form of Maxwell's equations. In this case, the corresponding conditions on the vector potential and it's derivative are

$$A_z = -\frac{E_{\max}}{2}\left(t + \frac{1}{\pi t_{\text{rise}}}\sin\left(-\pi t_{\text{rise}} t\right)\right), \tag{185a}$$

$$C_z = -\frac{E_{\max}}{c}\sin\left(-\frac{\pi}{2}\frac{t}{t_{\text{rise}}}\right). \tag{185b}$$

The computational mesh consists of 10,000 uniform elements along the x dimension, and a maximum charge state of 8 is used to limit computational cost. The AFC stabilization is applied with limiters computed using the density ρ_s and pressure p_s of each fluid, as well as $\|\mathbf{J}\|$ and $\|\mathbf{B}\|$. The size of each timestep is selected based on the characteristic speeds of the atomic species only (excluding electrons), and the simulation was run to a final time of 1.38E−7 seconds.

[3] Our ionization models rely on the presence of electrons within the gas for collisional ionization to occur. We have not at this point performed any detailed study of the effect of the initial ionized fraction on the progression of ionization in the simulation. If necessary, alternative strategies such as an electrode emission model for electrons could be explored in the future as a means of introducing sufficient seed electrons into the simulation to carry the initial current that is developed and to begin the collisional ionization process.

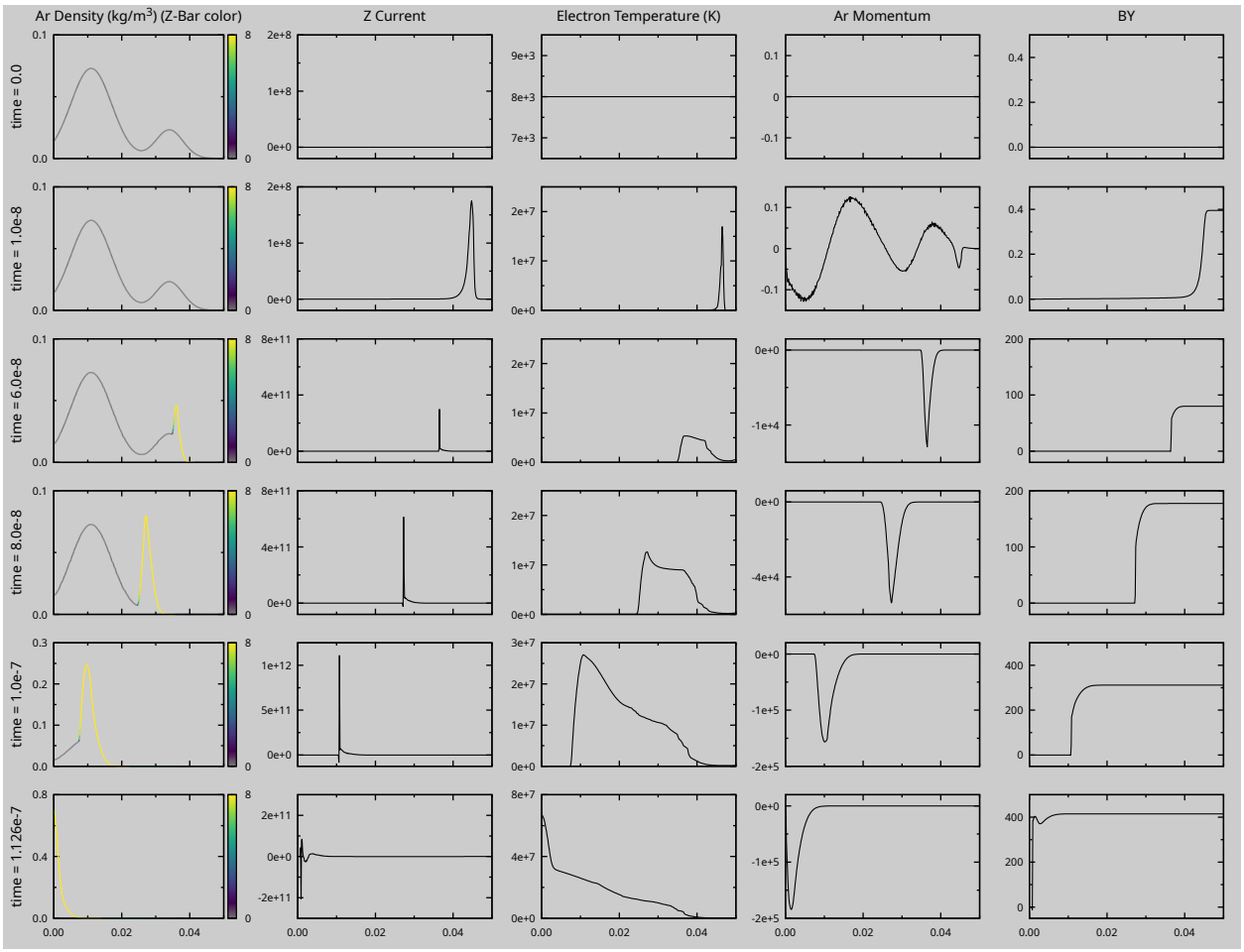

FIGURE 8.1. Solution quantities for a mock-up simulation of an argon gas puff experiment. Times are given in seconds, and the x-axis of each plot shows the radial position within the experiment in units of meters.

The evolution of various solution quantities is shown in fig. 8.1. While the simulation is not intended to be fully realistic at this point, the overall behavior seems qualitatively reasonable. Since the initial condition for the gas is not a hydrodynamic equilibrium, there is some initial momentum that develops early in time simply from the dynamics of the fluid expansion. As the electromagnetic fields reach the edge of the gas, the combination of Lorenz forces and elastic scattering yields resistive heating effects, and the gas progressively heats, ionizes, and compresses.

9. CONCLUSION

We have provided detailed descriptions of a general multifluid model framework for partially-ionized multispecies plasmas. The models are composed of a standard set of five-moment fluid equations for each species plus a description of electromagnetics. The most general model considered utilizes a full set of fluid equations for each charge state of each atomic species, plus a set of fluid equations for electrons. The fluid equations are coupled through source terms describing electromagnetic interactions, ionization, recombination, charge exchange, and elastic scattering collisions in the low-density coronal limit. The form of each of these source terms has been described in detail, and references for required rate coefficients have been identified for a diverse range of atomic species. Initial efforts have been made to extend these models to incorporate some higher-density collisional effects, including ionization potential depression and three-body recombination.

Some reductions of the general multifluid model have been considered. First, a reduced multifluid model was

derived which averages over all of the charge states (including neutrals) of each atomic species in the general multifluid model. The resulting model maintains full consistency with the general multifluid model from which it was derived by leveraging a quasi-steady-state collisional ionization equilibrium assumption to recover the ionization fractions required to make use of the general collision models. Further reductions were briefly considered to derive certain components of a single-fluid magnetohydrodynamics (MHD) model. In this case, a generalized Ohm's law was obtained, and the standard MHD resistivity was expressed in terms of the collisional models used in the general multifluid model. These consistently-derived material parameters may be used in future efforts to develop comparisons between various fluid models in this hierarchy.

A number of numerical considerations required to obtain robust implementations of these multifluid models were discussed. First, an AFC stabilization approach for a continuous Galerkin finite element discretization of the multifluid system was described in which the characteristic speeds used in the stabilization of the fluid systems are synchronized across all species in the model. It was demonstrated that this synchronization is crucial in order to obtain a robust discretization of the multifluid system.

Additionally, several different formulations were considered for describing the electromagnetics portion of the multifluid system using nodal continuous Galerkin finite element discretizations. While our original intent for this work did not include a detailed exploration of this issue, it quickly became apparent that careful treatment of the electromagnetics portion of the multifluid system (to ensure that the divergence involutions in Maxwell's equations are adequately satisfied) was required in order to obtain sufficient robustness in our numerical implementation. The formulations considered include a parabolic divergence cleaning method and an implicit projection method for the traditional curl formulation of Maxwell's equations, a purely-hyperbolic potential-based formulation of Maxwell's equations, and a mixed hyperbolic-elliptic potential-based formulation of Maxwell's equations. Some advantages and disadvantages of each formulation were explored to compare solution robustness and the ease of use of each formulation:

(i) Since it is based on the traditional curl form of Maxwell's equations, the parabolic divergence cleaning formulation was relatively easy to work with, in the sense that the imposition of various boundary conditions is well understood. Although this formulation worked reasonably well on the problems that we tested, the need to choose a penalty parameter that may vary from problem to problem raises some questions about the robustness of the formulation, unless progress can be made to establish a reliable approach for how this penalty parameter should be chosen.

(ii) The implicit projection formulation was shown to maintain robustness in all cases where it was used (in the sense that the divergence involutions in the electromagnetic fields were maintained to acceptable levels) without introducing any additional parameters to the model. However, the imposition of boundary conditions was found to be particularly difficult for this formulation. The most significant issues were encountered when attempting to use this formulation with periodic boundary conditions along an axis of the mesh in which the solution was not constant as a function of position. This often resulted in a failure to solve the resulting implicit system, and termination of the simulation. One hypothesis on how this issue could be resolved is that perhaps periodicity should only be applied to the physical variables, and not enforced on the correction potentials that are introduced by this formulation. We have not tried this approach due to limitations in our implementation, and we expect that such an approach would require special consideration in most codes, increasing the level of development effort required to make use of this formulation.

(iii) The hyperbolic structure of the purely-hyperbolic potential-based formulation of Maxwell's equations generally results in linear systems obtained from implicit discretization of the multifluid system that are somewhat easier to solve with standard preconditioning techniques compared to the other formulations. The imposition of appropriate boundary conditions can be moderately more involved for potential formulations, but was generally manageable with some additional effort. The most significant issue that was encountered when using this formulation was that solutions were observed to become unstable in a limited number of cases, implying that additional work would needed to reduce the gauge error produced by the discretization in order to ensure the robustness of this formulation.

(iv) The mixed hyperbolic-elliptic potential-based formulation of Maxwell's equations was one of the more robust and effective formulations that was considered. No instabilities were observed when this formulation was used in numerical simulations, and while the imposition of boundary conditions was moderately more

involved due to the use of potentials, this was generally manageable with some additional effort. The primary disadvantage of this formulation is the presence of an elliptic-form equation in the model, which can in practice make the resulting linear systems somewhat more difficult to solve using standard preconditioning techniques. While we did not specifically consider an in-depth investigation of solver efficiency in this work, we did not observe any significant issues with the solver requirements of this formulation for the problems considered.

A variety of numerical test problems were considered to evaluate the robustness and accuracy of our implementation. This included a range of spatially-homogeneous problems to examine the electromagnetic coupling of the fluids, the elastic collision source terms, and the ionization and recombination source terms. Analytic solutions were derived where applicable, and convergence studies were performed in these cases to demonstrate that the expected orders of convergence are obtained for a selection of implicit time discretizations. One-dimensional two-fluid electrostatic and electromagnetic shock-tube problems were used to demonstrate the robustness of the discretization methods in the two-fluid limit as well as the ideal shock-MHD limit. In particular, it was demonstrated that the implicit two-fluid simulations were able to reproduce single-fluid solutions near the ideal shock-MHD limit while resolving only the fluid stability criteria of the heavier ion species.

Two-dimensional test problems were then considered to further demonstrate the capabilities of the proposed methods. The first was a cylindrical diocotron instability using a tetrahedral mesh for a circular slab. The growth rates obtained for the initial perturbation were shown to closely match those available from theoretical analysis as the computational mesh was refined. The final test problem considered was the GEM challenge magnetic reconnection problem, using two thicknesses for the initial current sheet. The resulting rates of magnetic reconnection were shown to be in reasonable agreement with published values for kinetic, Hall MHD, and other two-fluid codes.

A one-dimensional simplified prototype of an argon gas puff configuration as deployed on Sandia's Z-machine was used as a demonstration to exercise the full range of capabilities associated with the general multifluid model. This simulation was not intended to be fully realistic, but did show qualitatively reasonable behavior for the system. Future work will focus on (i) additional verification of the general multifluid model in increasingly complex configurations incorporating the effects of elastic collisions, ionization, recombination, and charge-exchange; (ii) the implementation and verification of the fully-averaged multifluid model and the generalized Ohm's law MHD model; and (iii) detailed comparisons of the different models within this hierarchy on a selection of exemplar problems of interest.

REFERENCES

[1] S. A. ABDEL-NABY, D. NIKOLIĆ, T. W. GORCZYCA, K. T. KORISTA, AND N. R. BADNELL, *Dielectronic recombination data for dynamic finite-density plasmas: XIV. The aluminum isoelectronic sequence*, Astronomy & Astrophysics, 537 (2012), p. A40, doi:10.1051/0004-6361/201117544.

[2] M. ABRAMOWITZ AND I. A. STEGUN, eds., *Handbook of Mathematical Functions*, National Bureau of Standards, 1964.

[3] R. ALEXANDER, *Diagonally implicit Runge-Kutta methods for stiff O.D.E.'s*, SIAM Journal on Numerical Analysis, 14 (1977), pp. 1006–1021, doi:10.1137/0714068.

[4] E. E. ALLEN, *Analytical approximations*, Mathematical Tables and Other Aids to Computation, 8 (1954), p. 240.

[5] Z. ALTUN, A. YUMAK, N. R. BADNELL, J. COLGAN, AND M. S. PINDZOLA, *Dielectronic recombination data for dynamic finite-density plasmas: VI. The boron isoelectronic sequence*, Astronomy & Astrophysics, 420 (2004), pp. 775–781, doi:10.1051/0004-6361:20040964.

[6] Z. ALTUN, A. YUMAK, N. R. BADNELL, J. COLGAN, AND M. S. PINDZOLA, *Erratum to: Dielectronic recombination data for dynamic finite-density plasmas: VI. The boron isoelectronic sequence*, Astronomy & Astrophysics, 433 (2005), pp. 395–395, doi:10.1051/0004-6361:20040003e.

[7] Z. ALTUN, A. YUMAK, N. R. BADNELL, S. D. LOCH, AND M. S. PINDZOLA, *Dielectronic recombination data for dynamic finite-density plasmas: XI. The sodium isoelectronic sequence*, Astronomy & Astrophysics, 447 (2006), pp. 1165–1174, doi:10.1051/0004-6361:20053278.

[8] Z. ALTUN, A. YUMAK, I. YAVUZ, N. R. BADNELL, S. D. LOCH, AND M. S. PINDZOLA, *Dielectronic recombination data for dynamic finite-density plasmas: XIII. The magnesium isoelectronic sequence*, Astronomy & Astrophysics, 474 (2007), pp. 1051–1059, doi:10.1051/0004-6361:20078238.

[9] A. ALVAREZ LAGUNA, N. OZAK, A. LANI, H. DECONINCK, AND S. POEDTS, *Fully-implicit finite volume method for the ideal two-fluid plasma model*, Computer Physics Communications, 231 (2018), pp. 31–44, doi:10.1016/j.cpc.2018.05.006.

[10] T. AMANO, *Divergence-free approximate Riemann solver for the quasi-neutral two-fluid plasma model*, Journal of Computational Physics, 299 (2015), pp. 863–886, doi:10.1016/j.jcp.2015.07.035.

[11] T. AMANO, *A second-order divergence-constrained multidimensional numerical scheme for relativistic two-fluid electrodynamics*, The Astrophysical Journal, 831 (2016), p. 100, doi:10.3847/0004-637x/831/1/100.

[12] N. R. BADNELL, *Dielectronic recombination data for dynamic finite-density plasmas: X. The hydrogen isoelectronic sequence*, Astronomy & Astrophysics, 447 (2006), pp. 389–395, doi:10.1051/0004-6361:20053269.

[13] N. R. BADNELL, *Radiative recombination data for modeling dynamic finite-density plasmas*, The Astrophysical Journal Supplement Series, 167 (2006), pp. 334–342, doi:10.1086/508465.

[14] N. R. BADNELL, M. G. O'MULLANE, H. P. SUMMERS, Z. ALTUN, M. A. BAUTISTA, J. COLGAN, T. W. GORCZYCA, D. M. MITNIK, M. S. PINDZOLA, AND O. ZATSARINNY, *Dielectronic recombination data for dynamic finite-density plasmas: I. Goals and methodology*, Astronomy & Astrophysics, 406 (2003), pp. 1151–1165, doi:10.1051/0004-6361:20030816.

[15] D. S. BALSARA, T. AMANO, S. GARAIN, AND J. KIM, *A high-order relativistic two-fluid electrodynamic scheme with consistent reconstruction of electromagnetic fields and a multidimensional Riemann solver for electromagnetism*, Journal of Computational Physics, 318 (2016), pp. 169–200, doi:10.1016/j.jcp.2016.05.006.

[16] C. F. BARNETT, *Atomic data for fusion – Volume 1: Collisions of H, H2, He, and Li atoms and ions with atoms and molecules*, Tech. Report ORNL-6086/V1, Oak Ridge National Laboratory, Oak Ridge, TN, 1990.

[17] M. A. BAUTISTA AND N. R. BADNELL, *Dielectronic recombination data for dynamic finite-density plasmas: XII. The helium isoelectronic sequence*, Astronomy & Astrophysics, 466 (2007), pp. 755–762, doi:10.1051/0004-6361:20077056.

[18] J. BIRN, J. F. DRAKE, M. A. SHAY, B. N. ROGERS, R. E. DENTON, M. HESSE, M. KUZNETSOVA, Z. W. MA, A. BHATTACHARJEE, A. OTTO, AND P. L. PRITCHETT, *Geospace environmental modeling (GEM) magnetic reconnection challenge*, Journal of Geophysical Research: Space Physics, 106 (2001), pp. 3715–3719, doi:10.1029/1999JA900449.

[19] J. A. BITTENCOURT, *Fundamentals of Plasma Physics*, Springer-Verlag New York, 3rd ed., 2004.

[20] M. BRIO AND C. C. WU, *An upwind differencing scheme for the equations of ideal magnetohydrodynamics*, Journal of Computational Physics, 75 (1988), pp. 400–422, doi:10.1016/0021-9991(88)90120-9.

[21] P. BRYANS, N. R. BADNELL, T. W. GORCZYCA, J. M. LAMING, W. MITTHUMSIRI, AND D. W. SAVIN, *Collisional ionization equilibrium for optically thin plasmas. I. Updated recombination rate coefficients for bare through sodium-like ions*, The Astrophysical Journal Supplement Series, 167 (2006), pp. 343–356, doi:10.1086/507629.

[22] H.-K. CHUNG, M. CHEN, W. MORGAN, Y. RALCHENKO, AND R. LEE, *FLYCHK: Generalized population kinetics and spectral model for rapid spectroscopic analysis for all elements*, High Energy Density Physics, 1 (2005), pp. 3–12, doi:10.1016/j.hedp.2005.07.001.

[23] E. CLEMENTI, D. L. RAIMONDI, AND W. P. REINHARDT, *Atomic screening constants from SCF functions. II. Atoms with 37 to 86 electrons*, The Journal of Chemical Physics, 47 (1967), pp. 1300–1307, doi:10.1063/1.1712084.

[24] J. COLGAN, M. S. PINDZOLA, AND N. R. BADNELL, *Dielectronic recombination data for dynamic finite-density plasmas: V. The lithium isoelectronic sequence*, Astronomy & Astrophysics, 417 (2004), pp. 1183–1188, doi:10.1051/0004-6361:20034197.

[25] J. COLGAN, M. S. PINDZOLA, AND N. R. BADNELL, *Erratum to: Dielectronic recombination data for dynamic finite-density plasmas: V. The lithium isoelectronic sequence*, Astronomy & Astrophysics, 429 (2005), pp. 369–369, doi:10.1051/0004-6361:20042105.

[26] J. COLGAN, M. S. PINDZOLA, A. D. WHITEFORD, AND N. R. BADNELL, *Dielectronic recombination data for dynamic finite-density plasmas: III. The beryllium isoelectronic sequence*, Astronomy & Astrophysics, 412 (2003), pp. 597–601, doi:10.1051/0004-6361:20031362.

[27] M. M. CROCKATT, S. MABUZA, J. N. SHADID, S. CONDE, T. M. SMITH, AND R. P. PAWLOWSKI, *An implicit monolithic AFC stabilization method for the CG finite element discretization of the fully-ionized collisionless multifluid electromagnetic plasma system*, In Preparation, (2021).

[28] R. C. DAVIDSON, *Physics of Nonneutral Plasmas*, World Scientific Publishing, 2001.

[29] R. C. DAVIDSON AND G. M. FELICE, *Influence of profile shape on the diocotron instability in a non-neutral plasma column*, Physics of Plasmas, 5 (1998), pp. 3497–3511, doi:10.1063/1.873067.

[30] A. DEDNER, F. KEMM, D. KRÖNER, C.-D. MUNZ, T. SCHNITZER, AND M. WESENBERG, *Hyperbolic divergence cleaning for the MHD equations*, Journal of Computational Physics, 175 (2002), pp. 645–673, doi:10.1006/jcph.2001.6961.

[31] A. S. DICKINSON, M. S. LEE, AND L. A. VIEHLAND, *The mobility of He^+ ions in helium gas*, Journal of Physics B: Atomic, Molecular and Optical Physics, 32 (1999), pp. 4919–4930, doi:10.1088/0953-4075/32/20/309.

[32] W. L. FITE, A. C. H. SMITH, AND R. F. STEBBINGS, *Charge transfer in collisions involving symmetric and asymmetric resonance*, Proceedings of the Royal Society A: Mathematical, Physical and Engineering Sciences, 268 (1962), pp. 527–536, doi:10.1098/rspa.1962.0156.

[33] M. F. GU, *Radiative recombination rate coefficients for bare through F-like isosequences of Mg, Si, S, Ar, Ca, Fe, and Ni*, The Astrophysical Journal, 589 (2003), pp. 1085–1088, doi:10.1086/374796.

[34] Y. HAHN, *Improved rate formulas for dielectronic recombination*, Journal of Quantitative Spectroscopy and Radiative Transfer, 49 (1993), pp. 81–93, doi:10.1016/0022-4073(93)90020-I.

[35] Y. HAHN, *Corrigendum: Improved rate formulas for dielectronic recombination*, Journal of Quantitative Spectroscopy and Radiative Transfer, 51 (1994), p. 663, doi:10.1016/0022-4073(94)90121-X.

[36] A. HAKIM, J. LOVERICH, AND U. SHUMLAK, *A high resolution wave propagation scheme for ideal two-fluid plasma equations*, Jounal of Computational Physics, 219 (2006), pp. 4188–442, doi:10.1016/j.jcp.2006.03.036.

[37] A. H. HAKIM, *High Resolution Wave Propagation Schemes for Two-Fluid Plasma Simulations*, PhD thesis, University of Washington, 2006.

[38] C. HASTINGS JR., *Approximations for Digital Computers*, Princeton University Press, 1955.

[39] M. HESSE, J. BIRN, AND M. KUZNETSOVA, *Collisionless magnetic reconnection: Electron processes and transport modeling*, Journal of Geophysical Research: Space Physics, 106 (2001), pp. 3721–3735, doi:10.1029/1999JA001002.

[40] C. A. JENNINGS, D. J. AMPLEFORD, D. C. LAMPPA, S. B. HANSEN, B. JONES, A. J. HARVEY-THOMPSON, M. JOBE, T. STRIZIC, J. RENEKER, G. A. ROCHAU, AND M. E. CUNEO, *Computational modeling of Krypton gas puffs with tailored mass density profiles on Z*, Physics of Plasmas, 22 (2015), p. 056316, doi:10.1063/1.4921154.

[41] C. A. JENNINGS, M. E. CUNEO, E. M. WAISMAN, D. B. SINARS, D. J. AMPLEFORD, G. R. BENNETT, W. A. STYGAR, AND J. P. CHITTENDEN, *Simulations of the implosion and stangation of compact wire arrays*, Physics of Plasmas, 17 (2010), p. 092703, doi:10.1063/1.3474947.

[42] J. KAUR, T. W. GORCZYCA, AND N. R. BADNELL, *Dielectronic recombination data for dynamic finite-density plasmas: XV. The silicon isoelectronic sequence*, Astronomy & Astrophysics, 610 (2018), p. A41, doi:10.1051/0004-6361/201731243.

[43] C. A. KENNEDY AND M. H. CARPENTER, *Diagonally implicit Runge-Kutta methods for ordinary differential equations. A review*, Tech. Report NASA/TM-2016-219173, NASA Langley Research Center, Hampton, VA, 2016.

[44] W. KNAUER, *Diocotron instability in plasmas and gas discharges*, Journal of Applied Physics, 37 (1966), pp. 602–611, doi:10.1063/1.1708223.

[45] I. A. KOTELNIKOV AND A. I. MILSTEIN, *Electron radiative recombination with a hydrogen-like ion*, Physica Scripta, 94 (2019), p. 055403, doi:10.1088/1402-4896/ab060a.

[46] R. M. J. KRAMER, E. C. CYR, S. T. MILLER, E. G. PHILLIPS, G. A. RADTKE, A. C. ROBINSON, AND J. N. SHADID, *A plasma modeling hierarchy and verification approach*, Tech. Report SAND2020-3576, Sandia National Laboratories, Albuquerque, NM, USA, 2020, doi:10.2172/1608511.

[47] D. KUZMIN, M. MÖLLER, AND M. GURRIS, *Flux-Corrected Transport*, Springer Science, 2012, ch. Algebraic Flux Correction II, p. 193, doi:10.1007/978-94-007-4038-9.

[48] D. KUZMIN, M. MÖLLER, AND S. TUREK, *High-resolution FEM-FCT schemes for multidimensional conservation laws*, Computer Methods in Applied Mechanics and Engineering, 193 (2004), pp. 4915–4946, doi:10.1016/j.cma.2004.05.009.

[49] M. LANDINI AND B. C. MONSIGNORI FOSSI, *The X-UV spectrum of thin plasmas*, Astronomy & Astrophysics Supplement Series, 82 (1990), pp. 229–260.

[50] M. LANDINI AND B. C. MONSIGNORI FOSSI, *Ion equilibrium for minor components in a thin plasma*, Astronomy & Astrophysics Supplement Series, 91 (1991), pp. 183–196.

[51] R. H. LEVY AND R. W. HOCKNEY, *Computer experiments on low-density crossed-field electron beams*, The Physics of Fluids, 11 (1968), pp. 766–771, doi:10.1063/1.1691997.

[52] N. R. LEWKOW, V. KHARCHENKO, AND P. ZHANG, *Energy relaxation of helium atoms in astrophysical gases*, The Astrophysical Journal, 756 (2012), p. 57, doi:10.1088/0004-637X/756/1/57.

[53] S. D. LOCH, M. S. PINDZOLA, C. P. BALLANCE, D. C. GRIFFIN, D. M. MITNIK, N. R. BADNELL, M. G. O'MULLANE, H. P. SUMMERS, AND A. D. WHITEFORD, *Electron-impact ionization of all ionization stages of krypton*, Physical Review A, 66 (2002), p. 052708, doi:10.1103/PhysRevA.66.052708.

[54] W. LOTZ, *Electron-impact ionization cross-sections and ionization rate coefficients for atoms and ions from hydrogen to calcium*, Zeitschrift für Physik, 216 (1968), pp. 241–247, doi:10.1007/BF01392963.

[55] W. LOTZ, *Electron-impact ionization cross-sections and ionization rate coefficients for atoms and ions from scandium to zinc*, Zeitschrift für Physik, 220 (1969), pp. 466–472, doi:10.1007/BF01394789.

[56] J. LOVERICH, A. HAKIM, AND U. SHUMLAK, *A discontinuous galerkin method for ideal two-fluid plasma equations*, Communications in Computational Physics, 9 (2011), pp. 240–268, doi:10.4208/cicp.250509.210610a.

[57] J. LOVERICH, S. C. D. ZHOU, K. BECKWITH, M. KUNDRAPU, M. LOH, S. MAHALINGAM, P. STOLTZ, AND A. HAKIM, *Nautilus: A tool for modeling fluid plasmas*, in 51st AIAA Aerospace Sciences Meeting including the New Horizons Forum and Aerospace Exposition, Grapevine, Texas, USA, January 7-10, 2013, doi:10.2514/6.2013-1185.

[58] S. MABUZA, J. N. SHADID, E. C. CYR, R. P. PAWLOWSKI, AND D. KUZMIN, *A linearity preserving nodal variation limiting algorithm for continuous Galerkin discretization of ideal MHD equations*, Journal of Computational Physics, 410 (2020), p. 109390, doi:10.1016/j.jcp.2020.109390.

[59] S. MABUZA, J. N. SHADID, AND D. KUZMIN, *Local bounds preserving stabilization for continuous Galerkin discretization of hyperbolic systems*, Journal of Computational Physics, 361 (2018), pp. 82–110, doi:10.1016/j.jcp.2018.01.048.

[60] J. MAO, J. KAASTRA, AND N. R. BADNELL, *The electron energy loss rate due to radiative recombination*, Astronomy & Astrophysics, 599 (2017), p. A10, doi:10.1051/0004-6361/201629708.

[61] D. MARTÍNEZ-GÓMEZ, R. SOLER, AND J. TERRADAS, *Multi-fluid approach to high-frequency waves in plasmas. I. Small-amplitude regime in fully ionized media*, The Astrophysical Journal, 832 (2016), p. 101, doi:10.3847/0004-637X/832/2/101.

[62] D. MARTÍNEZ-GÓMEZ, R. SOLER, AND J. TERRADAS, *Multi-fluid approach to high-frequency waves in plasmas. II. Small-amplitude regime in partially ionized media*, The Astrophysical Journal, 837 (2017), p. 80, doi:10.3847/1538-4357/aa5eab.

[63] M. MATTIOLI, G. MAZZITELLI, K. B. FOURNIER, M. FINKENTHAL, AND L. CARRARO, *Updating of atomic data needed for ionization balance evaluations of krypton and molybdenum*, Journal of Physics B: Atomic, Molecular and Optical Physics, 39 (2006), pp. 4457–4489, doi:10.1088/0953-4075/39/21/010.

[64] E. MEIER AND U. SHUMLAK, *A general nonlinear fluid model for reacting plasma-neutral mixtures*, Physics of Plasmas, 19 (2012), p. 072508, doi:10.1063/1.4736975.

[65] E. T. MEIER, *Modeling Plasmas with Strong Anisotropy, Neutral Fluid Effects, and Open Boundaries*, PhD thesis, University of Washington, 2011.

[66] A. MIGNONE AND P. TZEFERACOS, *A second-order unsplit Godunov scheme for cell-centered MHD: The CTU-GLM scheme*, Journal of Computational Physics, 229 (2010), pp. 2117 – 2138, doi:10.1016/j.jcp.2009.11.026.

[67] S. T. MILLER, E. C. CYR, J. N. SHADID, R. M. J. KRAMER, E. G. PHILLIPS, AND S. CONDE, *IMEX and exact sequence discretization of the multi-fluid plasma model*, Journal of Computational Physics, 397 (2019), p. 108806, doi:10.1016/j.jcp.2019.05.052.

[68] D. M. MITNIK AND N. R. BADNELL, *Dielectronic recombination data for dynamic finite-density plasmas: VIII. The nitrogen isoelectronic sequence*, Astronomy & Astrophysics, 425 (2004), pp. 1153–1159, doi:10.1051/0004-6361:20041297.

[69] K. MIURA, *Development of a Multifluid Magnetohydrodynamic Model for Anisotropic, Partially Ionized Plasmas*, PhD thesis, University of Toronto, 2019.

[70] D. NIKOLIĆ, T. W. GORCZYCA, K. T. KORISTA, M. CHATZIKOS, G. J. FERLAND, F. GUZMÁN, P. A. M. VAN HOOF, R. J. R. WILLIAMS, AND N. R. BADNELL, *Suppression of dielectronic recombination due to finite density effects. II. Analytical refinement and application to density-dependent ionization balances and AGN broad-line emission*, The Astrophysical Journal Supplement Series, 237 (2018), p. 41, doi:10.3847/1538-4365/aad3c5.

[71] D. NIKOLIĆ, T. W. GORCZYCA, K. T. KORISTA, G. J. FERLAND, AND N. R. BADNELL, *Suppression of dielectronic recombination due to finite density effects*, The Astrophysical Journal, 768 (2013), p. 82, doi:10.1088/0004-637X/768/1/82.

[72] H. PAULS, G. ZANK, AND L. WILLIAMS, *Interaction of the solar wind with the local interstellar medium*, Journal of Geophysical Research, 100 (1995), pp. 21595–21604, doi:10.1029/95JA02023.

[73] J. PÉTRI, *Relativistic stabilisation of the diocotron instability in a pulsar "cylindrical" electrosphere*, Astronomy & Astrophysics, 469 (2007), pp. 843–855, doi:10.1051/0004-6361:20066985.

[74] J. PÉTRI, *Non-linear evolution of the diocotron instability in a pulsar electrosphere: two-dimensional particle-in-cell simulations*, Astronomy & Astrophysics, 503 (2009), pp. 1–12, doi:10.1051/0004-6361/200911778.

[75] E. PHIPPS AND R. PAWLOWSKI, *Efficient expression templates for operator overloading-basedautomatic differentiation*, in Recent Advances in Algorithmic Differentiation, S. Forth, P. Hovland, E. Phipps, J. Utke, and A. Walther, eds., Berlin, Heidelberg, 2012, Springer Berlin Heidelberg, pp. 309–319, doi:10.1007/978-3-642-30023-3_28.

[76] P. L. PRITCHETT, *Geospace environment modeling magnetic reconnection challenge: Simulations with a full particle electromagnetic code*, Journal of Geophysical Research: Space Physics, 106 (2001), pp. 3783–3798, doi:10.1029/1999JA001006.

[77] N. REDDELL, *A Kinetic Vlasov Model for Plasma Simulation Using Discontinuous Galerkin Method on Many-Core Architectures*, PhD thesis, University of Washington, 2016.

[78] A. ROHDE, *Eigenvalues and eigenvectors of the Euler equations in general geometries.* 15th AIAA Computational Fluid Dynamics Conference, Anaheim, California, USA, June 11-14, 2001, doi:10.2514/6.2001-2609.

[79] H. SCHMITZ AND R. GRAUER, *Kinetic Vlasov simulations of collisionless magnetic reconnection*, Physics of Plasmas, 13 (2006), p. 092309, doi:10.1063/1.2347101.

[80] S. H. SCHOT, *Eighty years of Sommerfeld's radiation condition*, Historia Mathematica, 19 (1992), pp. 385–401, doi:10.1016/0315-0860(92)90004-U.

[81] R. SCHUNK, *Mathematical structure of transport equations for multispecies flows*, Reviews of Geophysics, 15 (1977), pp. 429–445, doi:10.1029/RG015i004p00429.

[82] M. A. SHAY, J. F. DRAKE, B. N. ROGERS, AND R. E. DENTON, *Alfvénic collisionless magnetic reconnection and the Hall term*, Journal of Geophysical Research: Space Physics, 106 (2001), pp. 3759–3772, doi:10.1029/1999JA001007.

[83] G. A. SOD, *A survey of several finite difference methods for systems of nonlinear hyperbolic conservation laws*, Journal of Computational Physics, 27 (1978), pp. 1–31, doi:10.1016/0021-9991(78)90023-2.

[84] A. SOMMERFELD, *Partial Differential Equations in Physics*, Academic Press, 1949.

[85] B. SRINIVASAN AND U. SHUMLAK, *Analytical and computational study of the ideal full two-fluid plasma model and asymptotic approximations for Hall-magnetohydrodynamics*, Physics of Plasmas, 18 (2011), p. 092113, doi:10.1063/1.3640811.

[86] N. C. STERLING, *Atomic data for neutron-capture elements II. photoionization and recombination properties of low-charge krypton ions*, Astronomy & Astrophysics, 533 (2011), p. A62, doi:10.1051/0004-6361/201117471.

[87] N. C. STERLING, H. L. DINERSTEIN, AND T. R. KALLMAN, *The abundances of light neutron-capture elements in planetary nebulae I. photoionization modeling and ionization corrections*, The Astrophysical Journal Supplement Series, 169 (2007), pp. 37–61, doi:10.1086/511031.

[88] J. C. STEWART AND K. D. PYATT, JR., *Lowering of ionization potentials in plasmas*, The Astrophysical Journal, 144 (1966), p. 1203, doi:10.1086/148714.

[89] V. TANGRI, J. L. GIULIANI, A. L. VELIKOVICH, N. OUART, A. DASGUPTA, J. P. APRUZESE, A. J. HARVEY-THOMPSON, C. A. JENNINGS, AND B. JONES, *Simulations of recent argon gas-puff implosions on Z with Xe and Kr dopants*, IEEE Transactions on Plasma Science, 46 (2018), pp. 3871–3880, doi:10.1109/TPS.2018.2869724.

[90] V. TANGRI, A. J. HARVEY-THOMPSON, J. L. GIULIANI, J. W. THORNHILL, A. L. VELIKOVICH, J. P. APRUZESE, N. D. OUART, A. DASGUPTA, B. JONES, AND C. A. JENNINGS, *Simulations of Ar gas-puff Z-pinch radiation*

sources with double shells and central jets on the Z generator, Physics of Plasmas, 23 (2016), p. 101201, doi:10.1063/1.4965235.

[91] J. W. THORNHILL, J. L. GIULIANI, Y. K. CHONG, A. L. VELIKOVICH, A. DASGUPTA, J. P. APRUZESE, B. JONES, D. J. AMPLEFORD, C. A. COVERDALE, C. A. JENNINGS, E. M. WAISMAN, D. C. LAMPPA, J. L. MCKENNEY, M. E. CUNEO, M. KRISHNAN, P. L. COLEMAN, R. E. MADDEN, AND K. W. ELLIOT, *Two-dimensional radiation MHD modeling assessment of designs for argon gas puff distributions for future experiments on the refurbished Z machine*, High Energy Density Physics, 8 (2012), pp. 197–208, doi:10.1016/j.hedp.2012.03.010.

[92] J. W. THORNHILL, J. L. GIULIANI, B. JONES, J. P. APRUZESE, A. DASGUPTA, Y. K. CHONG, A. J. HARVEY-THOMPSON, D. J. AMPLEFORD, S. B. HANSEN, C. A. COVERDALE, C. A. JENNINGS, G. A. ROCHAU, M. E. CUNEO, D. C. LAMPPA, D. JOHNSON, M. C. JONES, N. W. MOORE, E. M. WAISMAN, M. KRISHNAN, AND P. L. COLEMAN, *2-D RMHD modeling assessment of current flow, plasma conditions and doppler effects in recent Z argon experiments*, IEEE Transactions on Plasma Science, 43 (2015), pp. 2480–2491, doi:10.1109/TPS.2015.2422373.

[93] G. TÓTH, Y. MA, AND T. I. GOMBOSI, *Hall magnetohydrodynamics on block-adaptive grids*, Journal of Computational Physics, 227 (2008), pp. 6967 – 6984, doi:10.1016/j.jcp.2008.04.010.

[94] T. UMEDA, K. TOGANO, AND T. OGINO, *Two-dimensional full-electromagnetic Vlasov code with conservative scheme and its application to magnetic reconnection*, Computer Physics Communications, 180 (2009), pp. 365–374, doi:10.1016/j.cpc.2008.11.001.

[95] D. A. VERNER AND G. J. FERLAND, *Atomic data for astrophysics. I. Radiative recombination rates for H-like, He-like, Li-like, and Na-like ions over a broad range of temperature*, The Astrophysical Journal Supplement Series, 103 (1996), p. 467, doi:10.1086/192284.

[96] G. VORONOV, *A practical fit formula for ionization rate coefficients of atoms and ions by electron impact: z =1-28*, Atomic Data and Nuclear Data Tables, 65 (1997), pp. 1–35, doi:10.1006/adnd.1997.0732.

[97] J. VRANJES AND P. S. KRSTIC, *Collisions, magnetization, and transport coefficients in the lower solar atmosphere*, Astronomy & Astrophysics, 554 (2013), p. A22, doi:10.1051/0004-6361/201220738.

[98] E. M. WAISMAN, R. D. MCBRIDE, M. E. CUNEO, D. F. WENGER, W. E. FOWLER, W. A. JOHNSON, L. I. BASILO, R. S. COATS, C. A. JENNINGS, D. B. SINARS, R. A. VESEY, B. JONES, D. J. AMPLEFORD, R. W. LEMKE, M. R. MARTIN, P. C. SCHRAFEL, S. A. LEWIS, J. K. MOORE, M. E. SAVAGE, AND W. A. STYGAR, *Voltage measurements at the vacuum post-hole convolute of the Z pulsed-power accelerator*, Physical Reveiw Special Topics Accelerators and Beams, 17 (2014), p. 120401, doi:10.1103/PhysRevSTAB.17.120401.

[99] E. M. WOLF, *A particle-in-cell method for the simulation of plasmas based on an unconditionally stable wave equation solver*, PhD thesis, Michigan State University, East Lansing, MI, USA, 2015.

[100] O. ZATSARINNY, T. W. GORCZYCA, J. FU, K. T. KORISTA, N. R. BADNELL, AND D. W. SAVIN, *Dielectronic recombination data for dynamic finite-density plasmas: IX. The fluorine isoelectronic sequence*, Astronomy & Astrophysics, 447 (2006), pp. 379–387, doi:10.1051/0004-6361:20053737.

[101] O. ZATSARINNY, T. W. GORCZYCA, K. KORISTA, N. R. BADNELL, AND D. W. SAVIN, *Dielectronic recombination data for dynamic finite-density plasmas: VII. The neon isoelectronic sequence*, Astronomy & Astrophysics, 426 (2004), pp. 699–705, doi:10.1051/0004-6361:20040463.

[102] O. ZATSARINNY, T. W. GORCZYCA, K. T. KORISTA, N. R. BADNELL, AND D. W. SAVIN, *Dielectronic recombination data for dynamic finite-density plasmas: II. The oxygen isoelectronic sequence*, Astronomy & Astrophysics, 412 (2003), pp. 587–595, doi:10.1051/0004-6361:20031462.

[103] O. ZATSARINNY, T. W. GORCZYCA, K. T. KORISTA, N. R. BADNELL, AND D. W. SAVIN, *Dielectronic recombination data for dynamic finite-density plasmas: IV. The carbon isoelectronic sequence*, Astronomy & Astrophysics, 417 (2004), pp. 1173–1181, doi:10.1051/0004-6361:20034174.

APPENDIX A. TIME SCALES

The calculation of timescales associated with various physical processes included in a given multifluid model is of general interest. In the context of numerical simulations, it is often useful to be able to compute these timescales at each point in time during a simulation to either (i) determine if the time integration scheme is able to resolve the dynamics associated that process, if the timestep size is selected based on other criteria not dependent on the timescales of that process; or (ii) ensure that the time integration scheme is able to resolve the dynamics associated with that process through appropriate choice of timestep size. The purpose of this section is to describe a selection of timescales associated with the multifluid models that have implementations available within Drekar. It should be noted that this list is not meant to be an exhaustive description of timescales relevant to the multifluid models: It is simply intended to serve as documentation of the timescale implementation in Drekar.

A.1. Plasma frequency

The standard definition of (electron) plasma frequency gives us a measure of the timescale of the high-frequency oscillations present in the plasma due to separation between electron and ion dynamics:

$$\tau_f = \frac{2\pi m_e}{q_e}\sqrt{\frac{\epsilon_0}{\rho_e}}. \tag{186}$$

A.2. Collision timescale

The analysis in section 7.1.1 gives us some crucial insight into the dynamics of collisional relaxation processes in the general multifluid model. Using the exact solutions generated in section 7.1.1, we define the timecales for collisional relaxation of velocity and temperature by

$$\tau^{-1}_{s;t(\mathbf{u})} = \alpha_{s;t}\left(\rho_s + \rho_t\right), \tag{187a}$$

$$\tau^{-1}_{s;t(T)} = 3\left(\gamma - 1\right)\alpha_{s;t}\frac{m_s m_t}{m_s + m_t}\left(n_s + n_t\right), \tag{187b}$$

respectively. It should be noted that in the case of two species with comparable number densities but drastically different masses, the magnitude of $(\rho_s + \rho_t)$ is roughly that of the mass density of the heavier species, but the magnitude of

$$\frac{m_s m_t}{m_s + m_t}\left(n_s + n_t\right) \tag{188}$$

is closer to the mass density of the lighter species. Thus the relaxation timescales for velocity and temperature often differ by a factor of approximately the mass ratio between the species, with the timescale for temperature relaxation being much longer than that of the velocity relaxation.

DISTRIBUTION

Email—Internal [redacted]

Name	Org.	Sandia Email Address
Technical Library	1911	sanddocs@sandia.gov

Sandia National Laboratories

Sandia National Laboratories is a multimission laboratory managed and operated by National Technology & Engineering Solutions of Sandia LLC, a wholly owned subsidiary of Honeywell International Inc., for the U.S. Department of Energy's National Nuclear Security Administration under contract DE-NA0003525.